Nonlinear Dynamic Analysis of Electrostatically Actuated MEMS Structures

RAKESH KALYANARAMAN

A Thesis

in

The Department

of

Mechanical and Industrial Engineering

Presented in partial fulfillment of the requirements for the
Degree of Master of Applied Science (Mechanical Engineering) at
Concordia University
Montreal, Quebec, Canada

June 2006

Canada

ABSTRACT

Nonlinear Dynamic Analysis of Electrostatically Actuated MEMS Structures

Rakesh Kalyanaraman

Micro Electro Mechanical Systems (MEMS) such as microsensors and microactuators that use the electrostatic force between electrodes for sensing and actuation, have numerous advantages over other actuation mechanisms due to their ease of operation, simplicity and favourable scaling laws in the micro domain. One of the main considerations while using electrostatic actuations is that the devices must be operated in the safe working range as there exists the phenomenon of pull-in instability which leads to the failure of the system. In the present work, the non linear analysis of electrostatically actuated MEMS structures is carried out to predict the pull-in voltages and frequencies in order to determine the range of operation for the system throughout the life-cycle without damage.

An analogy between the electrostatic phenomenon in MEMS structures and the aeroelastic phenomenon in aircraft wing structures has been inferred in this work. Initially, a linear analysis is adopted to understand the phenomenon in both these fields and their instabilities such as pull-in, divergence and flutter have been explained. Different active and passive control methods adopted so far by various researchers to avoid the instabilities in both the cases are presented. New terminologies have been proposed for MEMS based on their similarity with the aeroelastic phenomenon.

The feasibility of microfabrication of the electrostatic MEMS structures based on MicraGeM process is presented in this work. The conversion of a continuous cantilever system into an equivalent lumped mass-spring model based on their energy has been formulated and the equivalent stiffness, mass and electrostatic areas are found to perform the nonlinear analysis of the system. The phase portrait techniques are adopted to find the pull-in voltage and the natural frequency of the mass-spring system, and the significance of the conservative energy value on the system behaviour are discussed. Hence a comparision of this nonlinear approach with the linear case has been done and their respective results are discussed.

A non-contact optical Laser Doppler Velocimetry (LDV) set-up is used for the dynamic testing of micro cantilevers. Testing procedures along with the safe operating measures have been presented in order to avoid the pull-in condition. The frequency plots have been drawn for different DC and AC voltages based on the spectral analyzer frequency responses. Finally, the comparision of these frequency plots against the voltages from both the experimental testing and the nonlinear theoretical prediction is carried out and the percentage of accuracy of the prediction value has been found.

This thesis is
dedicated to my parents

Acknowledgements

The author is deeply privileged to work under thesis supervisors Dr. Rama B. Bhat and Dr. Muthukumaran Packirisamy. It was Dr. Rama B Bhat's invaluable advice to look at the physical phenomenon as a whole, independent of whether it is micro or macro that made the author channeling his thoughts on a technical level. The author is deeply grateful to him for providing an opportunity to be a miniscule of his infinite modes of vibration.

The author would also like to express his sincere gratitude to the co-supervisor Dr. Muthukumaran Packirisamy. His innovative and passionate ideas on MEMS helped the author build the thesis throughout the course of this work. The author would like to express his sincere gratitude to Dr. Packirisamy for being a constant source of inspiration.

The author is obliged to his cousins Dr. Srinivasan Krishnamurthy, Indurekha Krishnamurthy and their family for their invaluable support throughout the course of this work. It is the author's pleasure to work with his colleagues, Dr. Gino, Mr. Arvind, Mr. Kiran, Mr. Raghavendra, Mr. Avinash, Mr. Ashwin, Mr. Jian Liang You, Mr. Li, Mr. Anand (and the list goes on) for providing valuable help during different stages of this work. Last, but not the least, the author would like to express his gratitude to his parents, his sister and his friends for being there always.

TABLE OF CONTENTS

LIST OF FIGURES

LIST OF TABLES

ABBREVIATIONS

A.C.	Aerodynamic Centre
AC	Alternating Current
ACO	Anharmonic Casimir Oscillator
AFM	Atomic Force Microscope
BEM	Boundary Element Method
CMC	Canadian Microelectronics Corporation
CMOS	Complementary Metal Oxide Semiconductor
DC	Direct Current
DQM	Differential Quadrature Method
DRIE	Deep Reactive Ion Etching
FEA	Finite Element Analysis
FEM	Finite Element Method
MEMS	Micro -Electro-Mechanical Systems
MicraGeM	Micralyne Generalized MEMS
MOEMS	Micro-Opto-Electro-Mechanical Systems
MST	Micro Systems Technology
MUMPs	Multi-User MEMS Process System
PZT	Piezoelectric
RF	Radio Frequency
RIE	Reactive Ion Etching

SCREAM	Single Crystal Reactive Etching And Metallization
SEM	Scanning Electron Microscopy
SFC	Sequential Field Coupling
Si	Silicon
SiO_2	Silicon dioxide
SMA	Shape Memory Alloy
SOI	Silicon-on-Insulator
TMAH	Tetra Methyl Ammonium Hydroxide
XeF_2	Xenon Diflouride

LIST OF SYMBOLS

α	Angle of attack
α_0	Initial angle of attack
α_i	Initial angle of oscillation
α_e	Elastic twist
ε_o	Permittivity of free space
ε_r	Permittivity of air
ρ	Density
θ	Angle of deflection
θ_{max}	Maximum amplitude of oscillation
ω	Frequency of vibration
ω_n	Natural Frequency
$\phi(x)$	Orthogonal polynomial
μm	micrometers
ΔE	Change in energy
$\dfrac{\partial C_L}{\partial \alpha}$	Lift curve slope
a	Arbitrary constant
A	Area of the plate
A_{eq_i}	Equivalent electrostatic area
b	Width of the lumped mass-spring model

B	Width of the plate
c	Mean chord length
cm	Centimeters
C_L	Lift coefficient
C_{MAC}	Moment coefficient about the aerodynamic center
d	Gap between the top and bottom plate
e	eccentricity
E	Young's modulus
E_0	Conservative energy value
E_1^*	Minimum conservative energy value
E_2^*	Maximum conservative energy value
F	Farad
F_{el}	Electrostatic force
g	Acceleration due to gravity
H_{ext}	External magnetic field
Hz	Hertz
I	Moment of inertia
k	Stiffness of the spring
k_{elec}	Electrostatic stiffness
$k^d{}_{elec}$	Equivalent electrostatic stiffness for dynamic motion
$k^s{}_{elec}$	Equivalent electrostatic stiffness for static deflection
k_{aero}	Stiffness due to aerodynamic lift

kg	kilogram
kHz	kilo Hertz
K_α	Rotational stiffness of the wing
K_{eq}	Equivalent stiffness of the lumped mass-spring model
l	Length of the lumped mass-spring model
L	Aerodynamic lift force
L_l	Length of the plate
L_s	Length of the string
m	meter
mm	millimeter
M	Mass of the plate
M_{AC}	Moment about the aerodynamic center
M_{eq}	Equivalent mass of the lumped mass-spring model
M_y	Moment about the elastic axis
N	Newton
q	Dynamic pressure
q_{DIV}	Divergence pressure
s	second
S	Area of the wing
t	Thickness of the lumped mass-spring model
t_p	Time of oscillation
T	Time period

T_b	Kinetic energy of the beam
T_{rig}	Kinetic energy of the rigid plate
U	Dynamic speed
U_b	Potential energy of the beam
U_{DIV}	Divergence speed
$U_{el.be_i}$	Electrostatic potential energy
$U_{el.rig_i}$	Equivalent electrostatic potential energy of the lumped mass-spring model
U_{rig}	Potential energy of the rigid plate
V	Voltage applied
V_p	Pull-in voltage
$w(x)$	Deflection of the cantilever beam
$w_{av.st_i}$	Average static deflection
x	Displacement of the moving plate
$\dot{x}$	Velocity of the mass-spring model
x_1, x_2, x_3	Zero velocity points
x_p	Pull-in position
x_{st}	Static equilibrium position

Chapter 1

Introduction

1.1 Introduction to Micro Electro Mechanical Systems

Miniaturized devices or micro devices which consist of both electrical and mechanical components are termed as Micro Electro Mechanical Systems (MEMS). The origin of MEMS can be attributed to Richard Feynman, who mentioned about the possibility of miniaturization [1]. Since then, there has been significant progress in understanding the Micro Systems Technology (MST) more in detail [2-6].
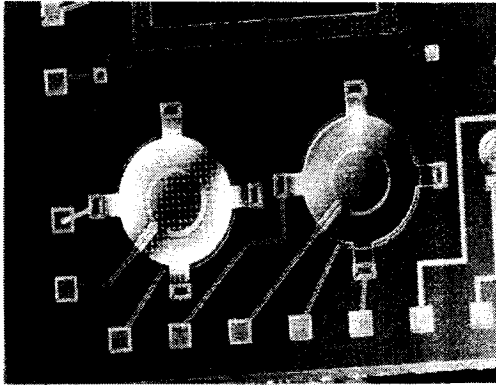
(a) Circular type, diameter = 600μm   (b) Triangular type
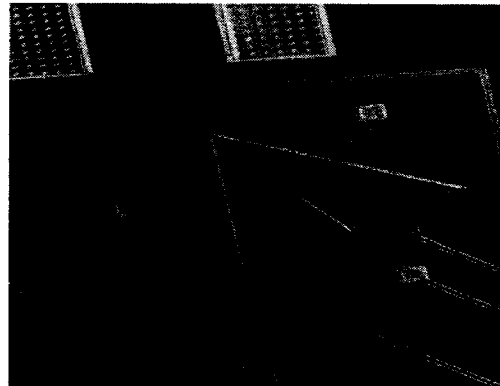
Fig. 1.1 Examples of MEMS devices - Electrostatic actuators

Most of the MEMS structures are based on silicon and its derivatives. The properties of silicon and its crystallographic orientation have helped tremendously in the synthesis of

MEMS devices. For example, high performance in silicon based sensors and actuators, is due to the lack of mechanical hysteresis [7] in silicon. The usefulness of silicon in the synthesis of microdevices is further highlighted by the feasibility of different micromachining techniques employed for the microfabrication of MEMS structures using silicon as the base substrate.

Through the different techniques available for fabrication, it is possible to realize unlimited design geometries for the MEMS devices. Bulk micromachining and surface micromachining are the two types of fabrication methods used in the MEMS industry. Etching, a part of bulk micromachining process which involves 'bulk' removal of the substrate, has resulted in the development of many MEMS devices [8]. The choice of bulk microfabrication also depends upon exploiting the etching behaviour of silicon with respect to its crystallographic planes. Whereas the uniform etching in all directions is produced with isotropic etching, the anisotropic etching is specific to the crystallographic planes of the substrate. Isotropic etching has been demonstrated with XeF_2 [9] and Petersen et al. [10] showed that properties of silicon and its etching behaviour on different lattices facilitate it as a convenient material for MEMS structure.

Surface micromachining [11] is another microfabrication technique which is useful in certain microfabrications. This technique involves building different material layers on top of a bottom substrate. An example of surface micromachining process is MUMPs [12] technology which has been used for the fabrication of many MEMS devices such as micromirrors, microactuators etc. Apart from these techniques, there are some of the

other industry defined MEMS fabrication processes like MicraGeM [13], Protolyne [14], SCREAM [15] etc. which are available. MEMS devices are delicate structures sensitive to damage from handling or environmental effects. Their functionality depends on either sealing the environment or being in direct contact with it. Stress, thermal load and contaminants may change their characteristics. Hence, packaging technology is extended from microelectronics towards MEMS and MOEMS (Micro-Opto-Electro-Mechanical Systems) fields. Single chip packaging [16] and multi chip packaging [17] are the main packaging techniques that are currently used in the MEMS industry for enabling safe and easy device handling. Proper packaging is essential not only to connect a loose MEMS device to external circuit but also enhance the longevity of the device.

1.2 Types of MEMS Actuation

Actuation can be defined as altering the mechanical state of a system by effectively exchanging the energy level of that system with its surroundings [18]. Different types of actuation principles are used in the MEMS structures so far and each of them has its own advantages and its limitations. Some of the actuation types which are being used for the MEMS devices are electrostatic, piezoelectric, magnetic, thermal, pneumatic/hydraulic, chemical and biological methods. Even though all the above mentioned actuation principles have been employed so far, the most widely used are the electrostatic, piezoelectric, magnetic and the thermal actuation methods [19].

3

1.2.1 Piezoelectric actuation

When materials such as quartz, tourmaline and synthesized ceramics are subjected to a mechanical force, an electric field is produced due to the polarization of these materials. The reverse also holds true, that when an electric field is applied on these materials, (i.e) a mechanical stress is developed. This phenomenon is called as the piezoelectric effect and the materials which exhibit these properties are called piezoelectric materials. For example, a micropump used for biomedical applications is shown in Figure 1.2 below. An alternating voltage applied to the piezoelectric (PZT) component causes the expansion and contraction along the horizontal direction which in turn induces a bending stress in the diaphragm. This results in the pumping of the fluid from the inlet flap to the outlet flap through the pump chamber [20]. The different applications of the piezoelectric actuation include RF MEMS tunable capacitor [21] and microvalve [22] as well.
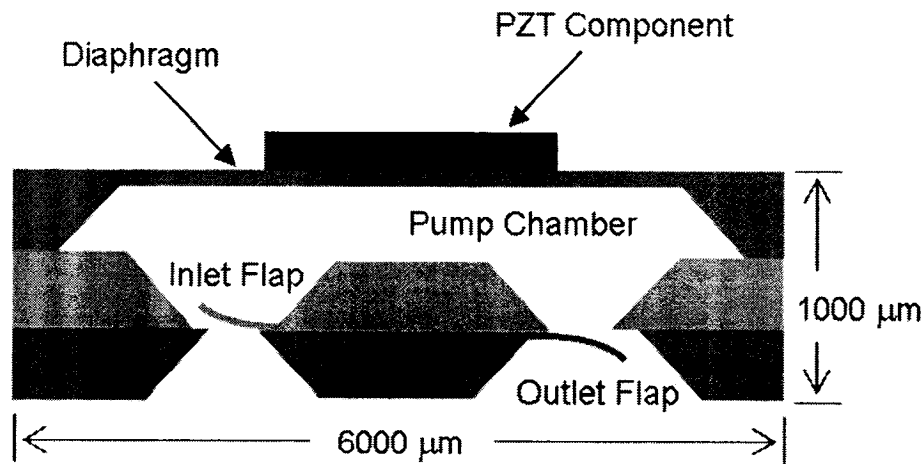
Fig. 1.2 Cross-section view of the micropump [20]

4

1.2.2 Magnetic actuation

Magnetic actuation is caused when an electroplated magnetic material, for example a Permalloy, is subjected to an external magnetic field, thereby causing mechanical actuation. As shown in Figure 1.3, a 3-dimensional hinged microstructure [23] is subjected to a magnetic actuation and the flap can be rotated till 90° with respect to the substrate based on the permalloy volume and also on the applied external magnetic field H_{ext}.
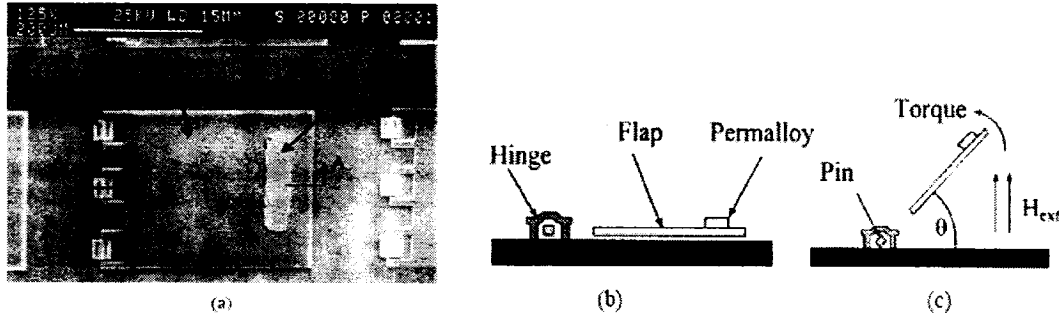
Fig. 1.3 (a) An SEM micrograph of a hinged flap magnetic actuator. (b) Schematic cross-sectional view (A-A) when there is no H_{ext} applied. (c) When H_{ext} exceeds a threshold value [23]

1.2.3 Thermal actuation

Thermal actuation is based on the principle that when an electric current is applied across the actuator terminals, the heating up of the actuator and the resulting differential thermal expansion causes a mechanical motion. Bimorph actuators are more common since they use the difference in the thermal coefficient of expansion of the two materials for the desired actuation. A bi-directional vertical thermal actuator [24] used in RF systems can

5

be actuated when the current is passed through the anchors of the hot and cold arms and its direction of motion can be controlled based on which anchor the current passes as shown in Figure 1.4.
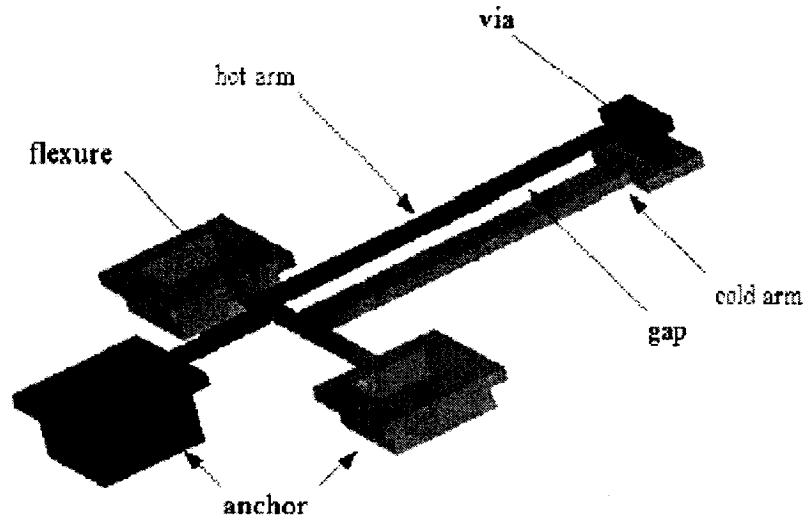
Fig 1.4 A 3-Dimensional schematic view of a vertical thermal actuator [24]

Hydraulic actuation is also used nowadays as they have the ability to produce high force actuations even though difficulties might arise in the choice of design parameters. A microgripper [25] actuated hydraulically has been studied and is based on the principle of a bourdon tube in which the liquid inside the tube is expanded thermally by means of external heating source. These actuators show favorable results and they are compared with shape memory alloy (SMA) actuators.

A combination of two or more actuating principles is also being used nowadays in the case of more complex MEMS structures where one of the actuation types is dominant

6

over the others. Electro-Thermo-Mechanical (ETM) actuator [26] is one such type where a thermal bimorph actuator is fabricated using poly-Multi User MEMS Process System (poly MUMPS). The actuator is given an electric current or voltage producing Joule's heat which leads to a temperature rise and the subsequent mechanical force.

Each of the above mentioned actuation techniques have been employed successfully in the MEMS industries based on their applications and suitability [27]. However, the electrostatic actuation method is one of the most frequently used actuation methods. The phenomenon of electrostatic actuation, along with its advantages, drawbacks and applications are explained below in the subsequent section.

1.3 Electrostatic Actuation

Electrostatic actuation makes use of the Coulomb forces developed between two capacitively coupled conductors across which a voltage is applied. Of all the actuation methods in MEMS, electrostatic actuation is the most widely used because of the following advantages [3]:

(i) Scaling laws favour electrostatic actuation rather than magnetic in micro range.

(ii) Simplicity in operation as it is actuated by just two electrodes and air gap.

(iii) Lower weight and power consumption.

(iv) It is driven by voltage and voltage switching is easier compared to that of electromagnetic actuation where current is used as the driving parameter. Electrostatic

7

actuation needs lower actuation voltage when compared to that of electromagnetic actuation.

(v) The possibility of miniaturization is high and their IC compatibility is excellent.
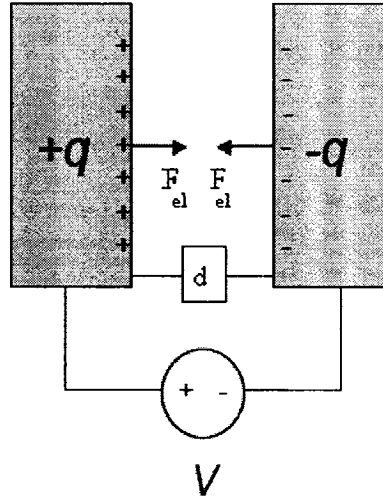
Fig. 1.5 Principle of electrostatic actuation

As shown in Figure 1.5, when a voltage 'v' is applied between the two plates, electrostatic actuation occurs which makes the movable plate to deflect towards the fixed plate due to the attractive forces between them. The electrostatic force that attracts the plates together is given by the Equation 1.1 as

$$F_{el} = \frac{\varepsilon_0 \varepsilon_r A V^2}{2(d-x)^2}$$

1.1

where

$\varepsilon_0 = 8.854 \times 10^{-12} \, F/m$, permittivity of vacuum

$\varepsilon_r = 1$, relative permittivity for air

A, area of the plate, m^2

V, voltage applied between the moving plate and the bottom plate, volts

d, initial gap between the top and the bottom plate, m

x, displacement of the moving plate, m

From Equation 1.1, it is clear that the electrostatic force is nonlinear due to the nonlinear deflection and hence a slight increase in voltage might result in a very large force and a large resulting deflection. For smaller gaps between the top and bottom electrodes, the deflection can be assumed to be linear and analysed accordingly. Even though linear analysis would give only an approximate solution, the difference between the exact and approximate solution is minimum such that it can be neglected. In the case of larger gaps between the two electrodes, the deflection value is so large that it can no longer be treated as linear for further analysis.

The better performance of MEMS structures when using electrostatic actuation also depends on the selection of materials [28], device geometry and residual stress state [29]. For example, the stiffness, mass, electrical resistivity, mechanical quality factor, stiction, fatigue resistance and shock reliability are some of the material selection criteria which have to be chosen accordingly for specific applications. The temperature during fabrication may not be the same when the device is in operation and drastic variations can cause low performance of the device [30].

Even though electrostatic actuation has certain advantages over other methods as mentioned before, there are some limitations involved in using it which cannot be

ignored. For example, when the voltage applied across the structure increases, the electrostatic force acting on it also increases and at a particular value of the voltage, the structure fails. This voltage is called as the 'pull-in voltage' [31]. Hence electrostatic actuation cannot be used for larger range of operation, in order to avoid this phenomenon. This pull-in instability is one of the main limitations that the researchers have to keep in mind while designing and operating structures using electrostatic actuation. The pull-in phenomenon in MEMS structures and its effects will be explained in the next section.

Another limitation of applying electrostatic actuation on MEMS structures includes the contamination of gap between the top and bottom electrodes as they are highly sensitive to dust and humidity [32]. Hence various efforts have been taken so far [33, 34] to prevent this contamination.

1.4 Pull-In Instability

In the model explained in Section 1.3, an electrostatic force is acting on the structure due to the application of voltage. The electrostatic force is counteracted by the mechanical force provided by stiffness properties of the structure. Hence the mechanical force restores the static equilibrium of the structure and brings it back to its original position. The electrostatic force is nonlinear as it is directly proportional to the square of voltage and inversely proportional to the square of deflection or change in the gap which can be seen from Equation 1.1. The stiffness of the structure times its deflection gives the restoring mechanical force and hence it is linear with the change in deflection.

When the voltage applied on the structure is increased, the deflection also increases and the gap between the two electrodes decreases. The electrostatic force increases nonlinearly to a higher value whereas the mechanical force increases in a linear fashion for the same deflection as explained previously. As the voltage is increased further to a particular value, both the mechanical and electrostatic forces seem to be equal and they balance each other to maintain the static equilibrium position of the structure. When the mechanical restoring force can no longer withstand the electrostatic force due to any further increase in the voltage, the structure snaps with the bottom electrode. This particular value of voltage is called as the 'pull-in voltage' and voltages above this pull-in value leads to failure of the device.

Nathanson [31] proved that for a simple mass-spring model, when the deflection is around one-third of the total initial gap, the structure fails and termed that particular voltage as the "pull-in voltage" and beyond this voltage, the steady state solution ceases to exist. Since then, different analytical, numerical and experimental works have been done to study this pull-in instability. Bernstein et al [35] proved the existence of a bifurcation point at pull-in, where the microdevice deflection becomes unstable. Pelesko [36] proved that when the deflection of a device with complex geometries is plotted against the applied voltage, the resulting plot is not the same single fold bifurcation diagram that are obtained for systems which are no longer in their steady state. This is shown in Figure 1.6.
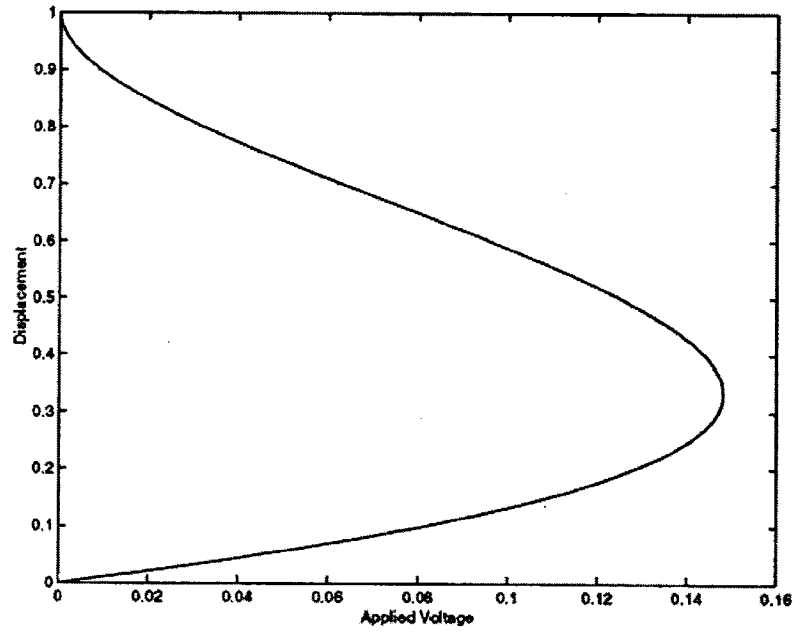
Fig. 1.6(a) Bifurcation plot for simple geometries [33]
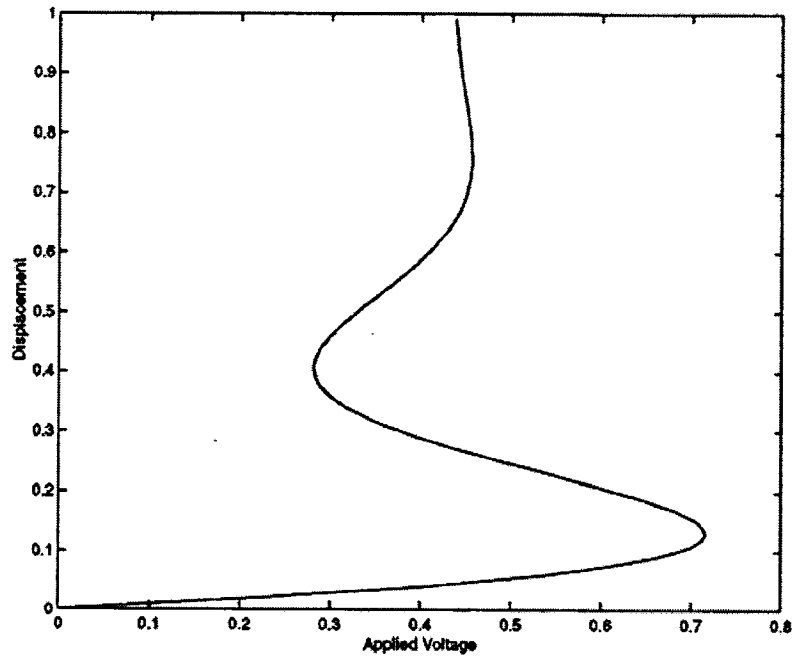
Fig. 1.6(b) Bifurcation plot for complex design geometries and electrode spacing [36]

12

It is also shown that pull-in in the case of a fixed-fixed and fixed-free beams correspond to 0.4 and 0.45 of the total initial gap and not one-third as in the case of mass-spring model type structures as explained in previous papers [37]. Thus the effect of pull-in instability on the actuation of electrostatic devices was shown. Different control techniques are carried out to extend the travel range beyond the pull-in limit or even avoiding the failure of the device when it touches the bottom electrode by various researchers and will be explained later in the next chapter.

1.4.1 Linear analysis approach

Analysis of electrostatic MEMS devices is challenging because the classical structural dynamics methodology is not easily applicable to the type of forcing and nonlinearities encountered. A common approach in the literature is to assume a linear relationship between the excitation force and the deflection. The linear equation is then solved by numerical methods, such as the Galerkin method, Rayleigh-Ritz method, the finite-element method.

Galerkin approximation has been applied to reduce the partial-differential equations of motion into a finite-dimensional system of nonlinearly coupled second-order ordinary differential equations for a microplate [38]. The developed linear model is then validated by comparing the results with those obtained experimentally and with those obtained by solving the distributed parameter system. The linear mathematical modeling of the microdevices is also done using the normal mode approach obtained by applying

boundary characteristic orthogonal polynomials in the Rayleigh–Ritz method from which the natural frequencies and mode shapes are obtained [39]. The comparison between theoretical and experimental results shows a little deviation and has been attributed to the microfabrication process limitations and foundry tolerances.

The pull-in behavior of a cantilever and fixed-fixed beam type electrostatic microactuators is studied using the capacitance-based analytical method and FEM simulations are also done to compare the pull-in position [40]. The normalized pull-in position for cantilever beams is found to be 0.470 times the initial gap by capacitance-based analytical method and 0.472 times the initial gap by finite element method. For the fixed beams, they are found to be 0.42 of the initial gap from both these methods. A linearized uniform approximate closed-form model is proposed to determine the pull-in voltage of a cantilever beam under uniform nonlinear electrostatic pressure [41]. The evaluated pull-in voltage for the cantilever beam has a maximum deviation of ±2% for wide beams, and a maximum deviation of ±1% for narrow beams from the Finite Element Analysis (FEA) results obtained from Coventor [42].

These are some of the methods that are used to linearize the electrostatic phenomenon. Even though the results obtained using these methods are not exact, the approximation holds good for structures undergoing smaller forces and hence smaller deflections. Linear analysis can be applied mainly for mechanical and optical switching purposes as the operation of the device for these applications do not have to deal with the stable and unstable regions and their effects.

1.4.2 Non linear analysis approach

The pull-in instability in MEMS structures is due to the nonlinear electrostatic force acting on the system as discussed before. For cases where the gap between the two electrodes are smaller resulting in smaller deflections, the nonlinearity can be ignored and the system can be analysed based on linear methods as explained in the previous section. But when the force applied and the subsequent deflection are larger, nonlinearity creeps into the system so much that they have to be considered for understanding the behaviour of the system. Significant work has been done so far using different methods to study the nonlinearity due to the increasing use of electrostatic actuation for MEMS structures for various applications.

The dynamic characteristics of nonlinear electrostatic pull-in behavior for a fixed–fixed beam are studied [43] and its natural frequencies are calculated using the differential quadrature method (DQM). This model included the nonlinear interaction between the curved electrostatic field force and the shaped micro-beam, as well as the mid-plane stretching, axial residual stress and electrical field fringing effect. The analytical results and the measured data shows good agreement and the analytical results also show that the shaped micro-beam with curved electrode can increase the working voltage range approximately six times compared to the rectangular micro-beam and flat electrode.

A Finite Element Method (FEM) based on a Sequential Field Coupling (SFC) approach in which electrostatic loads are gradually applied to the deformed shape of the micro

structure is proposed by Collenz et. al [44]. This model holds good for larger deflections where the geometric nonlinearities are dominant and hence the electrostatic load increments are given iteratively at different points of the deflection and an alternative option has also been presented by increasing the applied voltage incrementally by iteration.

A nonlinear modal analysis approach based on the invariant manifold method is applied to perform the dynamic analysis of a micro switch [45]. Both the geometric nonlinearity of the micro beam associated with large deflection and the nonlinear coupling between the two energy domains are considered and the nonlinear partial differential equation is decoupled into a set of nonlinear ordinary differential equations using the Galerkin technique. The results obtained show agreement with the finite difference method results and prove that accurate results are obtained without spending much computational time.

A nonlinear Mathieu equation is used to study the parametric resonance of an oscillator whose nonlinearity is due to both the electrostatic force and the structural nonlinearity due to the spring [46]. A two variable method has been applied to analyse the system and the results are compared with the experiments and a significant change in the parametric resonance has been observed due to the nonlinearity. Based on these results, an appropriate working mode for the mass sensor has been found out with its sensitivity independent of damping.

16

Period doubling and chaos in a simulated MEMS cantilever system with electrostatic sensing and actuation, intended for a MEMS based mass storage chip has been found out by [47]. A graphical interface has been used for the Poincare method to simulate multiple initial conditions simultaneously. The stable operation range was significantly reduced, by 25%, because of the chaotic response in a particular case. The dynamics of a micromechanical switch based on the bistable Anharmonic Casimir Oscillator (ACO), executing undamped periodic motion, are studied using numerical and analytical solutions of the differential equation of motion [48]. The tremendous change in the frequency and amplitude values due to the casimir effect has been explained and this extreme sensitivity due to ACO has been given as a platform for designing sensitive sensors and detectors.

The nonlinear dynamics of a mass-spring model has been presented based on the energy analysis and an analytical AC pull-in condition has been achieved [49]. The stable and unstable oscillations of the system has been studied by plotting the potential and kinetic energy curves for varying values of AC and DC voltages. A combination of maximum AC and DC voltages that can be applied to actuate the system without producing snapping at resonant frequency has been evauated.

The nonlinear response of a micro tweezer has been analyzed by using a hybrid Boundary Element and Finite Element Method (BEM/FEM) approach [50]. A modified Newmark method has been proposed to give accurate results for performing the time integration to obtain the nonlinear dynamic response of the system. The nonlinear behaviour of the

17

system and its responses due to the application of both the DC and AC signals have been obtained. The phase trajectories have been plotted and the three equilibrium positions from the plot are analysed to understand the stability of the system.

The simulation of transient and steady-state dynamics of microbeams undergoing small or large motions has been carried out in [51]. The frequency has been tuned in such a way that the system is excited near both the sub harmonic and the super harmonic excitations. The AC amplitude variation, DC bias and the damping has a significant effect on the frequency response curve in the case of super harmonic excitations whereas they do not have any effect for the case of sub harmonic excitations. The phase portraits are also plotted for both the stable and unstable regions and the effect of the pull-in voltage value on the plot has been studied. It has been concluded that the sub harmonic resonance of order one-half (twice the fundamental frequency) has the potential of being used to design a band pass RF filter with improved characteristics.

The transient dynamics of a micro beam under electrostatic actuation and squeeze film pressure has been studied with a special emphasis on stability analysis [52]. A model has been developed using the Galerkin procedure with normal modes as a basis and it accounts for the distributed nonlinear electrostatic forces, nonlinear squeeze film damping, and the rotational inertia of a mass carried by the beam. It has been seen that the presence of a nonlinear damping increases the dynamic pull-in voltage since higher initial energy required in order to cause instability and hence the velocity of the damped system is found to be higher at the beginning of the motion. The stable and unstable

regions due to the variation of the actuation voltage have been separated by a separatrix obtained in the phase plot and different phase portraits have been sketched for different voltage excitations close to the pull-in value and an extensive analysis has been done to study the nonlinear dynamics near the pull-in.

The complete nonlinear dynamics of a micro-electro-mechanical system with a time-varying capacitor has been investigated by Luo et al. [53]. The model analysed is the resonant gate transistor developed by [31] and the dynamic analysis has been done based on a specific conservative energy E_0 obtained from the invariant integration of the dynamic equation of the system and it has been used to find the natural frequency and other solutions such as phase portraits and equilibrium states for the system. From the phase portraits for different E_0 values and different voltages, different equilibrium points have been obtained and hence the pull-in voltage value (static analysis) has been evaluated.

The dynamic analysis has been done and the different equilibrium points obtained from the phase portraits have been used as the limits for the time integration where the elliptic integral of the third kind has been applied to find out the time period for the closed orbit and the frequency. The range of operation of the AC and DC voltages on the capacitor has been predicted in this dynamic analysis and various phase and frequency plots for different AC, DC voltages and E_0 values have been plotted and found to be in agreement with the experimental measurements. The dynamic analysis is also done for studying the

chaotic motion and the conditions have been inferred for the appearance and disappearance of the chaotic motion in resonant layers.

1.5 Objectives of the Thesis

The static and dynamic behaviour form the basis for designing the electrostatically actuated MEMS structure in order to achieve the desired performance and hence the necessity to understand the physical phenomenon. For highly sensitive applications such as sensors, actuators and filters, the stable operation of the device has to be achieved and the range of operation has to be predicted as accurately as possible. The pull-in instability leads to the system failure and hence an accurate prediction of the pull-in voltage and the dynamic frequencies are needed. Since the electrostatic actuation is a nonlinear phenomenon, linear approximations will not yield accurate results. Thus a nonlinear analysis is highly desirable for electrostatic MEMS structures.

The main objectives of this thesis are

(i) to study the electrostatic phenomenon and its pull-in instability in MEMS structures based on linear analysis and to understand its analogy to the aero elastic phenomenon.

(ii) to convert the continuous systems such as cantilever beams into equivalent lumped - mass-spring models based on their energy equations, since it is easier to perform the nonlinear analysis on the lumped model.

(iii) to perform the nonlinear static and dynamic analysis on the MEMS structures and predict the pull-in parameters and frequencies based on the phase portraits.

(iv) Microfabrication, experimental dynamic testing of the MEMS cantilever and validation with the analytical results.

1.6 Organization of the Thesis

The thesis is organized as follows:

1) Study on the electrostatic phenomenon in MEMS structures and the explanation of its similarity to the aeroelastic phenomenon in aircraft wing structures is given in Chapter-2.

2) Fabrication of the micro plates and micro cantilevers based on the MicraGeM process and the conversion of a continuous cantilever system into an equivalent mass-spring model are explained in Chapter-3.

3) An introduction to the nonlinear vibration analysis based on simple pendulum followed by the nonlinear analysis of two MEMS cantilevers, one compared with a published result and the other designed from the MicraGeM process, are presented in the Chapter-4.

4) Experimental dynamic testing set-up for the MicraGeM cantilevers is explained and the test results are presented in the Chapter-5 along with comparision.

5) The Chapter-6 presents conclusions based on the thesis work and future possible extensions to the present work.

Chapter 2

Analogy between Electrostatic MEMS and Aeroelastic Wing Structures

2.1 Introduction

An introduction to the electrostatically actuated MEMS structures has been given and the survey of work done about its mechanical performance and limitations, such as, pull-in and other instabilities have been explained in Chapter 1. In this chapter, the linear vibration analysis of a simple mass-spring model of an electrostatically actuated MEMS structure is explained to study the static and dynamic behaviour of the system. The understanding of pull-in instability is done through the mathematical equations and its physical significance is again emphasized. The instability phenomena occurring in electrostatically operated MEMS structures is very similar to those encountered in aeroelasticity. In order to benefit from the research on aeroelastic instabilities and their control, the aeroelastic phenomenon occurring on the aircraft wing structures is explained with a simple one degree of freedom wing model, and its divergence and flutter instabilities are studied. An analogy between the instabilities explained above in two different domains and the control methods adopted so far in both these fields are

presented. It is concluded that new terminologies can be given to the electrostatic MEMS based on the aeroelastic instabilities and control techniques.

2.2 Electrostatic Phenomenon: A Mass-Spring Model

As has been explained previously in Chapter 1, the electrostatic phenomenon in MEMS systems is nonlinear and there exists some complexity in dealing with this nonlinearity. Hence to understand the phenomenon initially, the nonlinear electrostatic force is linearised to solve for the deflection and the frequency. A simple mass-spring model is taken as shown in Figure 2.1 to understand the static and dynamic behaviour of the device.
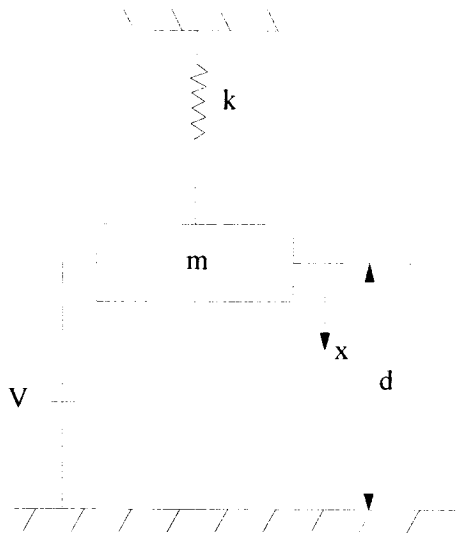
Fig. 2.1 A simple mass-spring model under an electrostatic force

The design parameters taken for the demonstration and the properties such as stiffness and mass are given in Table 2.1.

Table 2.1 Design parameters of the mass-spring model

ε_0 (F/m)	ε_r	L_1 (µm)	B (µm)	d (µm)	k (N/m)	m (kg)
8.85×10^{-12}	1	500	200	2	0.5	1×10^{-3}

The electrostatic force due to the voltage between the moving top plate and the fixed bottom electrode is given by

$$F_{el} = \frac{\varepsilon_0 \varepsilon_r A V^2}{2(d-x)^2}$$

(2.1)

The area of the plate (A) is A = Length (L_1) x Width (B) of the plate. The equation of motion of the system under the nonlinear electrostatic force is given as

$$m\ddot{x} + kx = F_{el}$$

(2.2)

or

$$m\ddot{x} + kx = \frac{\varepsilon_0 \varepsilon_r A V^2}{2(d-x)^2}$$

(2.2a)

For static equilibrium, the electrostatic force is balanced by the mechanical restoring force which is given by the Equation (2.3)

$$kx = \frac{\varepsilon_0 \varepsilon_r A V^2}{2(d-x)^2}$$

(2.3)

The Equation 2.3 is plotted as shown in Figure 2.2 which is a plot of mechanical and electrostatic forces against the displacement. It is seen that for each voltage value, the corresponding electrostatic force exactly balances the mechanical restoring force at two values of displacement. The first point which is stable, is termed as 'x_s' and called as the static equilibrium position. The second point is the unstable position termed as 'x_p' and is called as the pull-in position. At a particular voltage, both the positions 'x_s' and 'x_p'

become a single point (i.e. the electrostatic curve just touches the mechanical curve at a single point). This value of voltage is the pull-in voltage for the device. For the design parameters taken to analyse, the pull-in voltage is found to be 1.157V.
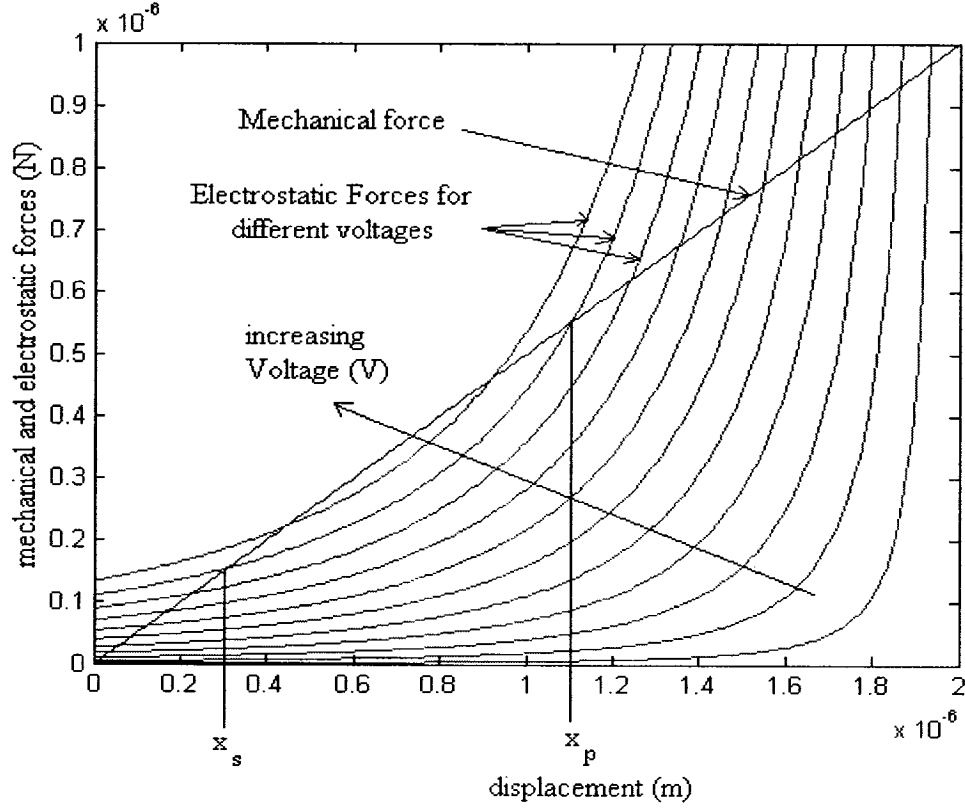
Fig. 2.2 Plot of mechanical and electrostatic forces against displacement

Even though the force balance plot can be used to see the pull-in voltage from the sketch, the mechanical behaviour of the device such as the deflection of the plate with an increase in voltage cannot be studied based on balancing the forces. Hence the static equilibrium Equation 2.3 has to be solved for the deflection. Since the electrostatic force on the right hand side of Equation 2.3 is nonlinear, the Taylor Series expansion with respect to zero deflection condition [54] is used to linearise it as given below.

$$\frac{\varepsilon_0 \varepsilon_r A V^2}{2(d-x)^2} = \frac{\varepsilon_0 \varepsilon_r A V^2}{2d^2}\left(1 + \frac{2x}{d} + \frac{3x^2}{d^2} + \ldots\right) \tag{2.4}$$

Considering that the device is undergoing only small deflections, the above equation can be approximated and introduced into the Equation 2.3 as

$$kx = \frac{\varepsilon_0 \varepsilon_r A V^2}{2d^2} + \frac{\varepsilon_0 \varepsilon_r A V^2}{d^3}x \tag{2.5}$$

The above equation is rewritten in terms of deflection as

$$x = \frac{\dfrac{\varepsilon_0 \varepsilon_r A V^2}{2d^2}}{\left(k - \dfrac{\varepsilon_0 \varepsilon_r A V^2}{d^3}\right)} = \frac{\dfrac{\varepsilon_0 \varepsilon_r A V^2}{2d^2}}{k - k^s_{elec}} \tag{2.6}$$

where k^s_{elec} is the equivalent electrostatic stiffness at static deflection. The deflection depends on the voltage and as the value of the voltage increases, the deflection also increases since the denominator decreases and the numerator increases in the Equation 2.6. The plot of the change in the gap between the top and bottom electrodes against the voltage for the design parameters taken for analysis is shown in Figure 2.3. It can be seen that the top plate is attracted to the bottom electrode as there is an voltage applied between them. As the voltage increases, the plate moves closer to the bottom electrode and at a particular voltage, the denominator of the Equation 2.6 becomes zero. At this voltage, the deflection becomes infinity which means that the top electrode touches the bottom electrode and results in the failure of the device due to a closed circuit. Hence there exists instability in the system which is called as the pull-in instability and the voltage at which this instability occurs is called as the pull-in voltage of the system.
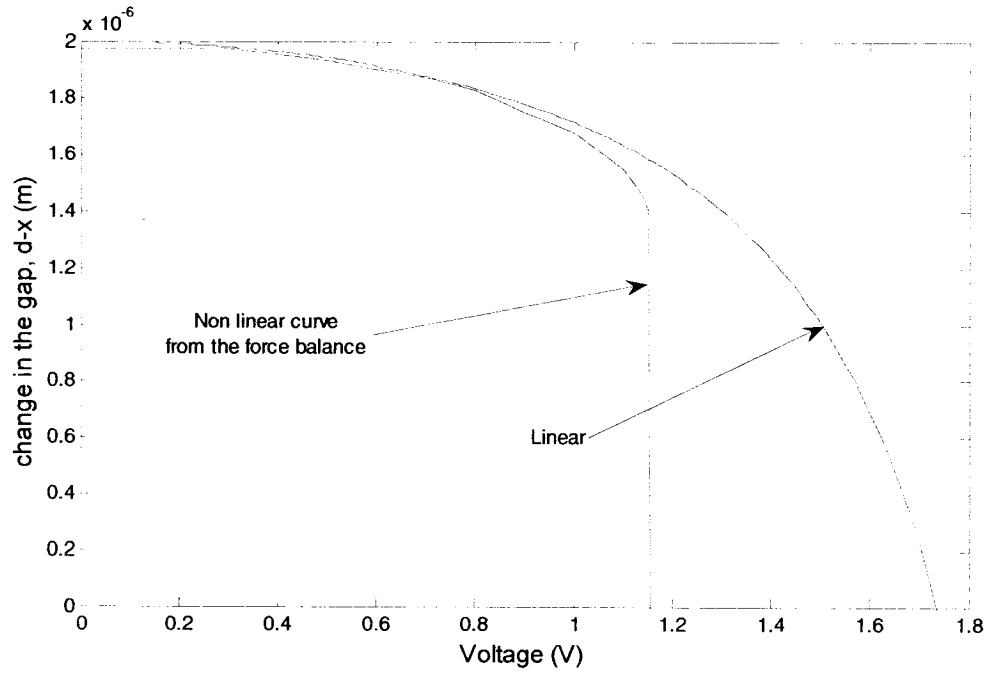
Fig. 2.3 Variation of the change in the gap against bias voltage

The pull-in voltage obtained for this system is found to be 1.739V which is not the same as that obtained from the force balance. This pull-in value is higher than the force balance value which is 1.157V since this is calculated based on the linearised approximation of the electrostatic force equation and a 33.5% reduction of pull-in voltage is obtained from the non linear analysis. Hence the device operation at voltages close to the pull-in value based on the linear model can cause the failure of the system even before the actual pull-in value calculated. Thus the linear model can be useful only for small deflections of the device for the safe operation as explained before.

The dynamic analysis of the mass-spring model is done to find the frequency of vibration under the electrostatic force. The dynamic equation of motion is given in Equation 2.2a.

By Taylor's series expansion with respect to the static equilibrium point, the equation of motion is reduced to the form

$$m\ddot{x} + \left(k - \frac{\varepsilon_0\varepsilon_r AV^2}{(d-x_{st})^3}\right)x = \frac{3}{2}\frac{\varepsilon_0\varepsilon_r AV^2}{(d-x_{st})^4}x^2 \tag{2.7}$$

where x_{st} is the static deflection position obtained from the static equilibrium analysis, x is the dynamic motion. The above Equation 2.7 is a forced vibration equation. After substituting Equation 2.3, the free vibration problem can be considered as

$$m\ddot{x} + \left(k - \frac{\varepsilon_0\varepsilon_r AV^2}{(d-x_{st})^3}\right)x = 0 \tag{2.8}$$

Thus the natural frequency is obtained as

$$\omega_n^2 = \frac{\left(k - \frac{\varepsilon_0\varepsilon_r AV^2}{(d-x_{st})^3}\right)}{m} \tag{2.9}$$

or

$$\omega_n = \sqrt{\frac{\left(k - k^d{}_{elec}\right)}{m}} \tag{2.10}$$

In the Equation 2.10, $k^d{}_{elec}$ is the equivalent electrostatic stiffness for dynamic motion due to the electrostatic force. When the value of the voltage is increased, the electrostatic stiffness also increases and hence the frequency is reduced. Thus, at a particular value of the voltage, the electrostatic stiffness is equal to the mechanical stiffness and the value of the frequency becomes zero. The plot of frequency against the voltage is shown in Figure 2.4. Thus the influence of electrostatic actuation on the MEMS structures has been explained and the instabilities such as *pull-in voltage* and *zero frequency voltage* have been emphasized based on performing the static and dynamic analysis. This electrostatic

phenomenon is similar to the aeroelastic phenomenon in the case of aircraft wing structures which is explained in the subsequent section.
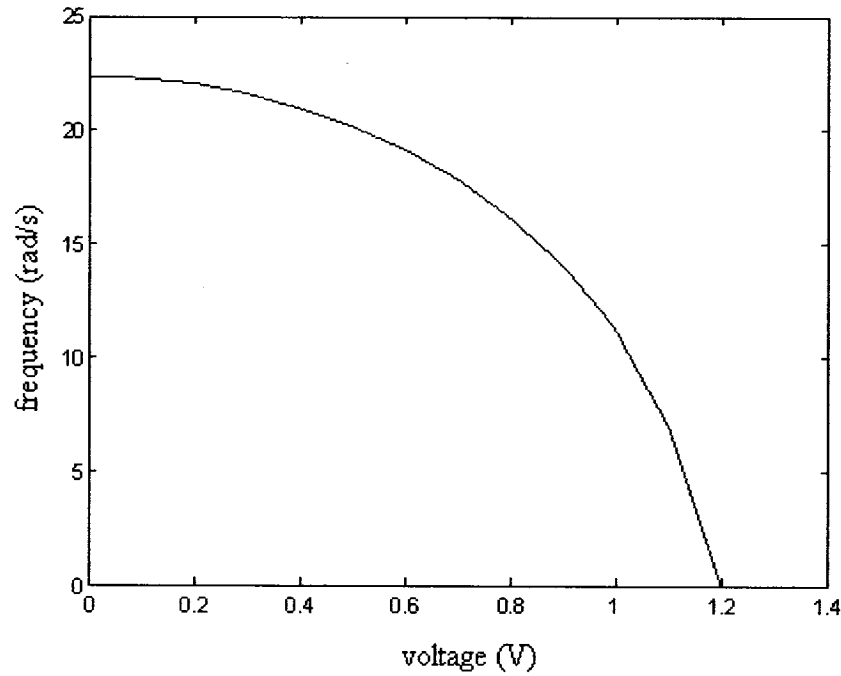
Fig 2.4 Frequency against voltage for the mass-spring model

2.3 Aeroelastic Phenomenon: 1-D Wing Model

Aeroelasticity is the discipline concerned with the mutual interaction of structural, aerodynamic and inertial forces on a flexible solid body moving through a fluid [55]. The aerodynamic forces acting on the aircraft wing structures cause vibrational instabilities which in turn lead to the failure of the wing structure. This has been a major area of research for the last 50 years and efforts have been taken to avoid these instabilities for the safe operation of the aircraft. Static and dynamic analysis on a simple wing model is given in this section to get an overview of the problem. It will be seen that there is a

similarity between this aeroelastic phenomenon in wing structures and the electrostatic phenomenon in MEMS structures. Hence in this section, the static and dynamic vibrational instabilities occurring on the aircraft wing structures is explained based on a single degree of freedom model [55].

A simple line diagram showing the cross-sectional view of an aircraft wing is given in Figure 2.5 below. Here, only one degree of freedom is considered, the rotational degree of motion (α), as shown in the Figure 2.5. The horizontal line defined by point 'O' is the elastic axis about which the rotation of the wing structure takes place. The elevated line is the simple line diagram of the cross-sectional view of cantilevered wing structure with ' K_α ' as the rotational stiffness of the wing structure acting at O. L is the aerodynamic lift force acting on the wing at the aerodynamic center (A.C) which is the point about which the pitching moment acting on the airfoil is constant regardless of the angle of the attack (α). The angle of attack α can be expressed as

$$\alpha = \alpha_0 + \alpha_e \qquad (2.11)$$

α_0 is the initial angle of attack and α_e is the elastic twist due to the aerodynamic lift force.
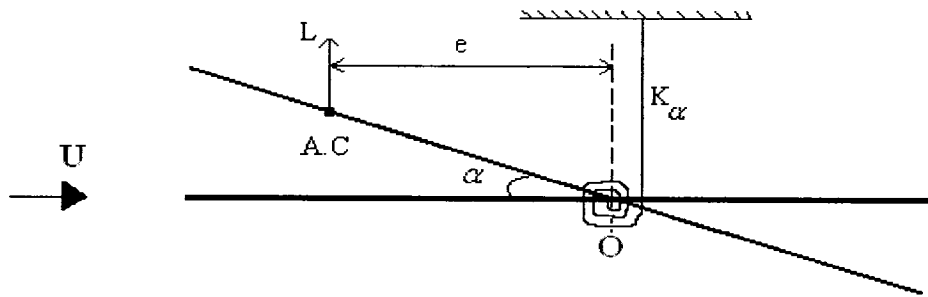
Fig. 2.5 Cross-sectional view of a simple line diagram of an aircraft wing model

The eccentricity e is the distance of the aerodynamic center from the point O. the fluid acting on the wing surface which is air in this case, moves with a velocity U due to which there is an aerodynamic lift force L acting in the upward direction at the point A.C. Hence this aerodynamic moment due to the lift force acting on the wing has to be balanced by the restoring moment due to the rotational stiffness of the wing. Hence for moment equilibrium,

$$M_y - K_\alpha \alpha_e = 0 \tag{2.12}$$

M_y in the Equation 2.12 is the moment about the elastic axis, O, which is given below as

$$M_y = M_{AC} + Le \tag{2.13}$$

M_{AC} is the moment about the aerodynamic center which is written as

$$M_{AC} = C_{MAC} \cdot qSc \tag{2.14}$$

where C_{MAC} is the moment coefficient about the aerodynamic center which reduces to $C_{MAC} = C_{MAC_0}$, since C_{MAC} does not change with α. S is the wing area and c is the mean chord length. The dynamic pressure acting on the wing is denoted by 'q'. The lift L in the Equation 2.13 is written as

$$L = C_L Sq \tag{2.15}$$

where C_L is the lift coefficient which varies with α. Using Taylor's series expansion, the lift coefficient is defined as

$$C_L = \left[C_{L_0} + \frac{\partial C_L}{\partial \alpha} \alpha \right] \tag{2.16}$$

Thus, $L = \left[C_{L_0} + \frac{\partial C_L}{\partial \alpha} \alpha \right] Sq \tag{2.17}$

31

In the above Equation 2.17, q is the aerodynamic dynamic pressure acting on the wing

which is written in terms of speed as $q = \dfrac{1}{2}\rho_1 U^2$ where ρ_1 is the density of the fluid due

to which the aerodynamic lift on the wing occurs and U is the speed or velocity of the

fluid. In the aircraft structures, the fluid acting is the air or the wind flowing against the

wing surface as explained before. The initial coefficient of lift is termed as C_{L_0} and the

lift curve slope as $\dfrac{\partial C_L}{\partial \alpha}$. For simple linear analysis, it is assumed that $C_{L_0} = C_{MAC_0} = 0$

which are the initial conditions. Hence Equation 2.12 reduces to the form,

$Le - K_\alpha \alpha_e = 0$.

$$qSe\frac{\partial C_L}{\partial \alpha}\alpha_0 + qSe\frac{\partial C_L}{\partial \alpha}\alpha_e - K_\alpha \alpha_e = 0 \qquad (2.18)$$

which can be rewritten in terms of the elastic angle of attack as

$$\alpha_e = \frac{qSe\dfrac{\partial C_L}{\partial \alpha}\alpha_0}{K_\alpha - qSe\dfrac{\partial C_L}{\partial \alpha}} = \frac{qSe\dfrac{\partial C_L}{\partial \alpha}\alpha_0}{K_\alpha - K_{aero}} \qquad (2.19)$$

where $K_{aero} = qSe\dfrac{\partial C_L}{\partial \alpha}$. The denominator in the above Equation 2.19 reduces as the value

of the dynamic pressure acting on the wing surface increases and hence the elastic angle

of attack α_e increases. At a particular value of the dynamic pressure (which in turn is

related to the dynamic speed), the rotational stiffness value is equal to the stiffness due to

the aerodynamic lift (K_{aero}) and the denominator becomes zero. Thus the value of the

elastic angle of attack becomes infinity which means that the wing structure breaks. This

maximum dynamic pressure that can be applied on the system is called as the divergence

pressure 'q_{div}' and hence the corresponding maximum speed which can act on the wing structure is called as the divergence speed 'U_{div}'. Hence the divergence is a static instability occurring on the wing structures and the failure of the structure happens when the velocity of the air acting on the surface is above the divergence speed. An example of the divergence curve is shown in Figure 2.6 which is plotted between the elastic angle of attack (α_e) against the divergence pressure (q) for the design parameters given in Table 2.2.

Table 2.2 Design parameters of the aircraft wing structure

S (m²)	e (m)	$\dfrac{\partial C_L}{\partial \alpha}$	α_0	K_α (Nm)	I (kg-m²)
1	0.1	6.28	5°	20	0.1
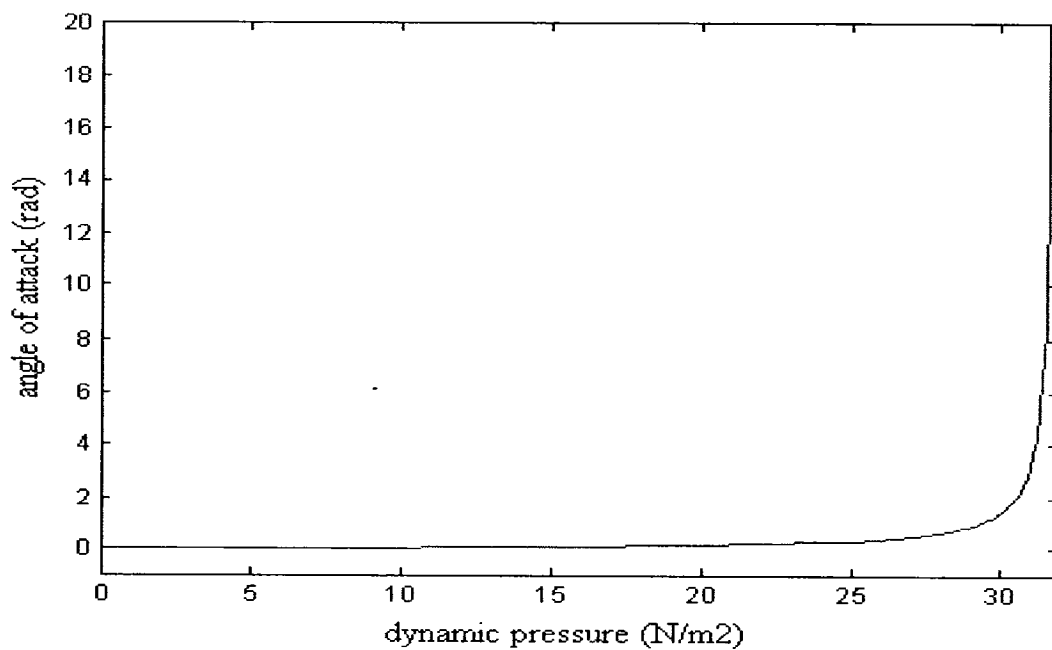
Fig. 2.6 Variation of the elastic angle of attack (α_e) against dynamic pressure (q)

The equation of motion under the aerodynamic force is written as

$$I\ddot{\alpha}_e + K_\alpha \alpha_e = M_y \tag{2.20}$$

In the above equation, I is the moment of inertia about the point O. Substituting for M_y from the Equation 2.13 into the above equation,

$$I\ddot{\alpha}_e + K_\alpha \alpha_e - qSe\frac{\partial C_L}{\partial \alpha}\alpha_e = qSe\frac{\partial C_L}{\partial \alpha}\alpha_0 \tag{2.21}$$

The above equation is a forced vibration problem. Hence to find the natural frequency, the free vibration equation as shown below in the Equation 2.22 has to be considered.

$$I\ddot{\alpha}_e + (K_\alpha - qSe\frac{\partial C_L}{\partial \alpha})\alpha_e = 0 \tag{2.22}$$

Hence the frequency of vibration under the aerodynamic force can be obtained as

$$\omega = \sqrt{\frac{K_\alpha - qSe\frac{\partial C_L}{\partial \alpha}}{I}} = \sqrt{\frac{K_\alpha - K_{aero}}{I}} \tag{2.23}$$
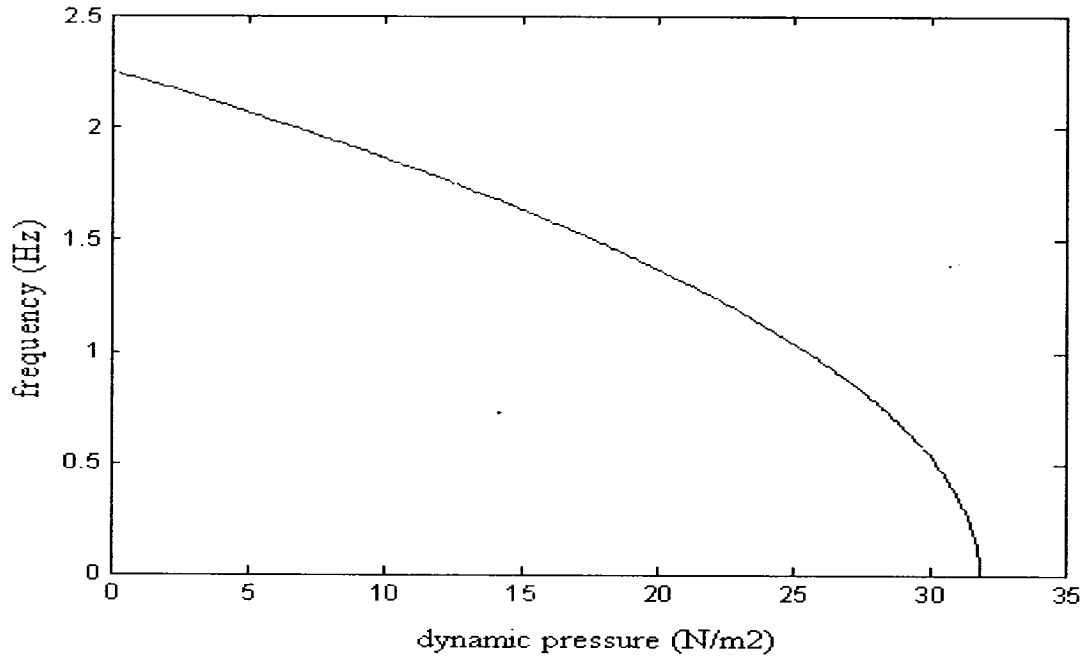
Fig. 2.7 Variation of frequency against dynamic pressure

34

One can see from Figure 2.7 that the increase in dynamic pressure or the speed results in the increase of K_{aero} leading to elastic weakening similar to that of electrostatic softening. Large increase in speed could make the net stiffness zero ($K_\alpha = K_{aero}$) leading to zero frequency condition. Hence the static and dynamic analysis of a single degree of freedom wing model is analyzed and the instabilities are studied.

2.4. Flutter

In the case of two degree of freedom wing model as shown below in Figure 2.8, where both the bending and twisting motions are considered, flutter types of instabilities are caused.
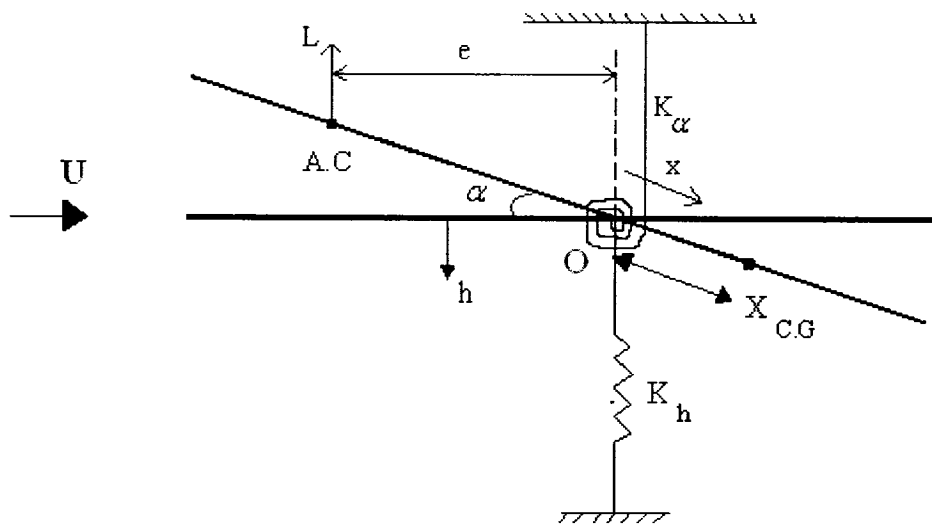
Fig. 2.8 Two degree of freedom wing model

The equations of motion for both the bending and twisting motions are

$$m\ddot{h} + S_\alpha \ddot{\alpha} + K_h h + qS \frac{\partial C_L}{\partial \alpha} \alpha = 0 \qquad (2.24)$$

$$I_\alpha \ddot{\alpha} + S_\alpha \ddot{h} + K_\alpha \alpha - qSe \frac{\partial C_L}{\partial \alpha} \alpha = 0 \qquad (2.25)$$

where 'h' is transverse displacement and 'K_h' is transverse stiffness. 'I_α' is the rotational moment of inertia whereas 'S_α' is the moment of area. Thus, flutter types of instabilities are seen when solving for the translational and rotational motions. Similarly, in MEMS structures, when the slenderness ratio (length to width) is small, (i.e.) when the rotational motion is significant, flutter type of instabilities has to be considered. But, usually in the case of micro cantilevers and microstructures, the slenderness ratio is quite large compared to the wing structures, (i.e.) l / b>>>1, the flutter type of instability is not a significant problem. In the next section, the control techniques that have been adopted in both these fields to avoid their respective instabilities will be discussed.

2.5 Control Methods

Since these instabilities cause the failure of the structures, different control methods that have been employed to avoid the instabilities so far in both these fields of MEMS and aeroelasticity are explained in this section. First, the control methods employed so far for the aeroelastic phenomenon are explained and then the methods in electrostatic phenomenon are discussed.

2.5.1 Aeroelastic control techniques

The efforts that have been taken so far to increase the divergence and flutter speeds or even eliminating these instabilities can be broadly classified as (i) active and (ii) passive control methods. Examples of these methods that have been explained by some previous research works is discussed below.

2.5.1.1 Active control

Active control can be explained as the real time monitoring and control of the aircraft wing vibrations by different techniques and feedbacks. The effective deployment of control surfaces [56] and different techniques to employ these flaps to adjust the speed of the aircraft are some of the common active control techniques. Also, the concept of piezoelectric material being deposited on the surface of the wing to actively control the wing deflections and their suppression of the instabilities has been studied [57] and applied successfully.

2.5.1.2 Passive Control

The passive control of the instabilities in the wing is done based on the concept of "aeroelastic structural tailoring" [58] which is the effective way of avoiding the divergence and flutter instabilities so far in the aircraft wings. Aeroelastic tailoring can be defined as the embodiment of directional stiffness into an aircraft structural design to

control aeroelastic deformation, static or dynamic, in such a fashion as to affect the aerodynamic and structural performance of that aircraft in a beneficial way. In the conventional wing, metallic surfaces are used such that their stiffness properties do not vary throughout. But when a composite structural wing is used, their directional stiffness varies according to the fiber alignment on the surface and hence an effective bending-torsion stiffness coupling parameter can be obtained [59]. In the composite wing, both the top and the bottom surfaces are laminated with fibers and called cover sheets. The orientation of the fiber leads to a change in the torsional and bending stiffness properties of the entire surface. The fiber angle variation with the reference to elastic axis over a certain range can very well avoid the divergence phenomenon [60]. Figure 2.9 shown below depicts the possibility of the divergence tending to infinity for a particular range of fiber angle for a straight, back swept and forward swept composite wings. . At ply angles in the range of 90-110°, the divergence tends to infinity as shown below.
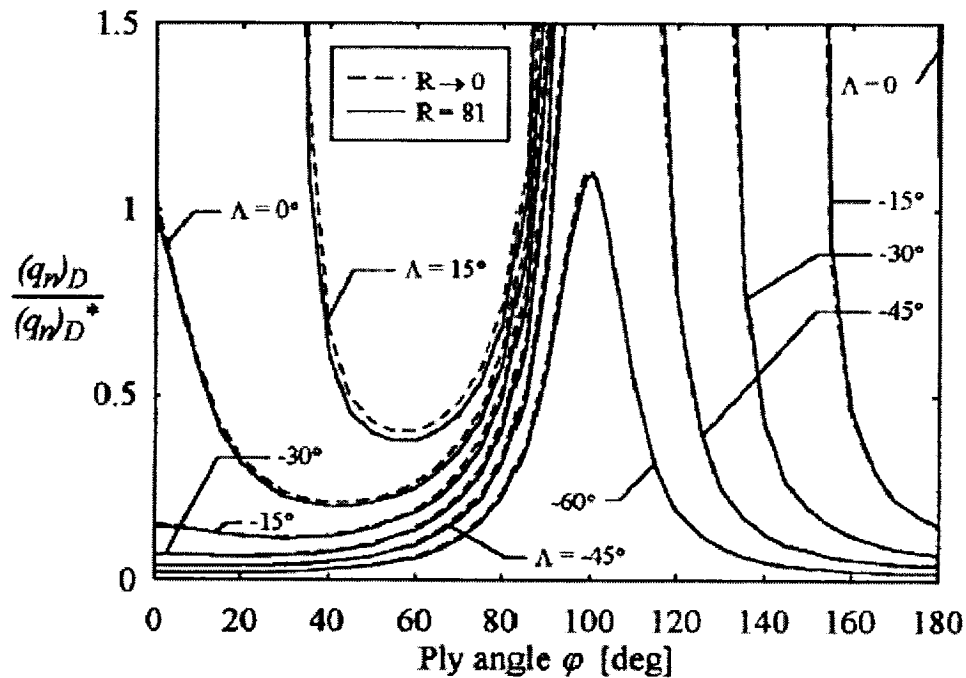
Fig. 2.9 Normalised divergence pressure against the fiber alignment angle [60]

Hence, it is inferred that the structural geometries can be optimized to passively control the instabilities. Thus an overview of both the active and passive control methods employed so far to avoid the instabilities in the aircraft wing structures has been given. In the section below, the control methods for avoiding the electrostatic structural instabilities are explained and based on their similarities with the aeroelastic phenomenon, they have been classified similar to the aeroelastic control methods, namely the active and passive control methods.

2.5.2 Electrostatic control techniques

Based on the aeroelastic terming of the control methods, the methods applied to control the pull-in instabilities in the electrostatic phenomenon can also be termed broadly as (i) active and (ii) passive control methods.

2.5.2.1 Active control

Active control can be defined as the controlling of the pull-in voltage of the system when the system is under the electrostatic actuation and also increasing the pull-in values accordingly. Seeger et al. [61] showed that the pull-in can be avoided by the simple addition of a series capacitance. This is the method called as "Capacitive control mechanism" that has been applied commonly to avoid the pull-in by most of the researchers so far. Also, a voltage control algorithm that has been applied by Chu et al. [62] is based on the controlling of voltage based on a feedback loop that clearly monitors

the pull-in. It is proved that the deflection can be as high as two or three times the nominal gap when such a kind of feedback loop is used and the device being stable throughout. These are the two widely used active control methods so far in the MEMS structures.

2.5.2.2 Passive control

When the structural parameters of the designed structure are such that they increase the pull-in limit or even avoid the instability, then that type of control can be called as the passive control mechanism. The following are some of the important design considerations that have been optimized to increase the pull-in voltage range by many researchers: (i) aspect ratio (ii) varying electrode placement and also the spacing between the bottom electrodes and (iii) varying dielectric properties. It is shown that pull-in in the case of a fixed-fixed and fixed-free beams correspond to 0.4 and 0.45 of the total initial gap and not as one-third for the mass-spring model type structures when the effective stiffness of the beam is optimized by having smaller aspect ratios rather than the usual values [63]. A novel external electrode configuration has been applied by Rosa et al. [64] to avoid the pull-in voltage at any point of the deflection in the case of a cantilever beam. In this model, in contrast to the traditional configuration, the suggested configuration consists of electrodes that are laterally offset from the actuated member. When a dielectric isolating layer is coated on one or both the electrodes, the residual charges that get deposited on the structure is a parameter that increases the pull-in voltage as shown by Degani et. al [65]. In their work, it is also proved that pull-in can be avoided according
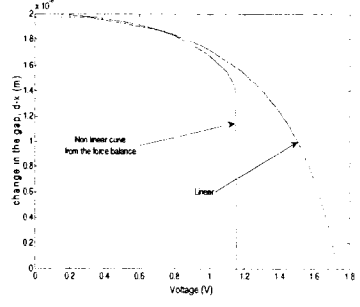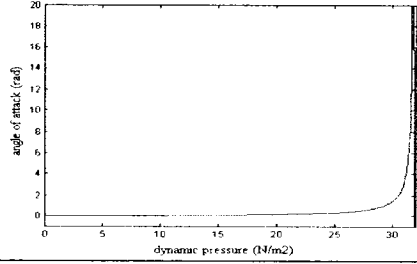
to the residual charge distribution on the coated layer. Thus the above mentioned passive control methods are some of the techniques that have been applied so far in avoiding pull-in instabilities in MEMS structures.

Hence the control methods adopted to deal with the instabilities in electrostatic MEMS structures have been discussed based on some of the work done so far. In the next section, the analogy between the two phenomenon, electrostatic and aeroelastic instabilities, is explained. The control methods employed in these fields are also compared and new terming of the electrostatic instabilities and control methods are proposed.

2.6 Analogy of Electrostatic MEMS and Aeroelastic Wing Structures

It can be inferred from the two previous sections that there is a similarity in the type of instabilities occurring in two different fields. The similarity between the electrostatic phenomenon in the MEMS structures and the aeroelastic phenomenon in the aircraft wing structures is studied and compared in this section. The following are the points that are summarized as shown in Table 2.3 which gives the analogy between the two phenomenon.

Table 2.3 Analogy between the electrostatic phenomenon and aeroelastic phenomenon in

MEMS and aircraft wing structures

S No	Analogy	Electrostatic phenomenon in MEMS structures	Aeroelastic phenomenon in aircraft wing structures
1	Static instability	When the voltage applied between the electrodes is increased beyond a particular voltage called the "pull-in voltage", the structure fails. 	When the aerodynamic velocity acting on the wing is increased beyond a critical value called the "divergence speed", the structural restoring force can no longer be able to withstand the aerodynamic force and the structure fails.
2	Phenomenon	Pull-in or touch down	Divergence
3	Deflection equation	$x = \dfrac{\dfrac{\varepsilon_0 \varepsilon_r A V^2}{2d^2}}{\left(k - \dfrac{\varepsilon_0 \varepsilon_r A V^2}{d^3}\right)} = \dfrac{\dfrac{\varepsilon_0 \varepsilon_r A V^2}{2d^2}}{k - k^s{}_{elec}}$	$\alpha_e = \dfrac{qSe\dfrac{\partial C_L}{\partial \alpha}\alpha_0}{K_\alpha - qSe\dfrac{\partial C_L}{\partial \alpha}} = \dfrac{qSe\dfrac{\partial C_L}{\partial \alpha}\alpha_0}{K_\alpha - K_{aero}}$
4	Critical parameter	Voltage (V)	Dynamic pressure (q) or dynamic speed (U)
5	Frequency equation	$\omega_n = \sqrt{\dfrac{\left(k - \dfrac{\varepsilon_0 \varepsilon_r A V^2}{(d - x_{st})^3}\right)}{m}} = \sqrt{\dfrac{\left(k - k^d{}_{ele}\right)}{m}}$	$\omega = \sqrt{\dfrac{K_\alpha - qSe\dfrac{\partial C_L}{\partial \alpha}}{I}} = \sqrt{\dfrac{K_\alpha - K_{aero}}{I}}$

42

2.7 Electrostatic Terminologies

Based on the similarities discussed between the two fields in the previous section and shown in Table 2.3, new terms are proposed for the electrostatic instabilities and their control methods based on the aeroelastic instabilities and their control methods respectively in this section. The Table 2.4 shown below gives the new terminology that can be given for the MEMS domain.

Table 2.4 Similar terminologies for MEMS based on aeroelasticity

S No	Actual MEMS terminology	Proposed terminology based on aeroelasticity
1	"Pull-in voltage" from the static analysis	"Divergence voltage"
2	"Zero frequency pull-in voltage" from the dynamic analysis	"Zero frequency voltage"
3	Control methods such as capacitive and voltage control mechanisms	"Active control methods"
4	Control techniques based on design and geometric optimizations	"Passive control methods" and also "Electrostatic structural tailoring"

2.7 Summary

In this chapter, the pull-in instability due to electrostatic actuation in MEMS structures is explained based on the static and dynamic analysis of a simple mass-spring model. Then, the aeroelastic instabilities such as divergence and flutter occurring on the aircraft wing structures are explained for simple one and two degrees of freedom wing models respectively. The control methods taken so far by various researchers in both MEMS and aircraft wing structures to avoid the instabilities have been presented. Thus an analogy is

found out between the electrostatic and aeroelastic instabilities and new terminologies have been proposed for the electrostatic instabilities and their control methods based on the aeroelastic phenomenon.

Chapter 3

Microfabrication and Equivalent

System Formulation

3.1 Introduction

In Chapter 2, the linear analysis of electrostatic MEMS structures was carried out and the analogy between the aeroelastic phenomenon and the electrostatic phenomenon were highlighted. In the first half of this chapter, the feasibility of microfabrication of the electrostatic MEMS structures is discussed. In the second part, the conversion of a continuous cantilever system into a lumped mass-spring system has been derived.

3.2 Microfabrication: MicraGeM Process Overview

There are different methods of fabrication of MEMS structures, such as, isotropic dry etching with Xenon difluoride (XeF2), anisotropic wet etching with Tetra Methyl Ammonium Hydroxide (TMAH), Deep Reactive Ion Etching (DRIE) etc. Herein, the MEMS fabrication has been carried out on Silicon-On-Insulator material through MicraGeM process technology [66]. MicraGeM is an acronym for Micralyne Generalized

MEMS and is a technology offered to the Canadian Universities through the Canadian Microelectronic Corporation [67]. Through this technology, different structures such as microplates, micromirrors, microcantilevers etc. have been fabricated [68]. The following sections present briefly the MicraGeM process overview and the results of the fabrication have been presented through Scanning Electron Microscopy (SEM). MicraGeM is a Micro-Electro-Mechanical Systems (MEMS) prototyping process developed at Micralyne Inc [69]. This technology differs from traditional MEMS processes by the materials used in the process, and by its variable geometry. Herein, SOI device is bonded on top of pyrex substrate, with an option of designing an etch in the pyrex substrate, and metal electrodes both on top of the SOI and in the pyrex etch. Thus, through this technology, fully suspended MEMS devices can be produced and can be actuated with the presence of the metal electrodes. A process overview [66] of this technology is shown in Figure 3.1 in order to understand the steps involved in fabricating the micro systems and structures. A fabrication area of 9 mm x 5 mm was allotted for each of the designs submitted to the CMC for fabrication. Herein, the MicraGeM process was used for fabrication of different microplates under different boundary conditions. The different boundary conditions refer to the clamping of the different boundary edges of the plate. Different cantilevers were also fabricated on the same chip.

3.3 Fabrication Results

MEMSPro design tool is used for designing various micro plates and micro beams. The design is then sent to CMC for microfabrication and it took around four months to get

released micro devices in a packaged chip. The fabrication results of the electrostatic MEMS structures are presented through Scanning Electron Micrographs. Figures 3.2 to 3.8 show the SEM of different microplates fabricated under different boundary conditions and dimensions. The general

Metal Electrode

Glass Pyrex Wafer

1. The process begins with a Pyrex wafer. Metal electrodes and bond pads are patterned.

Silicon Handle

Single Crystal Silicon   **Buried Oxide Layer**

2. The SOI wafer (device layer down) anodically bonded to the Pyrex.

3. The silicon handle wafer and buried oxide layer are etched away.

4. The metal layer is deposited and patterned lithographically to release silicon microstructures.

Fig. 3.1 Steps involved in the microfabrication based on MicraGeM process [66]

overview of the microplates that are fabricated is seen in Figure 3.2 which shows the array of plates from the top. In Figure 3.3, free and fixed boundary supports of the micro plates have been captured through the SEM. Figures 3.4 and 3.5 show the variation in the

dimensions of the microplates from that of previous Figure 3.3, and also similar variations in the boundary supports. A cantilever type microplate is shown at the extreme left of Figure 3.6 where three edges are free and one end clamped. An extreme close view of the microplate showing a smooth surface finish is seen in Figure 3.7. The gap between the top and bottom electrodes is seen clearly in Figure 3.8 showing a shadow of the top surface falling on the pyrex wafer. In the following Figures, 'F' denotes the fixed end and the 'Fr' denotes the free end.
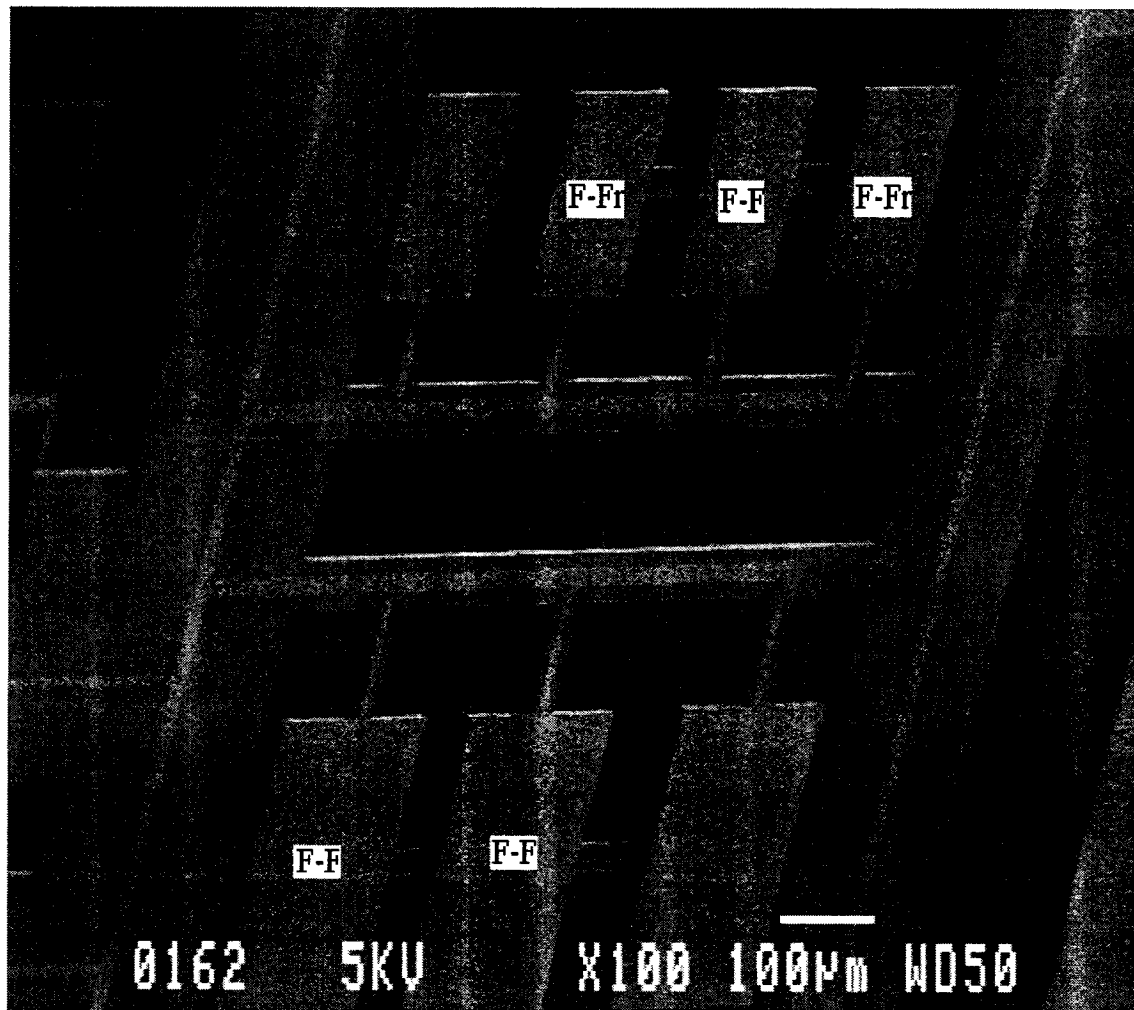
Fig. 3.2 General overview of the microbeams
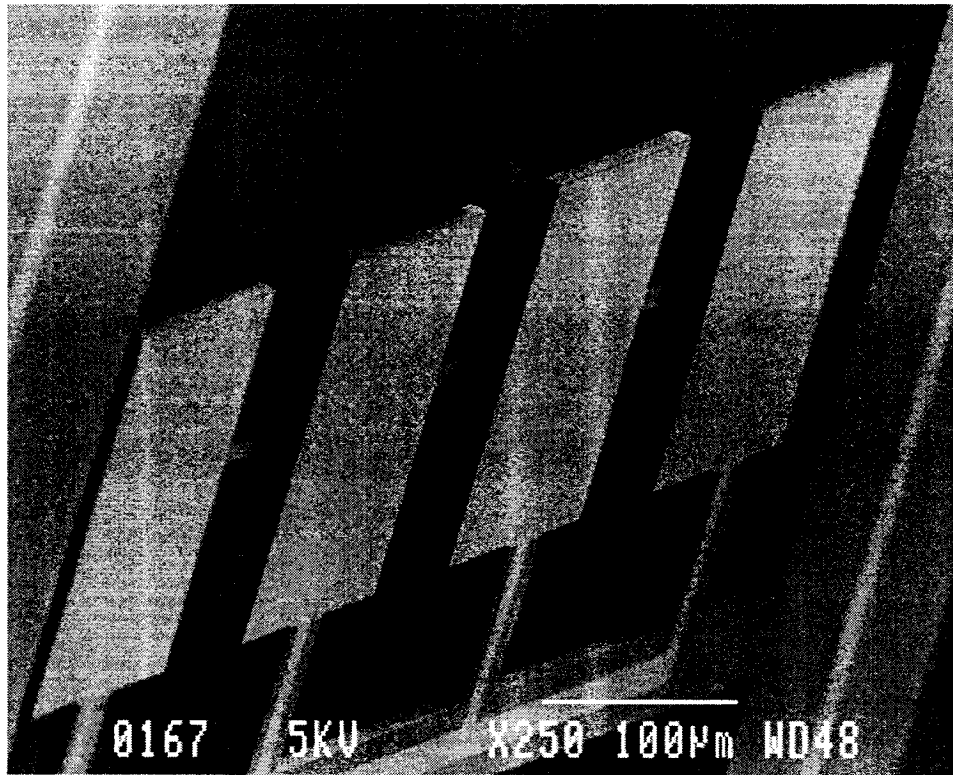
Fig. 3.3 Clear view of free and fixed boundary supports at the end of the plates
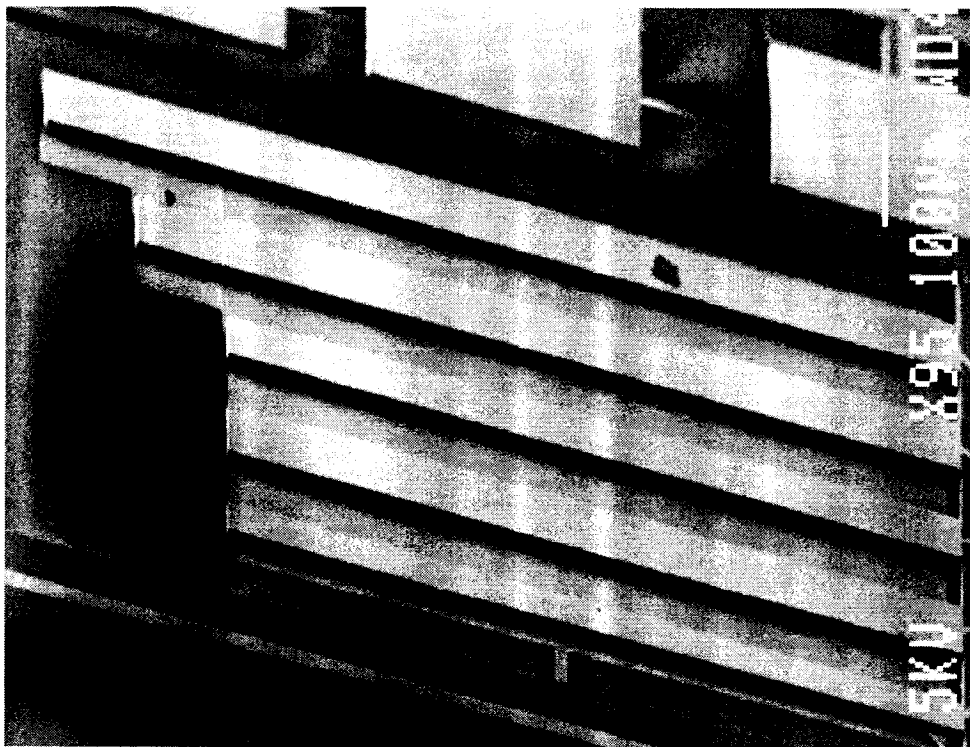
Fig. 3.4 Cantilever beams with different dimensions

49
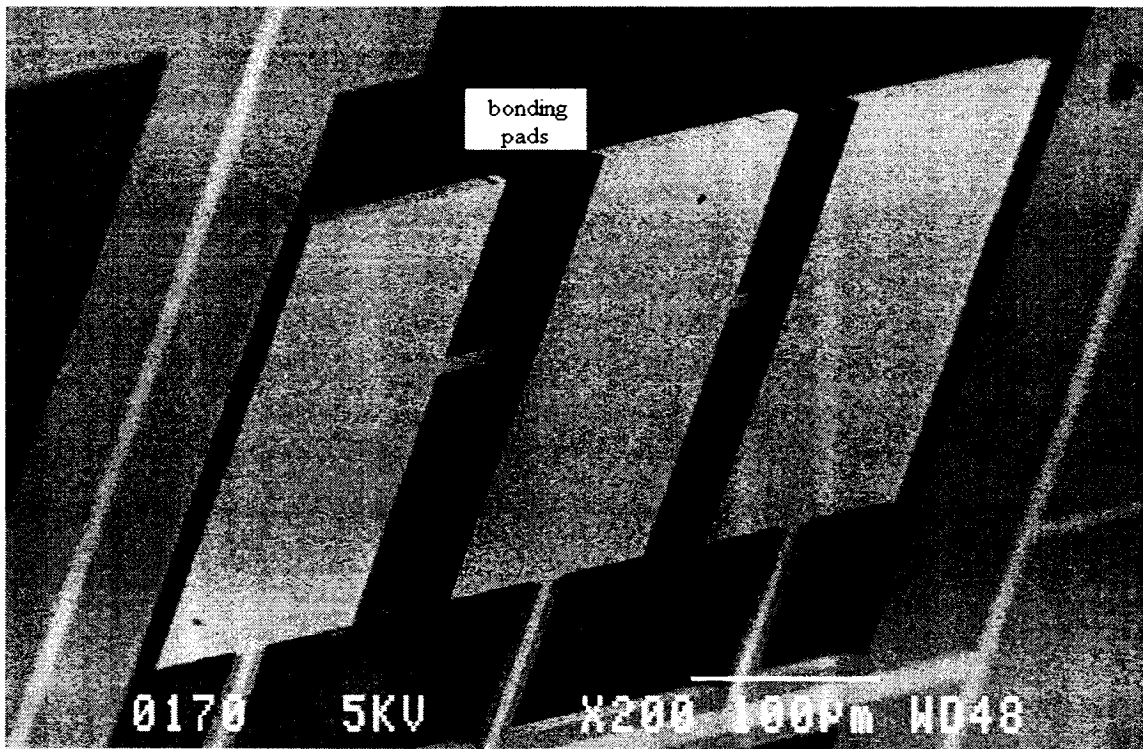
Fig. 3.5 Clear view of the ends of the microplates
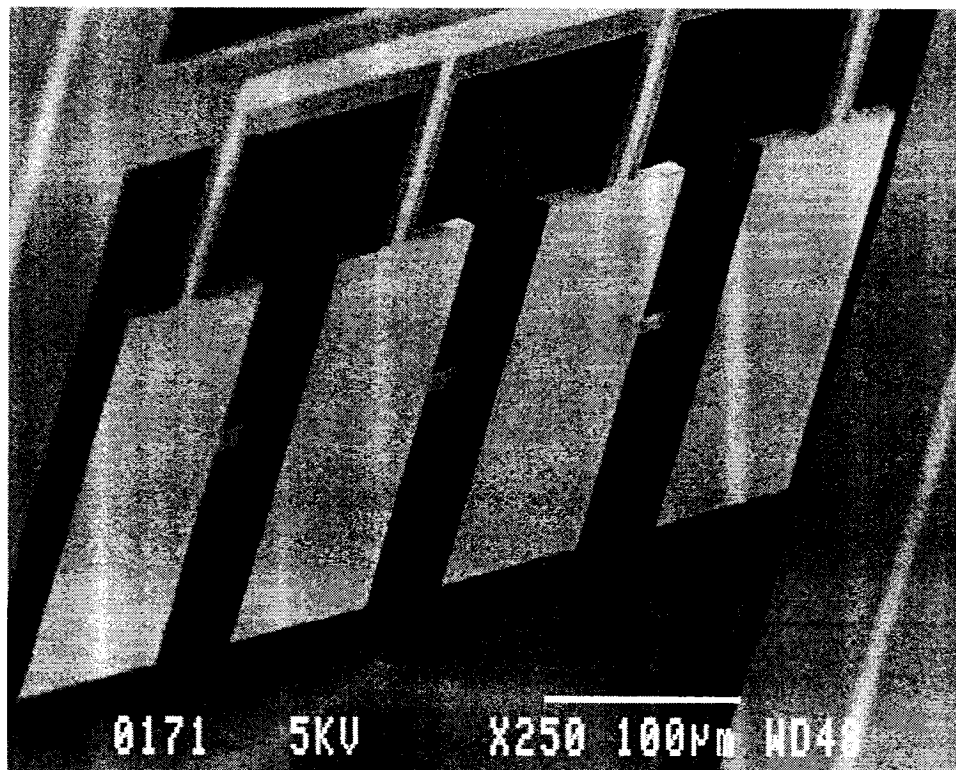
Fig. 3.6 Microplate at the extreme left having three free edges (cantilever type)
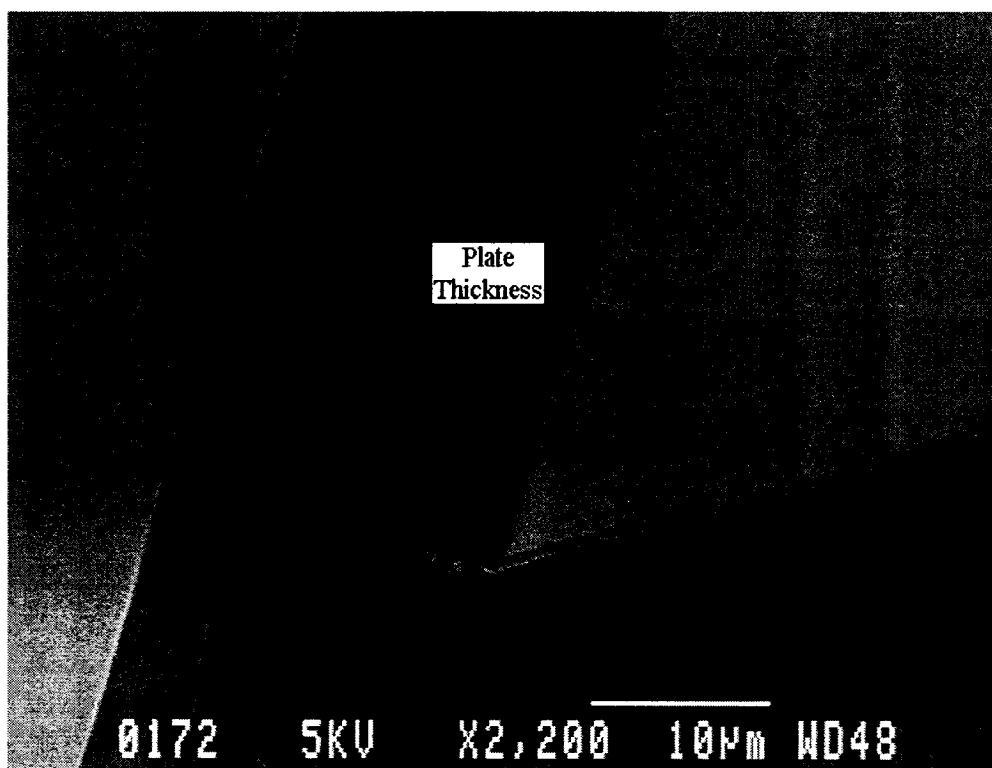
Fig. 3.7 Extreme close view of the microplate, showing the thickness
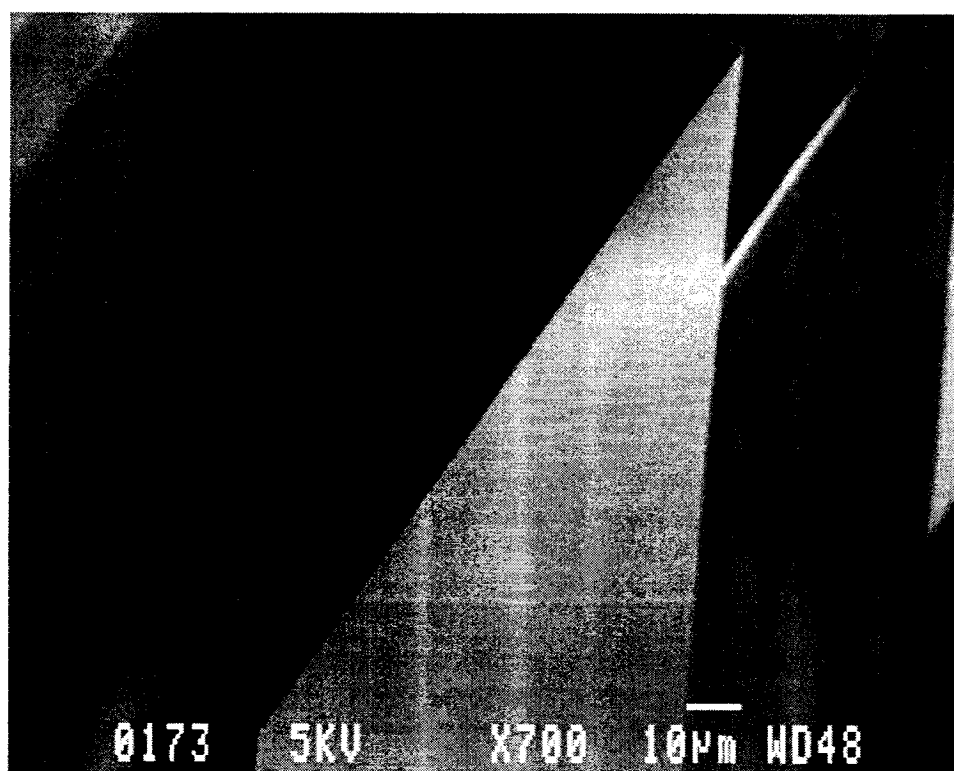
Fig. 3.8 Side view showing the gap between the two electrodes

51

3.4 Conversion of a Cantilever System to a Lumped Model

An electrostatically actuated micro cantilever beam is a continuous system, and it would be more complicated to carry out the nonlinear analysis and solve for its velocity, phase portrait and its pull-in phenomenon directly. In this section, the distributed system is converted into an equivalent mass -spring model, thereby enabling the study of non-linear behaviour of the system without complexity.
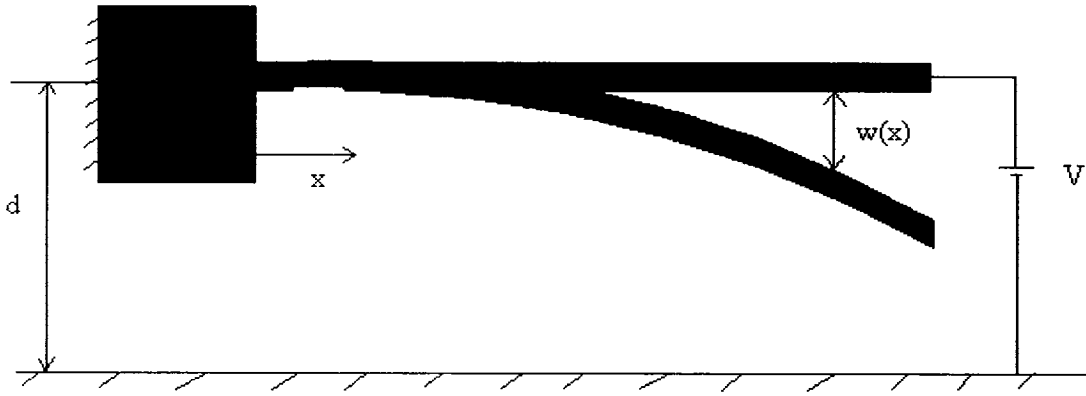
Fig. 3.9 A cantilever beam model under an electrostatic force

The deflection shape of the beam. shown in Figure 3.9, is assumed as given in the Equation 3.1 which satisfies the boundary conditions of the cantilever beam.

$$w(x) = a(6x^2 - 4x^3 + x^4)$$ (3.1)

Let the polynomial be taken as $\phi(x)$ in the above Equation and it is written as

$$w(x) = a.\phi(x)$$ (3.2)

where a is an arbitrary constant. Further, the second derivative of the above equation leads to

$$w''(x) = 12a(1 - 2x + x^2)$$ (3.3)

or

$$w''(x) = a.\phi''(x)$$ (3.4)

The potential energy of the beam is given by

$$U_b = \frac{1}{2} EI \int_0^l (w''(x))^2 \, dx$$ (3.5)

The above equation is reduced to the form

$$U_b = C_1.a^2$$ (3.6)

where

$$C_1 = \frac{1}{2} EI \int_0^l (\phi''(x))^2 \, dx$$ (3.7)

The kinetic energy of the beam is given by

$$T_b = \frac{1}{2} \rho A \omega^2 \int_0^l (w(x))^2 \, dx$$ (3.8)

Similar to the Equation 3.6, kinetic energy also can be reduced to

$$T_b = C_2 \omega^2 a^2$$ (3.9)

where

$$C_2 = \frac{1}{2} \rho A \int_0^l (\phi(x))^2 \, dx$$ (3.10)

The corresponding equations for an equivalent mass-spring system are given below. The equivalent potential energy for a rigid plate would be

$$U_{rig} = \frac{1}{2} K_{eq} \langle w^2 \rangle$$ (3.11)

Where K_{eq} is the equivalent stiffness of the lumped system.

53

$$\langle w^2 \rangle = \frac{1}{l} \int_0^l w^2(x) dx$$

(3.12)

is the mean square value of the deflection. Hence, Equation 3.11 can be written in the form

$$U_{rig} = C_3 K_{eq} a^2$$

(3.13)

where

$$C_3 = \frac{1}{2} \int_0^l (\phi(x))^2 dx$$

(3.14)

The equivalent kinetic energy of the system would be

$$T_{rig} = \frac{1}{2} M_{eq} \omega^2 \langle w^2 \rangle$$

(3.15)

where M_{eq} is the equivalent mass of the lumped system. The above equation reduces to

$$T_{rig} = C_4 M_{eq} \omega^2 a^2$$

(3.16)

and

$$C_4 = \frac{1}{2} \int_0^l (\phi(x))^2 dx$$

(3.17)

From Equations 3.6, 3.9, 3.13 and 3.16, the equivalent stiffness and mass are obtained as

$$K_{eq} = \frac{C_1}{C_3}$$

(3.18)

$$M_{eq} = \frac{C_2}{C_4}$$

(3.19)

Hence, the mechanical part of a continuous system is converted into an equivalent lumped system and their stiffness and mass values are derived.

Similar to the mechanical conversion, the equivalent electrostatic system can be obtained as shown below. The electrostatic potential energy for a given voltage of V_i is written as

$$U_{el.he_i} = \frac{1}{2}\varepsilon_0\varepsilon_r bV_i^2 \int_0^l \frac{dx}{(d - w_{st_i}(x))} \qquad (3.20)$$

where 'i' represents a particular voltage V_i. Also, $w_{st_i}(x) = a_{st_i}\phi(x)$ is the corresponding static deflection and a_{st_i} is obtained from the force balance plot for that voltage V_i. Hence, Equation 3.20 is numerically integrated which results in a constant value such that

$$U_{el.he_i} = C_{5_i} \qquad (3.21)$$

The equivalent electrostatic potential energy for a lumped system can now be expressed as

$$U_{el.rig_i} = \frac{\varepsilon_0\varepsilon_r A_{eq_i} V_i^2}{2(d - w_{av.st_i}(x))} \qquad (3.22)$$

Here, it should be noted that the equivalent area of the rigid plate changes when the voltage changes due to the electrostatic nature and hence the term A_{eq_i}. Similar to the mechanical part, there is an average deflection which is a constant value for a given voltage.

$$w_{av.st_i} = \frac{1}{l}\int_0^l w_{st_i}(x)dx \qquad (3.23)$$

The potential energy in Equation 3.22 thus reduces to

$$U_{el.rig_i} = C_{6_i} A_{eq_i} \qquad (3.24)$$

where

$$C_{6_i} = \frac{\varepsilon_0\varepsilon_r V_i^2}{2(d - w_{av.st_i}(x))} \qquad (3.25)$$

Hence, the equivalent area for the lumped system is obtained from Equations 21 and 24

as

$$A_{eq_i} = \frac{C_{5_i}}{C_{6_i}}$$ (3.26)

Thus the cantilever system is converted into an equivalent lumped mass-spring model

with K_{eq}, M_{eq} and A_{eq_i} as shown in Figure 3.10 based on balancing the energy equations as

derived.
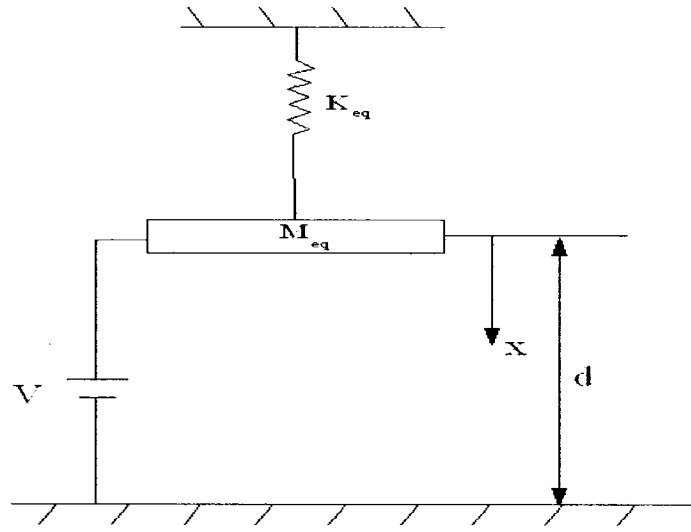
Fig. 3.10 Equivalent mass-spring model

The equivalent stiffness (K_{eq}), equivalent mass (M_{eq}) and equivalent electrostatic area

A_{eq_i} are calculated and given below for the cantilever [70] whose dimensions and

properties that are used are given in Table 3.1.

Table 3.1 Design parameters of the cantilever beam [70]

E (kg/m^2)	ρ(kg/m^3)	l(mm)	b(mm)	t(μm)	d(μm)	ε_0(F/m)
155.8x10^9	2.33x10^3	20	5	57	92	8.85x10^{-12}

The values obtained from the analysis are

Equivalent Stiffness, K_{eq} = 18.623 N/m

Equivalent Mass, M_{eq} = 1.3281 x 10^{-5}kg

Since the electrostatic area (A_{eq_i}) varies with the voltage (V_i), it is given below in Table 3.2 for some particular values of the voltage. It could be seen that the equivalent area is the same as the actual cantilever area which is 100 x 10^{-6} m^2 when there is no voltage applied.

Table 3.2 Equivalent electrostatic area variation with the voltage

Voltage V_i (Volts)	Equivalent Area A_{eq_i} x 10^{-6} m^2
0	100.0000
10	100.0020
20	100.0026
30	100.0204
40	100.0748
50	100.2273
60	100.7142
68.4	104.8800

When the voltage increases, the equivalent electrostatic area slowly increases and when it is around the pull-in voltage, the equivalent area increases rapidly. The Table 3.2 values

57

are plotted below in Figure 3.11 to see the rapid variation of the electrostatic area near the pull-in voltage.
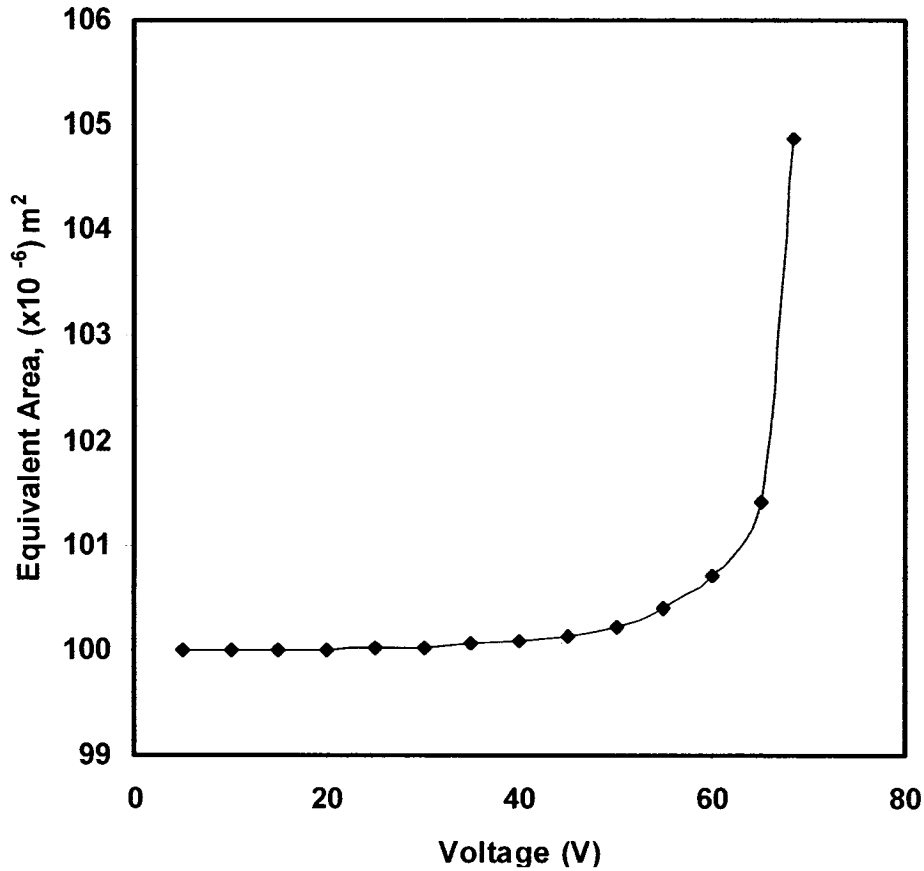
Fig. 3.11 Variation of the equivalent area with the voltage

In the above mentioned equivalent electrostatic model for the beam, the electrostatic area varies with the varying voltage while the gap between the top and bottom electrodes is kept constant throughout. Another way of designing the equivalent system is by changing the gap between the electrodes over a changing voltage while keeping the electrostatic area constant. Thus, the cantilever system is effectively converted into a lumped mass-

spring model with its equivalent values to study the nonlinear static and dynamic behaviour.

3.5 Summary

The method of microfabricating the MEMS structures based on the MicraGeM technology has been explained in this chapter. The fabricated devices were shown from the Scanning Electron Microscopy (SEM) pictures taken. In the second part of the chapter, the conversion of a cantilever system into an equivalent lumped mass-spring model was done successfully and the final equations for calculating the equivalent mass, stiffness and electrostatic area have been derived.

Chapter 4

Nonlinear Analysis of MEMS

Structures

4.1 Introduction

For small oscillations the response of a deformable structure can be adequately described by solving linear equations together with appropriate boundary conditions, but as the amplitude of the oscillations increases, the nonlinear effects grow and it is important to consider them in the analysis. The sources of nonlinearities can be geometric, inertial, phenomenological or material in nature. Geometric nonlinearities may be due to the mid-plane stretching of the structure. Nonlinear inertial effects are caused by the presence of concentrated or distributed masses. Material nonlinearities occur whenever the stress is a nonlinear function of the strain [71]. Examples for phenomenological nonlinearity include the systems behaving nonlinearly, such as, simple pendulum executing large oscillations, a particle restrained by a nonlinear spring, a particle in a central-force field etc. The electrostatic actuation in MEMS structures is a nonlinear phenomenon and an introduction has been given in the previous chapters about its nonlinearity. In this chapter, the nonlinear analysis is done on some of the electrostatically actuated structures by solving the differential equation of the system. A brief introduction and an analysis are

given for the case of a simple pendulum in the beginning and then the nonlinear analysis for the electrostatic MEMS structures is done and its similarity with the pendulum is observed. For both these cases, phase portraits are sketched and the behaviour of the system is studied. The differential equation of motion is integrated and reduced to a form suitable to find out the time period and hence the nonlinear frequency of vibration for the electrostatic structures.

4.2 Simple Pendulum: Phase portrait

A simple pendulum consists of a particle mass swinging in one plane at the end of a light string or rod. An ideal pendulum does not exist but a ball of lead with a diameter of about half an inch swinging at the end of a light string about a yard long may be considered as a close example. The Figure 4.1 shows such an example of a simple pendulum. When the string makes an angle 'θ' with the vertical, the equation of motion of the pendulum as shown in Figure 4.1 can be written as

$$I\ddot{\theta} + mgL_s \sin\theta = 0 \qquad (4.1)$$

where 'm' is the mass of the bob attached to the string, 'L_s' is the string length and 'g' is the acceleration due to gravity. The Equation 4.1 can be rewritten as

$$\ddot{\theta} + \omega_0{}^2 \sin\theta = 0 \qquad (4.2)$$

where

$$\omega_0{}^2 = \frac{g}{L_s} \qquad (4.3)$$

$$\text{or } \omega_0 = \sqrt{\frac{g}{L_s}} \qquad (4.3a)$$
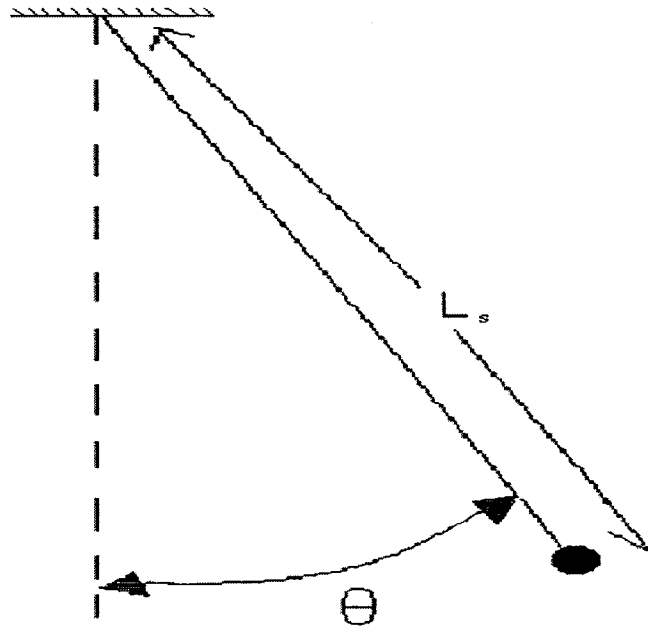
Fig. 4.1 A simple pendulum

The dynamic analysis of the pendulum based on the Equation 4.2 can be done in two ways depending on the amplitude of oscillation. If the system undergoes small oscillations, it can be considered to be linear and the Equation 4.2 reduces to

$$\ddot{\theta} = -\omega_0^2 \theta \qquad (4.4)$$

since for smaller deflections, $\sin \theta \approx \theta$. The solution of the above equation can be given as

$$\theta = \theta_{max} \sin \omega_0 t \qquad (4.5)$$

where θ_{max} is the maximum amplitude of oscillation.

Thus the linear analysis of the pendulum is simple and approximations are acceptable for small oscillations. The analysis of the pendulum becomes more interesting and complex when the oscillations are no longer considered to be small and the Equation 4.2 cannot be

reduced to a simple form. Different methods have been used so far to analyse such a case of nonlinearity and some of them are listed below.

i) Exact method (time integral method using the elliptic integral approach)

ii) Perturbation method

iii) Harmonic balance method (Fourier analysis)

iv) Phase portrait technique

In the time integral method, the equation of motion is numerically integrated and solved for the response till a steady state is reached. Elliptic integral of the first kind is used in the case of a pendulum while using this method and the time period of oscillation is evaluated. Fulcher et al. [72] analysed the nonlinear pendulum both experimentally and theoretically and compared their results. Both the exact method and perturbation methods were used to solve for the solution theoretically. Perturbation methods are commonly used if the nonlinearities of the dynamic system are of a small order. The nonlinear terms are referred to as "perturbations" and are identified by means of a small parameter. The solution is obtained in the form of a power series in this parameter. For example, time period is calculated using the perturbation theory method given by Kryloff [73] and these values were compared with the experimental time period and found to be in agreement for the same case of a simple pendulum. The harmonic balance method is a simple, systematic approach and is not restricted to weakly nonlinear problems. The technique is based on a Fourier series residual approximation of the nonlinear terms, converting the nonlinear differential equations of motion into nonlinear algebraic equations. Simon et al. [74] solved for the time period using the above mentioned Fourier series analysis. For

larger amplitudes, Fourier coefficients of the terms higher than fifth order do not have significant impact on the solution such as the time period of oscillation.

Even though the phase portrait analysis cannot be considered as a method to solve for the time period and for the response of the system, it can be used to study the motion and its behaviour in the nonlinear range. The phase portrait for the motion of a simple pendulum is done by integrating the equation of motion to obtain the velocity and by plotting this velocity against a range of displacement or amplitude of oscillation. Different values of initial amplitudes are taken and hence the different plots of velocity against the displacement are obtained. Thus the solution for such a motion of the pendulum is given below. The equation of motion from Equation 4.2 is

$$\ddot{\theta} + \omega_0{}^2 \sin\theta = 0 \tag{4.6}$$

This equation is multiplied throughout by $2.\dfrac{d\theta}{dt}$ to get

$$2.\frac{d\theta}{dt}.\frac{d}{dt}(\frac{d\theta}{dt}) + 2.\frac{d\theta}{dt}.\omega_0{}^2.\sin\theta = 0 \tag{4.7}$$

Integration of the above equation leads to

$$\left(\frac{d\theta}{dt}\right)^2 = 2.\omega_0{}^2.\cos\theta + C \tag{4.8}$$

where C is the constant of integration. To find the value of C, the assumed initial conditions are

$\theta = \alpha_i$ and $\dfrac{d\theta}{dt} = 0$. Hence, the value of 'C' is obtained as

$$C = -2.\omega_0{}^2.\cos\alpha_i \tag{4.9}$$

where ' α ' is the initial amplitude of oscillation. Hence the velocity equation is

$$\left(\frac{d\theta}{dt}\right) = \omega_0\sqrt{2.(\cos\theta - \cos\alpha_i)} \tag{4.10}$$

When the velocity $\left(\dfrac{d\theta}{dt}\right)$ is plotted for various values of displacement (θ), the plot

obtained is termed as the phase portrait of the system. Such a portrait is given below for

the following values:

Initial displacement, α_i varying from $\dfrac{\pi}{16}$ to π radians

Acceleration due to gravity, $g = 9.81\, m/s^2$
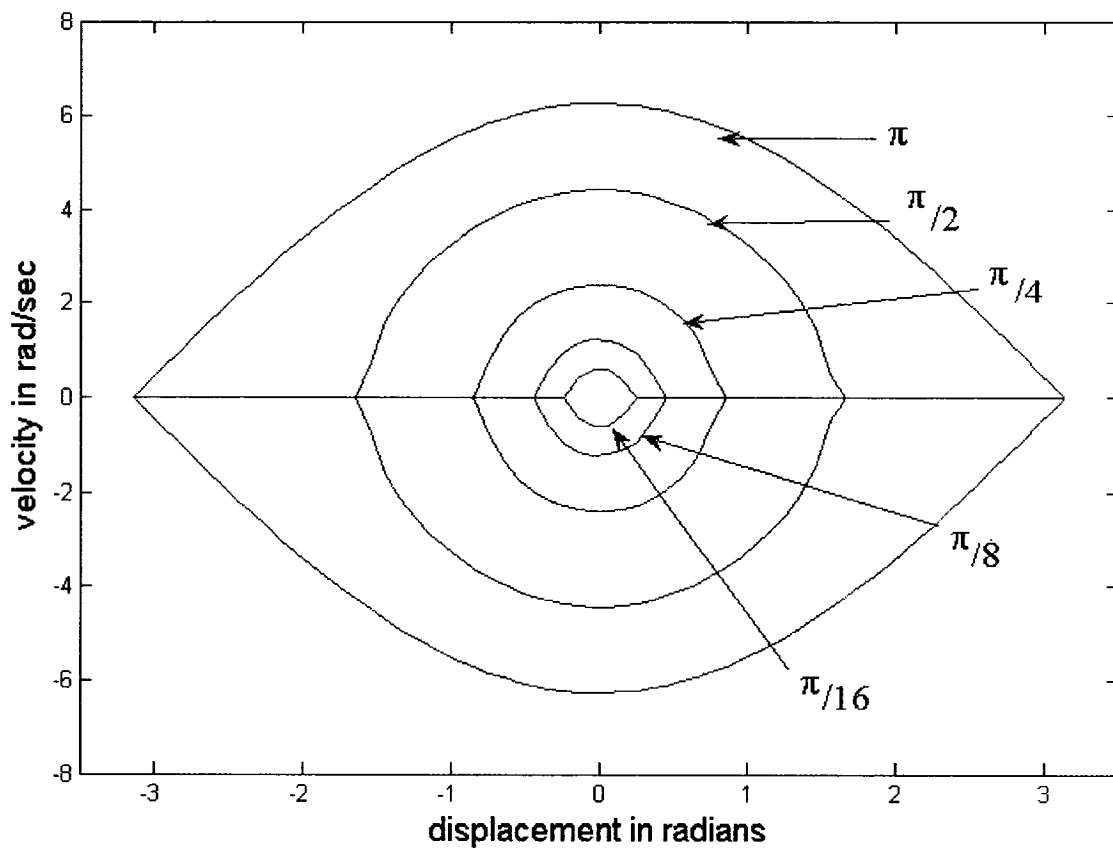
Length of the string, $\qquad$ $L_s = 1m$

Fig. 4.2 Phase portrait of a simple pendulum

The phase plot is done by plotting velocity ($\frac{d\theta}{dt}$) for the values of displacement (θ)

ranging from π to $-\pi$ radians which is shown in Figure 4.2. It can be seen that for

smaller values of initial amplitude (α_i) like $\frac{\pi}{16}$ or even $\frac{\pi}{8}$ radians, the phase plot takes

the shape of a circle which means that the system is behaving linearly. But for higher

values of initial amplitudes, the circular shape transforms into the shape of an ellipse or

oval. This is due to the nonlinear behaviour of the system when it undergoes larger

deformations or oscillations as explained previously. For higher values of initial

amplitudes, like more than π radians, the velocity of the pendulum becomes a complex

value and when are plotted over a range of displacements, it forms a separatrix and the

velocity does not become zero at any point of time. When initial amplitude is larger than

π radians, the pendulum will start oscillations from the opposite field, and hence the

physical interpretation of the phase portraits is not obvious. These are termed as the

chaotic behaviour or simply chaos of the pendulum and they can be seen in other physical

systems also. An example of a similar behaviour [75] is shown in Figure 4.3.
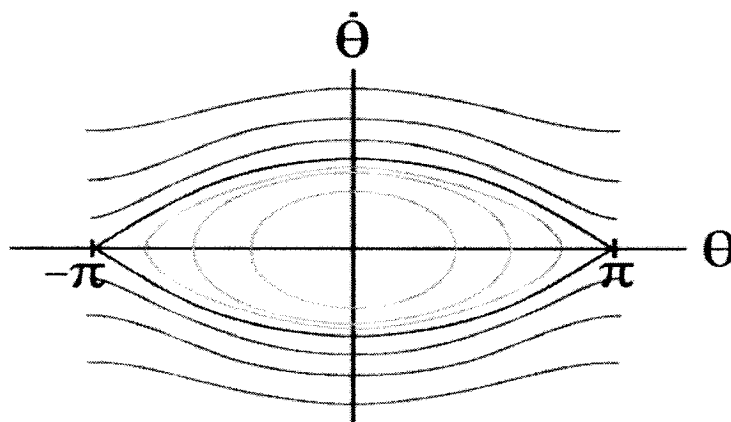

Fig. 4.3 Example for the chaotic pendulum phase portrait [75]

The nonlinear behaviour of the simple pendulum is thus studied and the various methods used to solve either exactly or approximately for the solution were discussed. Also, the phase portrait equations were derived and plotted for different initial angles or displacements. Now, the nonlinear behaviour of the electrostatic actuation in the case of MEMS structures will be analysed and the same approach as that of the pendulum will be implemented which can be seen in the subsequent sections.

4.3 Nonlinear Phenomena in Electrostatic MEMS

The electrostatic actuation in MEMS structures as discussed earlier is a nonlinear phenomenon and to obtain the exact solution is difficult. Hence, we employed the Taylor's series expansion on the electrostatic force and the system becomes linear which is easier to solve. This linear analysis was explained previously in Chapter 2. But this approximation holds well only when the deflection or the amplitude of vibration is small. For cases when the gap between the top and bottom electrodes becomes significantly large, the amplitude of vibration or the deflection also becomes large and the nonlinear effect is more dominant and it has to be considered for the stable operation of the device. In this section, both static and dynamic analysis, which is the pull-in voltage determination and the frequency determination respectively, are done for electrostatically actuated structures namely rigid micro plates and micro cantilevers. The analysis is done for three different cases and the various results obtained are discussed below in the subsequent sections.

The three cases that are analysed are:

(i) A simple mass-spring model where the basic phenomenon of phase portraits is explained to understand the nonlinear behaviour of the system. This also forms the base for the analysis of cantilever systems.

(ii) An equivalent mass-spring model of the cantilever system [70] based on the nonlinear analysis using the phase portraits and time integration methods. The results obtained are then compared with that of [70].

(iii) An equivalent mass-spring model of the cantilever system fabricated using the Micragem technology, whose design and fabrication methodologies were explained in Chapter-3.

4.3.1 A simple mass spring model: phase portrait analysis

A simple mass-spring model, as shown in Figure 2.1 with design parameters as given in the Table 2.1, is considered from chapter 2. A linear analysis has been done in Chapter 2 for this system and the pull-in voltage has been determined based on the approximation. But in this section, nonlinearity in the system is studied by doing the phase portrait analysis and the determination of pull-in voltage is carried out. The static and dynamic analysis of the mass-spring model is done based on the phase portraits in this section. The equation of motion 2.2 is reduced to a form of velocity equation to plot the phase portraits and is given below. The Equation 2.2 is multiplied throughout by $2.\dfrac{dx}{dt}$ and is rewritten as

$$m.2.\frac{dx}{dt}.\frac{d}{dt}(\frac{dx}{dt}) + k.2.\frac{dx}{dt}.x = 2.\frac{dx}{dt}.\frac{\varepsilon_0\varepsilon_r AV^2}{2(d-x)^2}$$

This equation is integrated throughout with respect to time and is reduced to the form

$$m\dot{x}^2 + kx^2 - \frac{\varepsilon_0\varepsilon_r AV^2}{d-x} = E_0$$

In the Equation 4.12, E_0 is the constant obtained from integration and this constant is called as the conservative energy value available for the system. Based on this energy value, the static and dynamic behaviour of the system varies which will be seen later in the subsequent sections. Hence from the Equation 4.12, the velocity of the system is obtained as

$$\dot{x} = \pm\sqrt{\frac{E_0 + \left(\frac{\varepsilon_0\varepsilon_r AV^2}{d-x}\right) - kx^2}{m}}$$

The phase portrait is obtained by plotting the velocity against the displacement from the Equation 4.13. This can be done in two ways:

(i) Varying the value of the conservative energy level (E_0), for a particular value of voltage V.

(ii) Varying the voltage with a constant value of E_0.

4.3.1.1 Phase portrait for constant voltage and varying energy

The phase plots for the mass-spring system considered are given in this section. In the Figure 4.4, there is no voltage applied (V=0) to the system but the energy value (E_0) is varied to get different velocity curves. It can be seen from the figure that the phase plots are circular throughout for any value of increasing E_0. This is due to the fact that there is

no nonlinearity in the system since there is no electrostatic force applied on the system (voltage V=0). But when there is a voltage applied on the system, the nonlinearity can be seen clearly as shown in Figure 4.5. The voltage applied is 0.7V which is constant throughout for varying E_0 values. It is seen that as the value of E_0 is increasing, the velocity plot slowly changes from the shape of a circle into an ellipse.
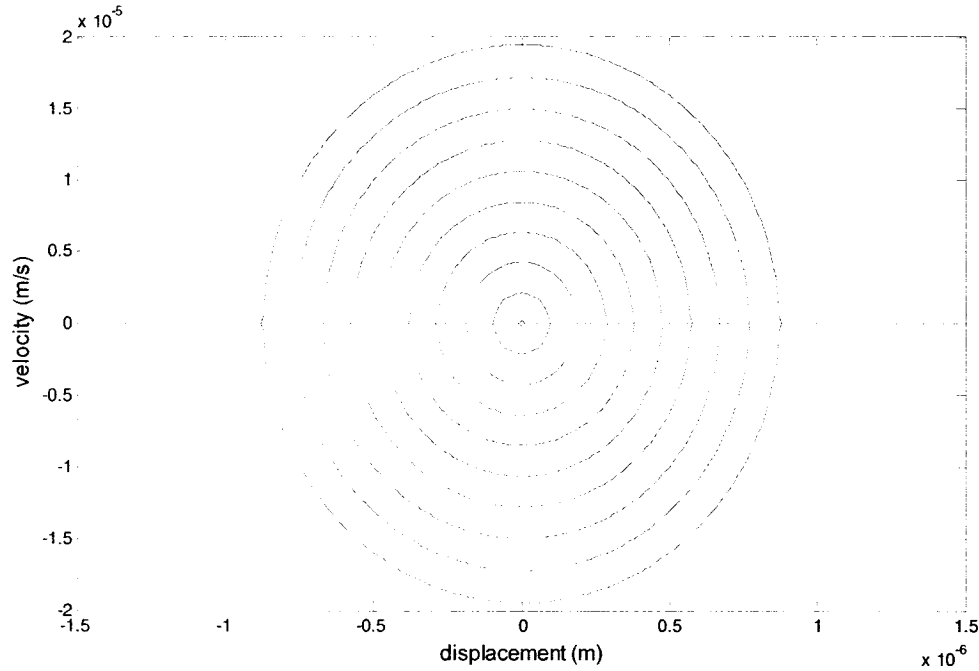

Fig. 4.4 Phase portrait for voltage V=0 and varying Energy value E_0

The points x_1, x_2 and x_3 in Figure 4.5 are the displacement values at which the velocity becomes zero. The first equilibrium position, called the static equilibrium position, is between the points x_1 and x_2 while the second unstable equilibrium position is between x_2 and x_3. As the E_0 value increases, the gap between the points x_1 and x_2 increases and the gap between the points x_2 and x_3 decreases. After a certain E_0 value, the portraits do

70

not cross the x-axis and the velocity increases monotonically as shown in Figure 4.5. This means that the system has become unstable and the failure of the system has occurred for that particular E_0 due to the excessive available energy.
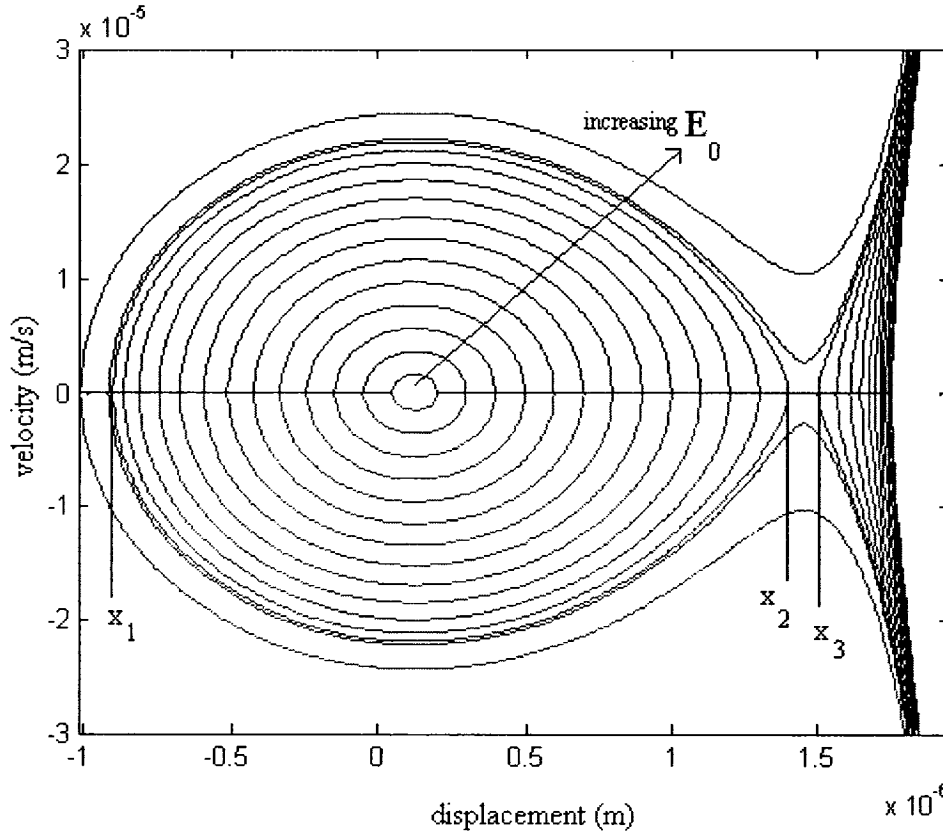

Fig. 4.5 Phase portrait for voltage V = 0.7V and varying energy values E_0

Thus the energy level or range that can be applied to the system, for a particular voltage, has to be known for the safe operation of the system. Beyond a minimum E_0 value, the stable limiting points x_1 and x_2 start separating or the gap between them widens as shown in Figure 4.5. This is termed as minimum conservative energy value, E_1^*, that has to be given to the system for the initiation of its motion. Similarly, there is a particular value of

71

E_0 at which both the unstable limiting points x_2 and x_3 become the same value as shown in Figure 4.5. With any further increase in the E_0 value, the velocity curve separates and grows monotonically. This maximum value of E_0 corresponding to this condition is termed as the maximum conservative energy value, E_2^*, beyond which the system is unstable. Thus the possible range of energy level E_0 (i.e. from E_1^* to E_2^*) which has to be applied for the safe operation of the system can be found out.

4.3.1.2 Phase portrait with constant energy and varying voltage

In the section above, the nonlinear behaviour of the electrostatic MEMS structure with a varying energy level E_0 at a constant voltage has been shown. Similar analysis is done with a varying voltage and at constant energy value in this section. When the E_0 value is kept constant and the voltage is increased, the shape of the velocity plot changes from circle to that of an ellipse. As shown in Figure 4.6, there are three values of displacements at which the velocity becomes zero for a particular voltage. The three displacement values, as explained previously, can be termed as the points x_1, x_2 and x_3. The first equilibrium position, called the static equilibrium position, is between the points x_1 and x_2 while the second unstable equilibrium position is between x_2 and x_3. As we keep E_0 constant in this case, with an increase in the voltage, the gap between the points x_1 and x_2 increases and the gap between the points x_2 and x_3 decreases. After a certain voltage value, the separation of the velocity plot occurs as seen in Figure 4.6. This

means that the system has become unstable and the failure of the system has occurred for
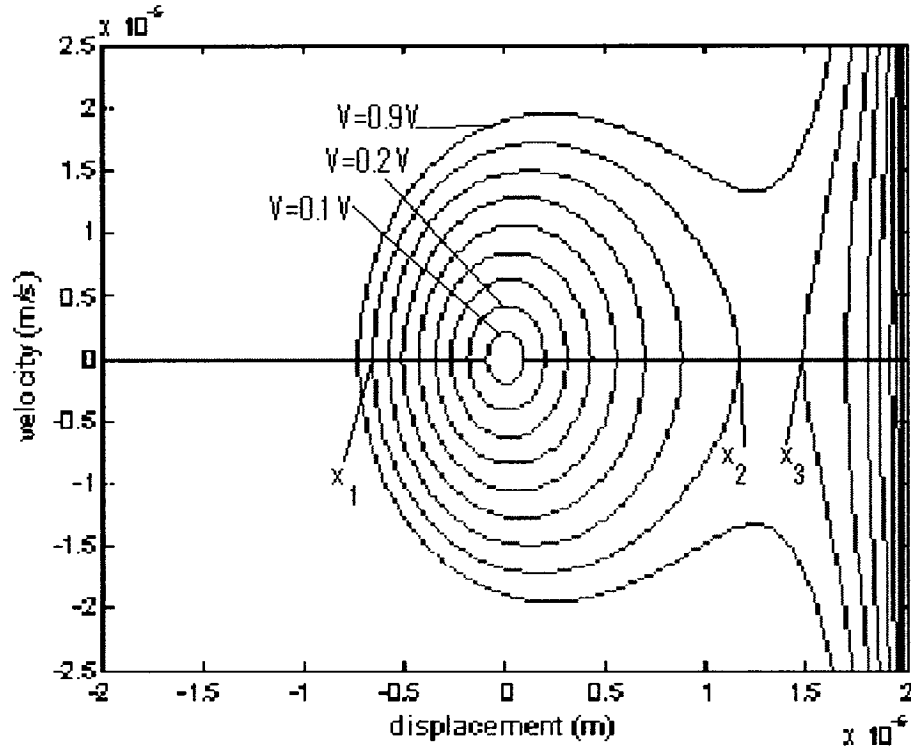
that particular E_0 due to the excessive voltage.

Fig. 4.6 A phase portrait with constant E_0 and varying voltage V

Thus the amount of voltage that can be applied to the system has to be known when a

specific initial conservative energy value E_0 is given to the system. There is a particular

value of voltage at which both the points x_2 and x_3 coalesce. With any further increase in

the voltage, the velocity curve separates and there are no separate x_2 and x_3 points. This

maximum value of voltage is termed as the pull-in voltage for that specific energy value

supplied to the system beyond which the system becomes unstable. Thus an idea of the

maximum amount of voltage application with an initial particular conservative energy value supplied to the system is obtained for the safer operation of the device.

The two sections explained above showed that both the application of voltage and the conservative energy level are interrelated and has its minimum and maximum values. So far in electrostatic MEMS devices, there is only one pull-in voltage value for a particular device. But it is shown here that there can be different pull-in voltages for the same device based on the conservative energy value supplied to the system. It is also shown that the energy value E_0 varies from minimum to maximum based on the voltage applied.

4.3.1.3 Phase portrait for varying voltage and varying energy

Phase portraits are plotted for varying values of voltage and E_0 simultaneously in this section. The minimum and maximum values of E_0 for each voltage is known from the previous section and hence the pull-in voltage of the device is obtained by plotting phase portraits for different voltages at their respective maximum conservative energy value E_2^* as shown in Figure 4.7. It can be seen that for all the voltages there are only two points, x_1 and ' $x_2 - x_3$ ' together, at which velocity is zero since it is plotted for maximum energy levels E_2^* for each voltage and at a particular voltage and its respective E_2^*, all the points x_1, x_2 and x_3 become a single value. This value of the voltage is the pull-in voltage for the device. For the mass-spring system considered here, the pull-in voltage is found to be 1.157V as seen from Figure 4.7. Hence the pull-in voltage determination based on phase

portrait technique is done and this technique can be applied for various electrostatic MEMS structures to find their operating range and the pull-in voltage.
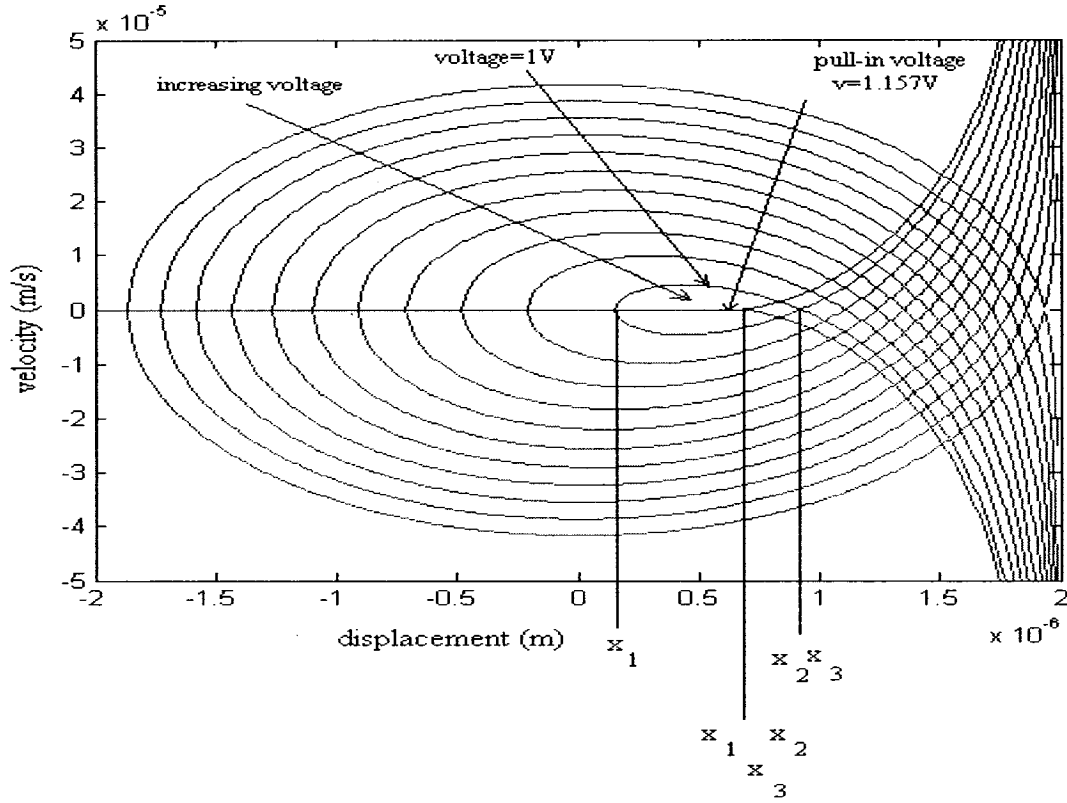

Fig. 4.7 Phase portrait for varying voltages at their respective $E_2{}^*$ values

Thus the basic idea of applying the phase portrait technique to understand the nonlinear influence on the electrostatic MEMS structures has been explained successfully for the simple mass-spring model. The significance of E_0 on the system behaviour is presented and the pull-in voltage determination is done based on phase plots. This method will be studied more extensively for the continuous cantilever system [70] which is converted into a mass-spring model based on Chapter-3, in the subsequent section.

4.3.2 Lumped model of the cantilever

A continuous cantilever system [70] which is converted into a lumped mass-spring model based on the energy equations as shown in the previous chapter is analysed considering the nonlinearity in the system for its static and dynamic behaviour in this section based on the phase portrait and time integration methods. The equivalent stiffness, mass and electrostatic area were found out and given in Chapter 3. The design parameters were also given in previous Chapter in Table 3.1.

The equation of motion of the equivalent system under an electrostatic force can be written as

$$M_{eq}\ddot{x} + K_{eq}x = \frac{\varepsilon_0\varepsilon_r A_{eq_i} V_i^2}{2(d-x)^2} \tag{4.14}$$

For the static equilibrium, the electrostatic force is balanced by the mechanical restoring force as explained before. Hence the above equation reduces to

$$K_{eq}x = \frac{\varepsilon_0\varepsilon_r A_{eq_i} V_i^2}{2(d-x)^2} \tag{4.15}$$

Thus the force balance is plotted for different values of voltage which is shown in Figure 4.8. From the force balance, it can be seen that for a particular voltage, both the stable and unstable equilibrium positions, x_s and x_p, become a single point which is the pull-in voltage of the device as explained before. This force balance plot will be used later in finding out the energy levels E_1^* and E_2^* for any value of the voltage.
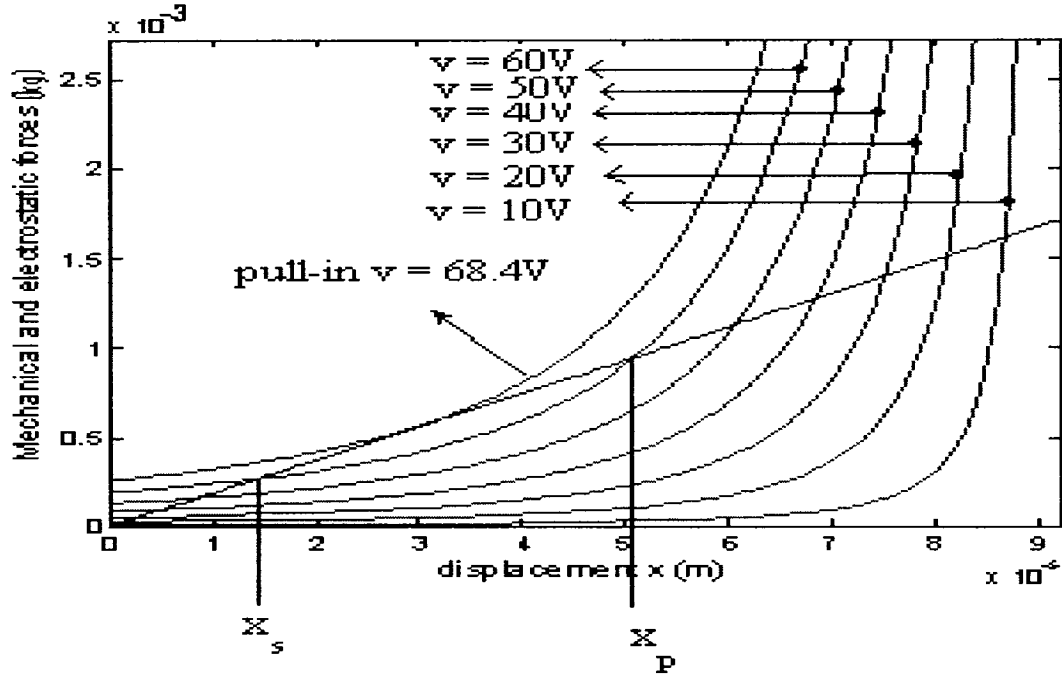
76

Fig. 4.8 Force balance plot for the equivalent mass-spring system

4.3.2.1 Phase portrait analysis

Similar to the sections explained before, the phase portraits are plotted to study the nonlinear behaviour of the cantilever system considered here. The equation of motion is reduced to the form similar to Equation 4.12 as

$$M_{eq}\dot{x}^2 + K_{eq}x^2 - \frac{\varepsilon_0\varepsilon_r A_{eq_i}V_i^2}{d-x} = E_0 \tag{4.16}$$

The above equation is reduced into the form of a velocity Equation 4.17 which is used to plot the phase portraits and it is given as

$$\dot{x} = \pm\sqrt{\frac{E_0 + \left(\dfrac{\varepsilon_0\varepsilon_r A_{eq_i}V_i^2}{d-x}\right) - K_{eq}x^2}{M_{eq}}} \tag{4.17}$$

where 'i' varies from 1 to p and V_p being the pull-in voltage for the device.

77

The two parameters that can be varied in the Equation 4.17 are the conservative energy value E_0 and the voltage V. The variation in the phase portrait due to these two parameters is shown in the sections below and their significance in affecting the behaviour of the system is emphasized. The phase portraits are plotted as shown in Figure 4.9 for a constant energy value E_0=0 and varying voltages. As explained in previous section, when the value of the voltage increases, the gap between the points x_1 and x_2 increases while the gap between x_2 and x_3 decreases. At a particular value of the voltage, 49.2V in this case, the points x_2 and x_3 coalesce. This is the maximum voltage that can be applied to the system when the initial energy value E_0 supplied is zero beyond which the system becomes unstable. Hence the separation of the velocity plot occurs which is seen for 60V in Figure 4.9.

Different cases of phase portraits can be drawn by keeping energy values E_0 as a constant and by varying the voltages for each case. Hence the maximum voltage that can be applied to the system for a particular value of E_0 is found out. Similarly, different cases of phase plots are obtained by keeping a constant voltage and varying the energy values E_0 for each case. In this case, the minimum and maximum energy values, E_1^* and E_2^*, that can be given to the system for that particular voltage are found out. The significance of conservative energy value E_0 and the determination of pull-in voltage by means of the phase plot are discussed below in the next sections.
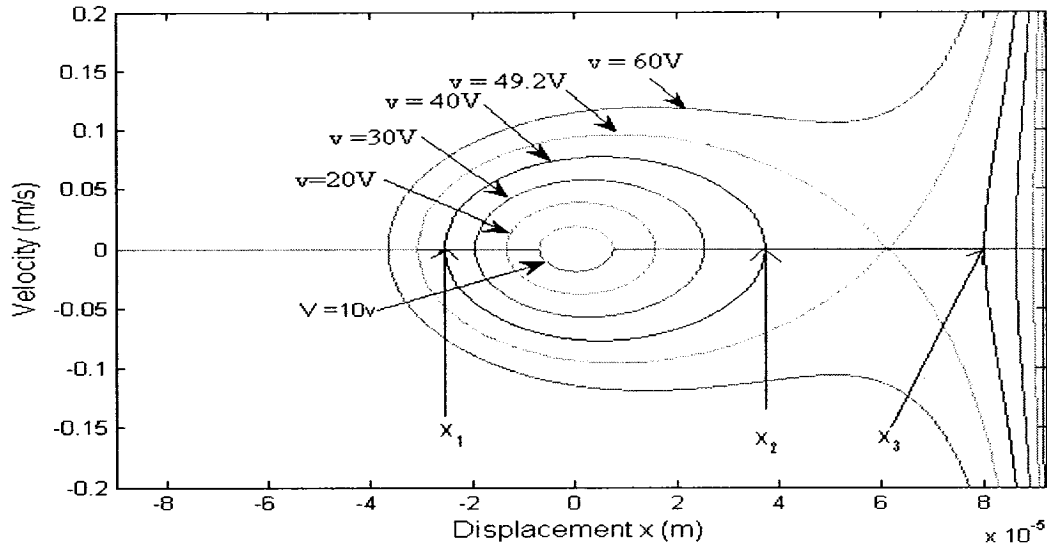
78

Fig. 4.9 Phase portrait for $E_0 = 0$ and varying voltages

4.3.2.2 Significance of E_0

Varying the energy value E_0 can clearly affect the value of voltage that can be applied to the system as was seen previously from different phase plots. Hence there is a need to know the range of values of E_0 to be applied before applying the voltage and vice-versa.

It is always difficult and time consuming to know the E_1^* and E_2^* for each voltage if we follow the hit and trial method. Hence an easier way of knowing these values is done by means of using the force balance plot. From the force balance plot as shown in the Figure 4.8, there are two equilibrium points, x_s and x_p, for every voltage, except the pull-in voltage. Hence an idea of the numerical values of E_1^* and E_2^* can be obtained by substituting x_s and x_p instead of x in the velocity Equation 4.17 and putting the velocity as zero.

Thus E_1^* and E_2^* can be expressed as shown in the Equations 4.18 and 4.19.

$$E_1^* = K_{eq}x_s^2 - \frac{\varepsilon_0\varepsilon_r A_{eq_i}V_i^2}{(d - x_s)}$$ (4.18)

$$E_2^* = K_{eq}x_p^2 - \frac{\varepsilon_0\varepsilon_r A_{eq_i}V_i^2}{(d - x_p)}$$ (4.19)
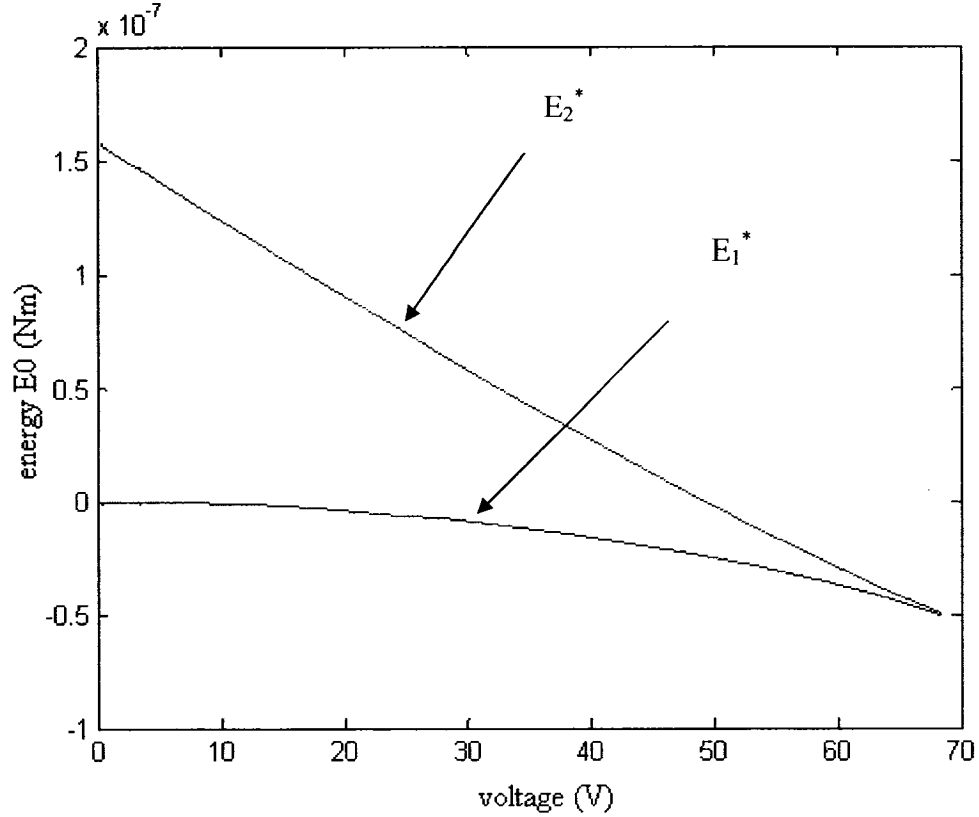

Fig. 4.10 Variation of voltage against the energy value

Thus the values of E_1^* and E_2^* can be plotted with varying voltages and is shown in Figure 4.10. It can be seen from the figure that the gap between the two energy values, E_1^* and E_2^*, reduces as the value of the voltage increases. Hence the range of the conservative energy value that can be applied to the system is reduced as the voltage increases. This can be clearly seen in Figure 4.11 which is plotted between the voltage

80

and the difference between corresponding E_2^* and E_1^* (ΔE) with E_1^* being taken as the

absolute value (i.e. y-axis starts from E_1^*). As the voltage is increased, the value of ΔE

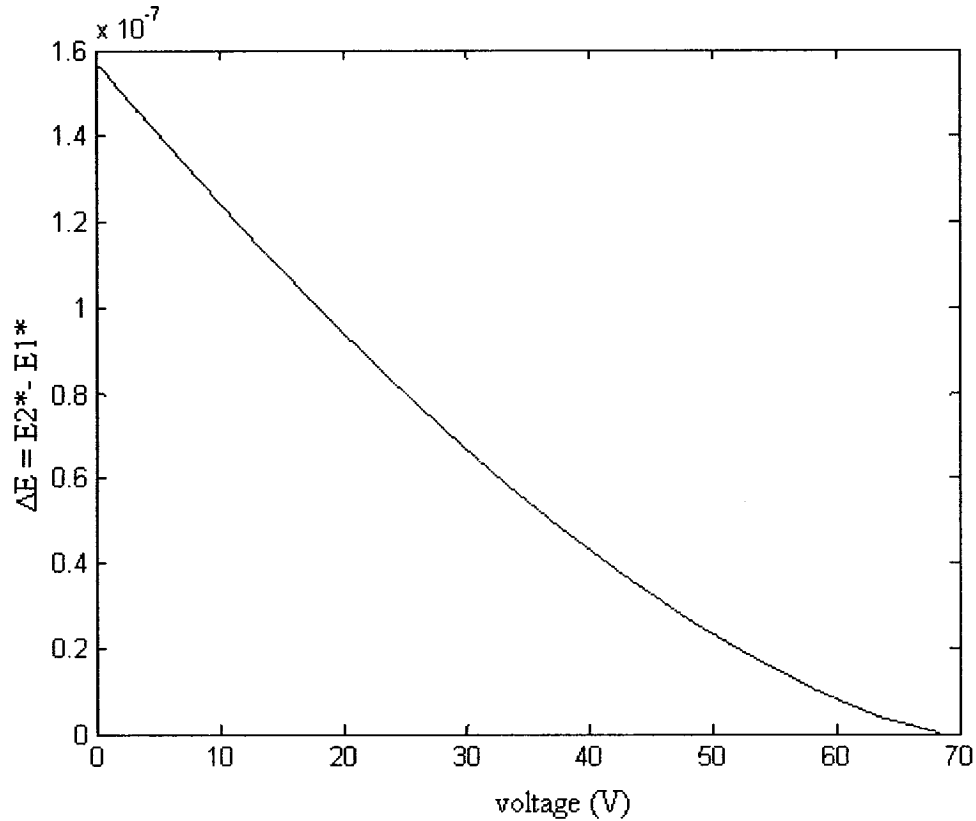decreases and it becomes zero at the pull-in value.

Fig. 4.11 Variation of voltage against ΔE

It is known that the range of energy value E_0 that can be applied to the system for any

voltage varies from E_1^* to E_2^* and there are three points x_1, x_2 and x_3 at which the

velocity becomes zero at any E_0 other than E_1^* and E_2^* which is clearly shown in Figure

4.9. At any particular value of voltage, the points x_1 and x_2 start separating from each

other at E_1^* and the points x_2 and x_3 coalesce at E_2^*. The path traced by these three points

for a range of E_0 at a particular voltage is sketched below in Figure 4.12 and their

direction of travel is shown by the arrows. It is also seen that the range of E_0 reduces as

the voltage increases as explained previously from Figures 4.10 and 4.11. At voltages

very close to the pull-in, the gap between the points reduces similar to the range of E_0

applied. At the pull-in voltage, all the three points meet at one for only one value of E_0
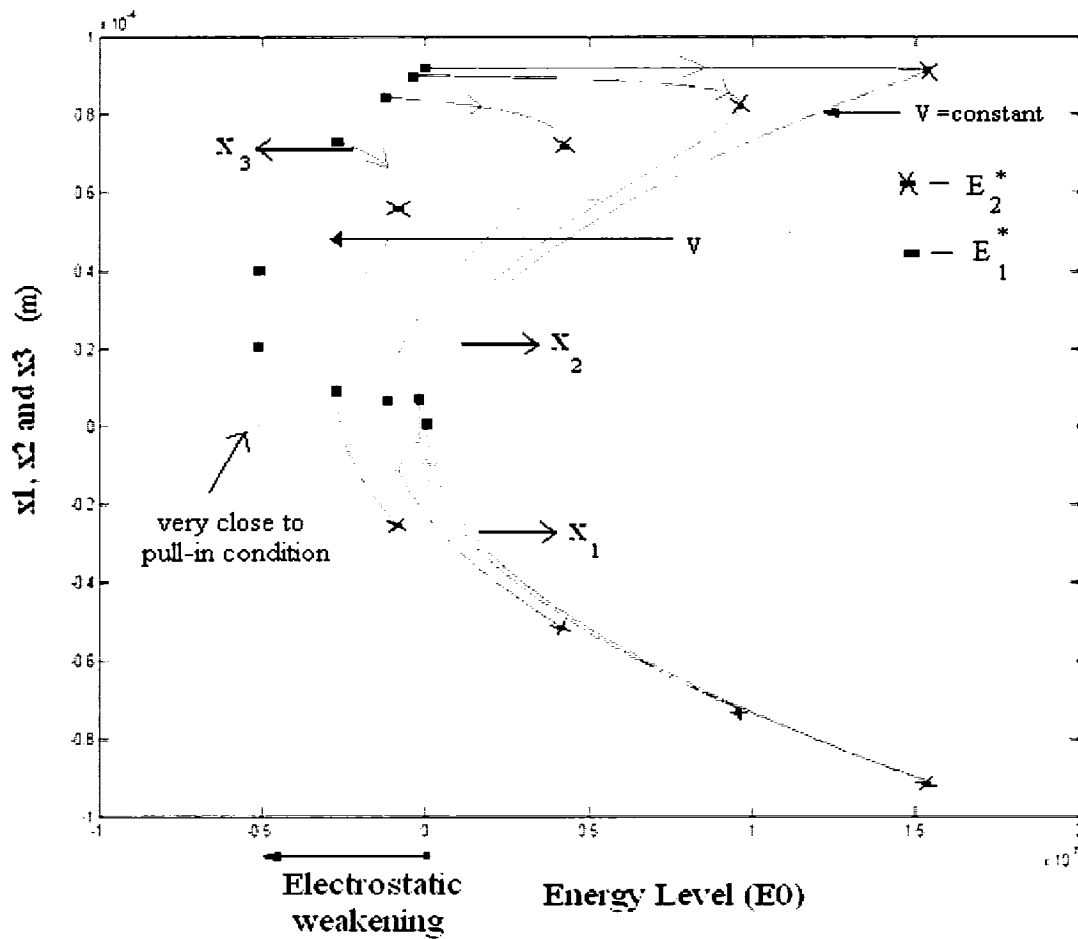
and the system becomes unstable.

Fig. 4.12 Variation of x_1, x_2 and x_3 for varying E_0 at different voltages

4.3.2.3 Pull-in voltage

The pull-in voltage obtained from the force balance plot can be validated by determining the pull-in voltage based on the phase portrait method. Maximum energy value, E_2^*, has to be known for each voltage to find the pull-in voltage by this method as discussed earlier for the mass-spring model. As the voltage is increased, the gap between the two points (x_1 and x_2, x_3) at which the velocity is zero reduces which is seen in Figure 4.13. At a particular value of voltage, 68.4V in this case, velocity just becomes zero at a single point i.e. x_1, x_2 and x_3 are all of same value. It is seen from published results [70] that the pull-in value is 68.5V. Thus the pull-in voltage is determined by the phase portrait as explained and is in close agreement with the published result [70].
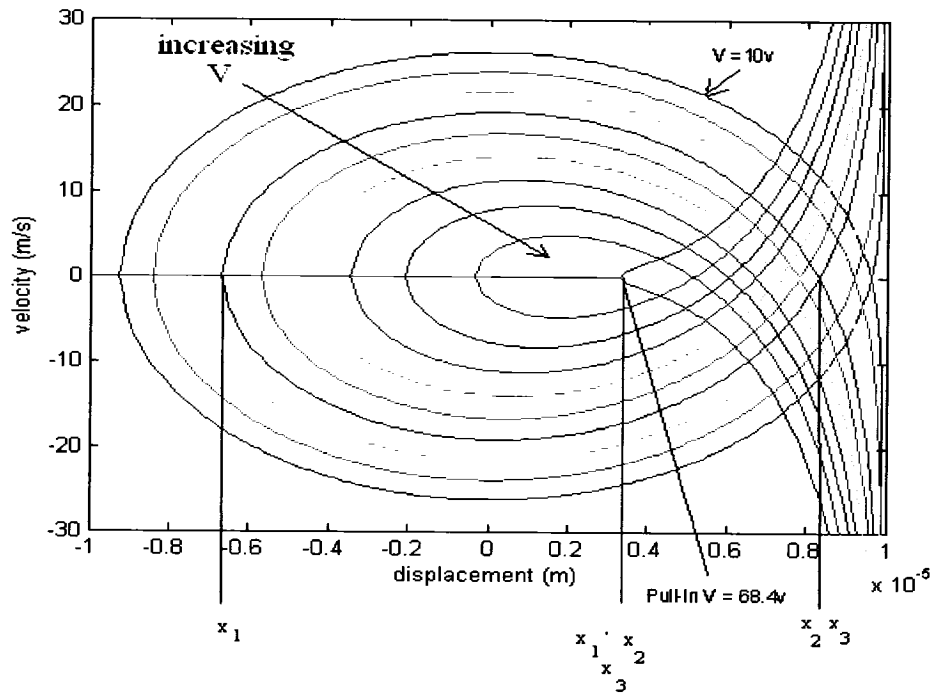

Fig. 4.13 Phase portrait for determining the pull-in voltage

The points at which the velocity becomes zero in Figure 4.13 for different voltages are plotted below in Figure 4.14. It is seen that the gap is reduced between the zero velocity points as the voltage increases. At the pull-in voltage, the points converge to a single point which indicates that the system becomes unstable at this voltage.
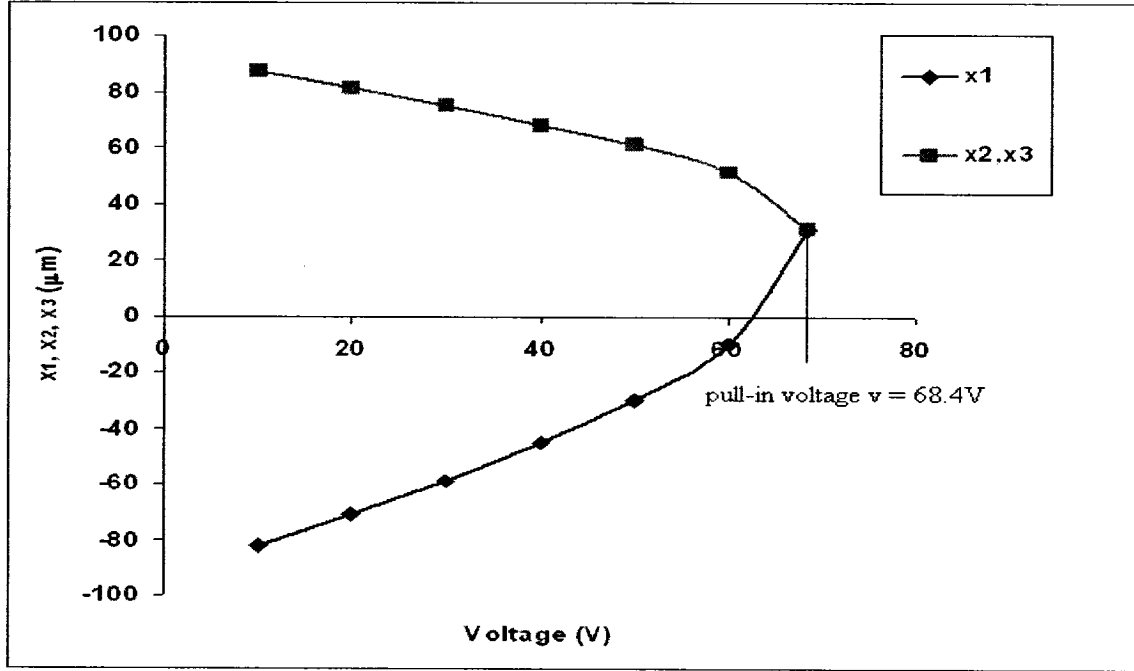

Fig. 4.14 Variation of x_1, x_2 and x_3 against voltage from the phase plot plotted at E_2^*

Thus the method of plotting the phase portraits based on the mass-spring model explained before in Section 4.3.1 is adopted for the lumped model of a cantilever system [70] as explained in this Section. The significance of the conservative energy level E_0, its variation and effects on the system behaviour is explained and the method of finding out the minimum and maximum values, E_1^* and E_2^* respectively, are presented. The various plots of x_1, x_2 and x_3 points against voltage and E_0 values are plotted to understand the

phase portraits and hence the system changes have been inferred. Finally, the pull-in voltage investigation is done based on the phase portrait and the pull-in value is determined and validated with that of the force balance plot and also the published result [70].

4.3.2.4 Frequency determination

The nonlinear dynamic analysis is done in this section to study the frequency variation with the energy value E_0. The velocity Equation 4.17 is rewritten in the form of the time equation to obtain the time and hence the frequency which is explained below. The velocity equation is inverted and written as

$$\frac{dt}{dx} = \pm \frac{1}{\sqrt{\dfrac{E_0 + \left(\dfrac{\varepsilon_0 \varepsilon_r A_{eq_i} V_i^2}{d - x} \right) - K_{eq} x^2}{M_{eq}}}} \tag{4.20}$$

The above equation is represented in the integration form as

$$t_p = \int_{x_1}^{x_2} \frac{dx}{\sqrt{\dfrac{E_0 + \left(\dfrac{\varepsilon_0 \varepsilon_r A_{eq_i} V_i^2}{d - x} \right) - K_{eq} x^2}{M_{eq}}}} \tag{4.21}$$

In the above equation, the limits x_1 and x_2 are obtained for each value of E_0 and voltage from their respective phase portrait. The time that is found here is for half the cycle of motion or it is the half-period. Hence the time period of oscillation is $T = 2t_p$ and the frequency of vibration is given by

$$\omega = \frac{2\pi}{T} \tag{4.22}$$

85

or $\omega = \dfrac{\pi}{t_p}$

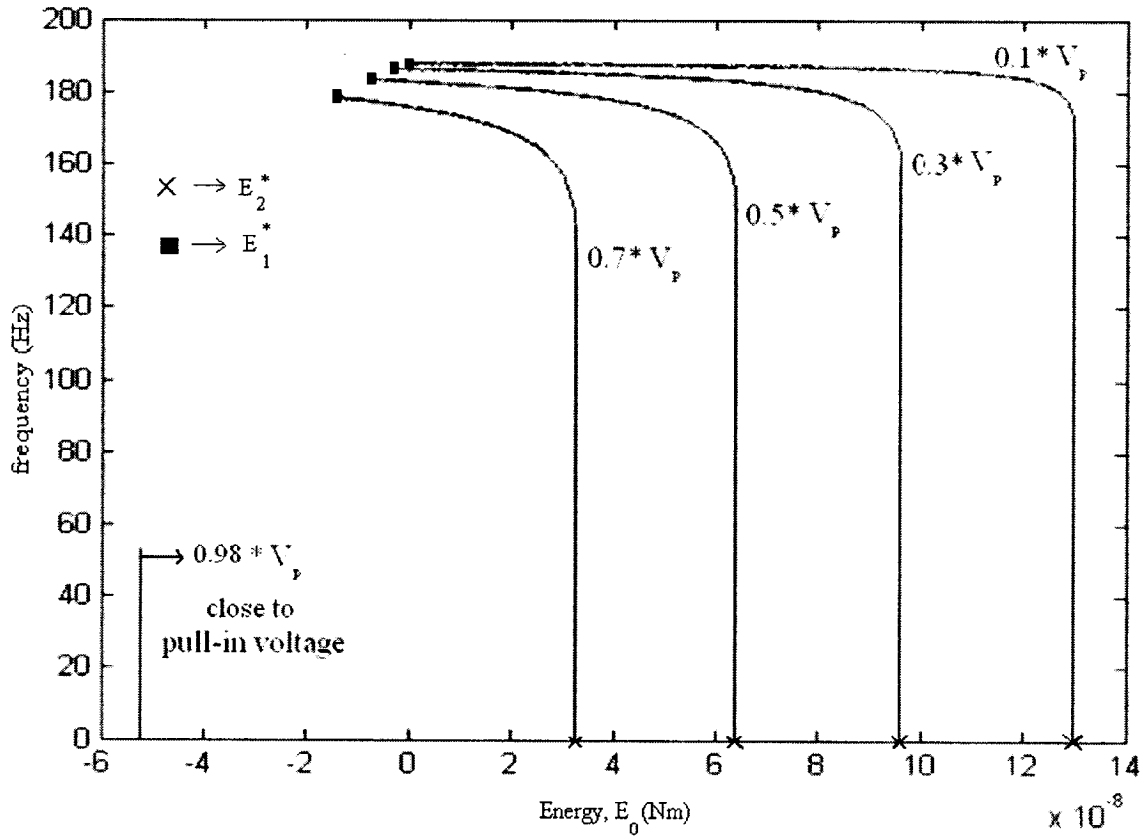<div align="right">(4.23)</div>

Fig. 4.15 Variation of frequency against the energy level E_0 for varying voltages

Thus the frequency is calculated and plotted as shown in Figure 4.15. From the figure, the frequency curve starts at E_1^* and reduces slowly for increasing E_0 and drops rapidly for small changes of E_0 when it is close to E_2^* and suddenly the frequency becomes zero at E_2^* for a particular value of voltage. It is seen that the frequency curve on the top starts at E_1^* and slowly reduces with increasing E_0 and at E_0 value of $13x10^{-8}$ which is the E_2^*, the frequency becomes zero with a rapid reduction for the voltage of $0.1xV_p$, where V_p is the pull-in voltage obtained from the phase portrait. Similar curves are plotted for varying

voltages expressed as a parameter normalized with pull-in voltage. As the voltage is increased, the range of frequency reduces similar to the E_0 value and at values of voltage very close to pull-in voltage, $0.98xV_p$ in this case, the frequency curve is very steep due to a very small range of E_0. At the pull-in voltage, the frequency is zero since the device is already snapped.

Thus the frequency calculation or the dynamic analysis of MEMS cantilevers undergoing electrostatic actuation is done using the nonlinear method as explained above. The frequency plot can also be plotted against voltage for different values of E_0 which will be explained in the next section for the MicraGeM cantilever case.

4.3.3 MicraGeM cantilever converted to a mass-spring model

So far, the nonlinear analysis has been done for the mass-spring models whose design parameters will not be used for testing purposes as they were taken only for theoretical analysis. Hence, a microfabricated cantilever from the MicraGeM technology which has to be tested later is analysed in this section based on the nonlinear methods explained in previous Sections 4.3.1 and 4.3.2. The MicraGeM cantilever is converted to a simple mass-spring model similar to the cantilever. As explained in the previous chapter, the equilvalent stiffness, mass and electrostatic areas are found out. The design parameters of the cantilever which is used for analysis is given below in Table 4.1. As the phase portrait techniques, its significance and the importance of E_0, pull-in voltage investigation and the frequency determination were all explained in the previous sections for the cantilever

87

system [70], the results and plots obtained for the MicraGeM cantilever analysed are just shown rather than explaining their significance again. Hence the Figures from 4.16 to 4.20 are obtained for the MicraGeM cantilever and they are briefly discussed below.

Table 4.1 Design parameters of the MicraGeM cantilever

E (kg/m^2)	ρ (kg/m^3)	L (μm)	B (μm)	t (μm)	d (μm)	ε_0 (F/m)
1.29×10^9	2.32×10^3	1000	100	10.7	10.5	8.85×10^{-12}

In Figure 4.16, a simple phase portrait is given for varying energy level E_0 at a constant voltage. The displacement values x_1, x_2 and x_3 at which the velocity becomes zero for varying E_0 values at a constant voltage is traced and is shown in Figure 4.17. The significance of the range of E_0 that can be applied for different voltages is studied by plotting the minimum and maximum energy values E_1^* and E_2^* for varying voltages which is shown in Figure 4.18. The next plot in Figure 4.19 is drawn between the voltage and the difference between E_2^* and E_1^* (ΔE) (E_1^* being taken as the absolute value) to understand the reduction in the range of E_0 values that can be applied to the system when the voltage value increases. The phase portrait shown in Figure 4.20 is plotted for different voltages with their respective E_2^* values to determine the pull-in voltage of the system.
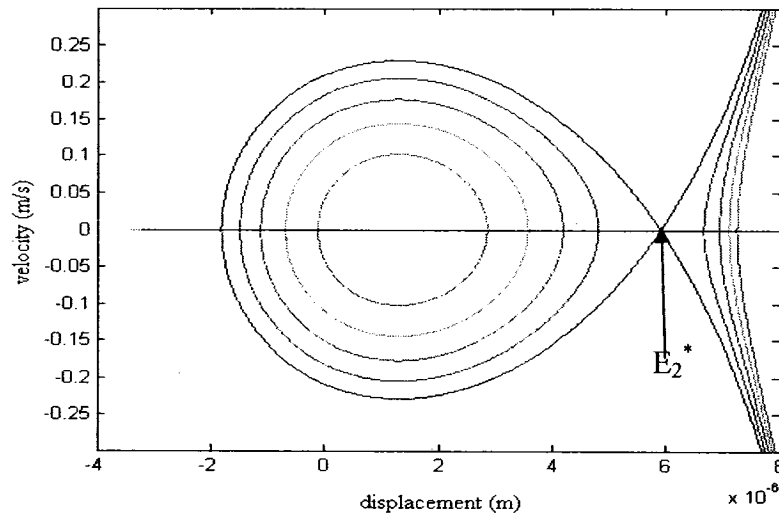
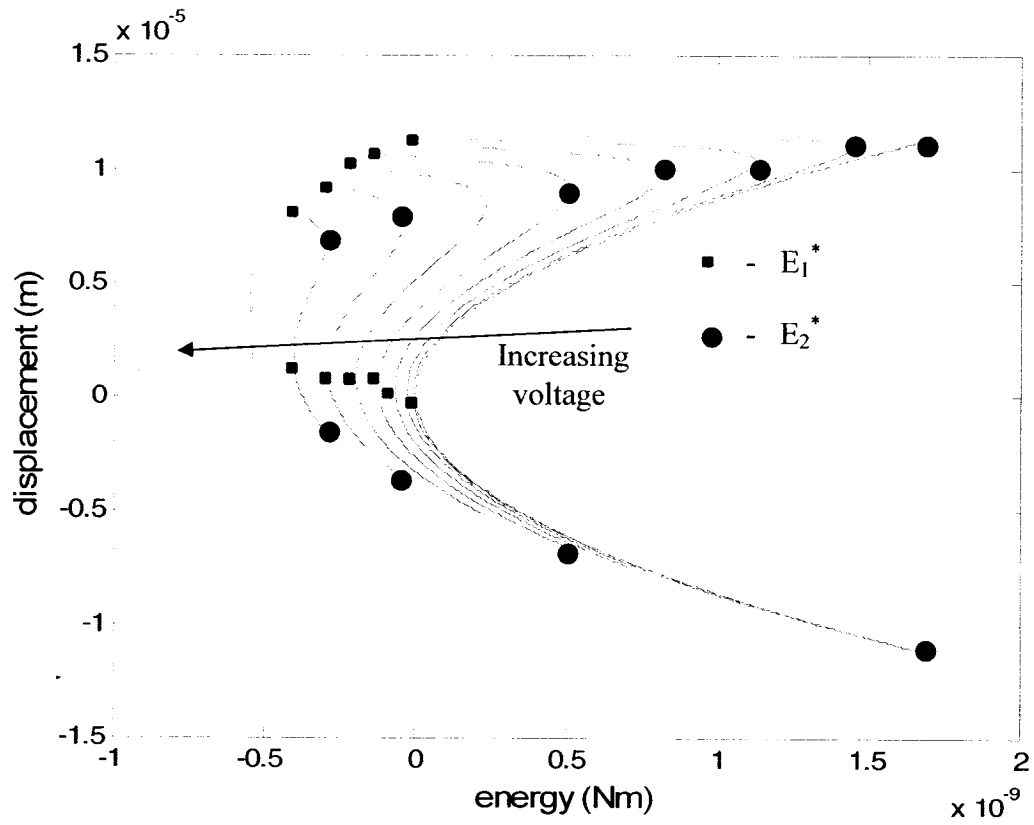Fig. 4.16 Example of a phase portrait with constant voltage and varying E_0

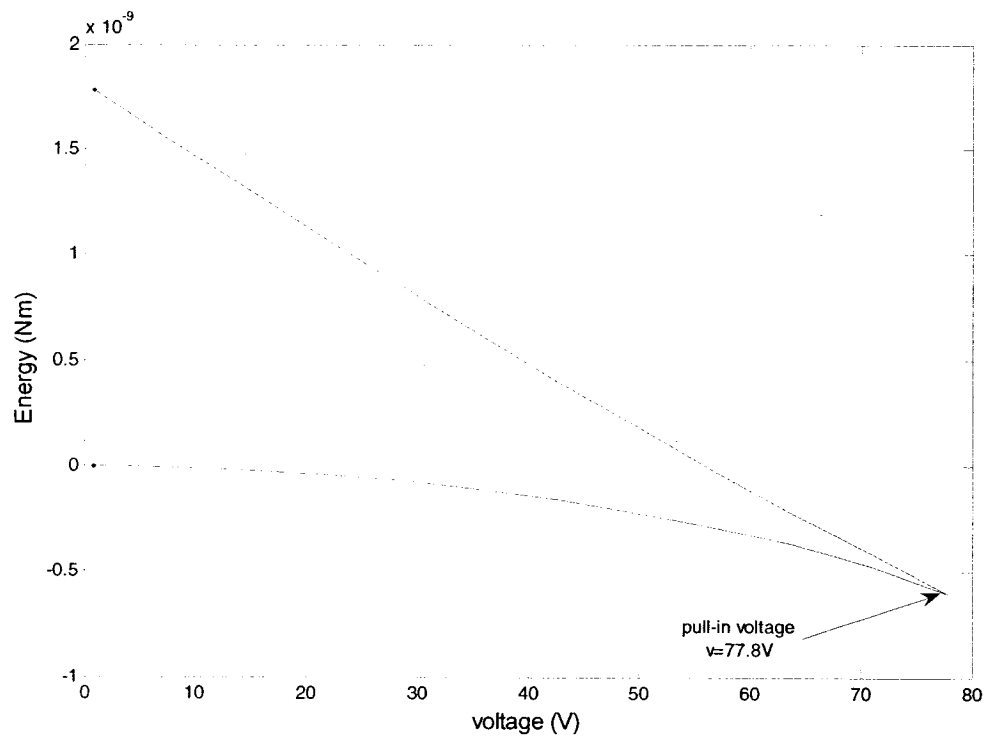Fig. 4.17 Variation of x_1, x_2 and x_3 for varying E_0 at different voltages

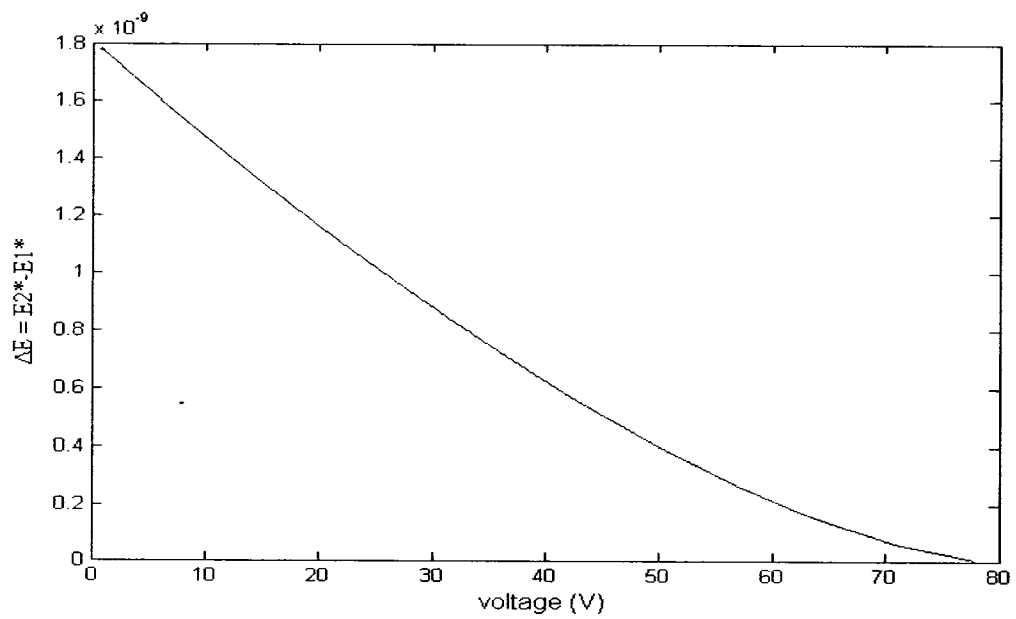Fig. 4.18 Variation of E_1^* and E_2^* for varying voltages

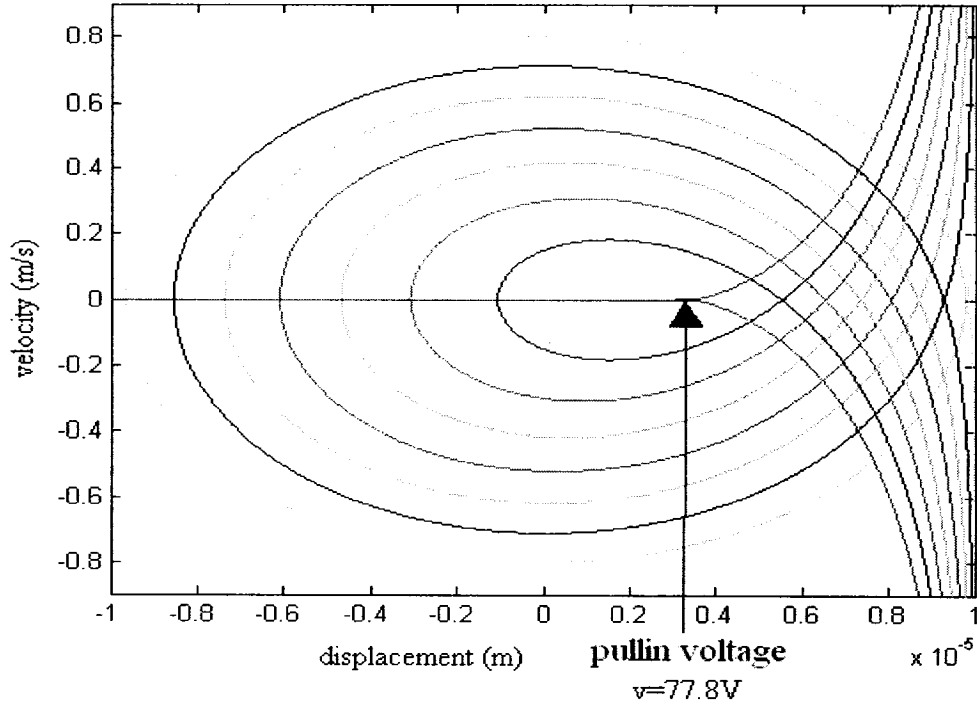Fig. 4.19 Variation of voltage against ΔE

Fig.4.20 Pull-in voltage determination based on the phase portrait

4.3.3.1 Frequency analysis

Hence the pull-in voltage determination and the significance of energy level E_0 plots were plotted for the MicraGeM cantilever as shown in previous section. In this section, the frequency plots are plotted for varying voltages and at different energy values E_0. The equation for selecting the E_0 is given as

$$\Delta E = E_0 - E_1^* = \text{a constant value} \tag{4.24}$$

While selecting E_0 value, care is taken to maintain the ΔE constant throughout. There is a value of voltage for every E_0 value at which the frequency becomes zero which can be

seen in Figure 4.21. When the frequency is plotted with voltage while E_0 being just the

E_1^* value at different voltages, the frequency value becomes zero at the pull-in voltage

which is the same as obtained from the phase portrait i.e. 77.8V. Similarly, at different E_0

values, different pull-in voltages can be calculated. When the same plot is plotted with E_0

value as E_2^*, the frequency obtained will be zero for all value of voltages. Hence the

frequency curves are obtained for varying voltages and at different energy values E_0.

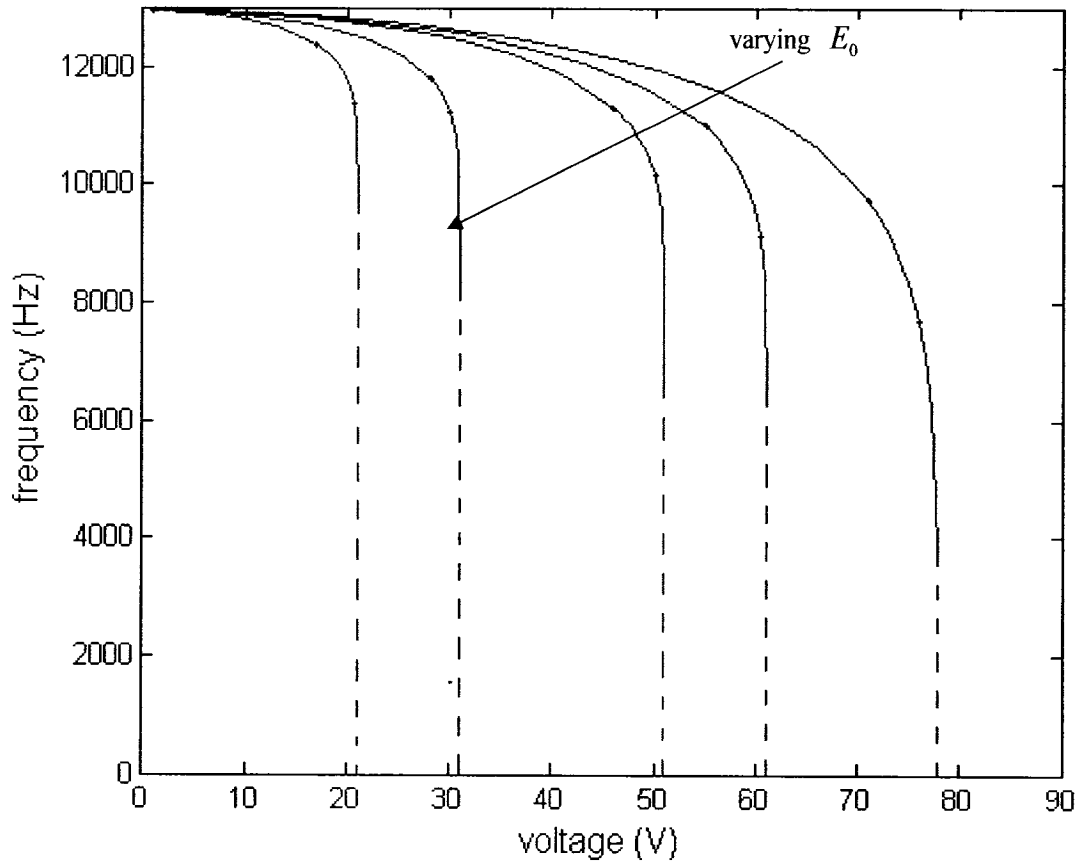Different pull-in voltages are obtained at different E_0 values.

Fig. 4.21 Frequency against voltage for varying energy values E_0

4.3.3.2 Validation

In this section, the nonlinear dynamic analysis employed in the present work is compared with the results obtained from the linear analysis adopted by Rinaldi et al. [76]. The dimensions taken for both the cases are given below in Table 4.2.

Table 4.2 Design parameters taken for the comparision between linear and nonlinear analysis adopted for finding the frequency of a MEMS cantilever

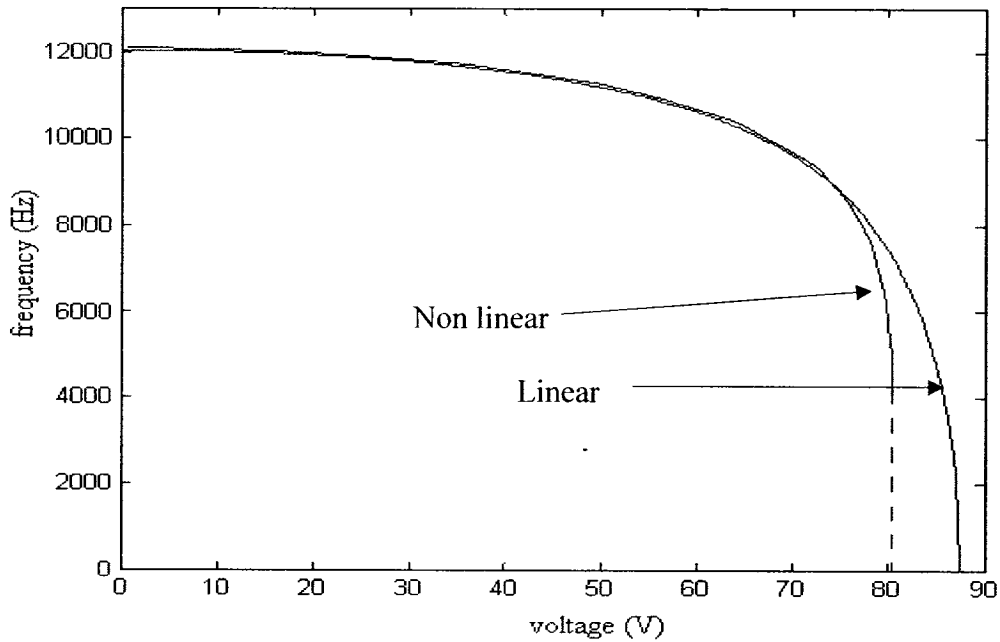| E (kg/m^2)	ρ (kg/m^3)	L (μm)	B (μm)	t (μm)	d (μm)	ϵ_0 (F/m)
1.29x10^9	2.32x10^3	1000	100	10	11.5	8.85x10^{-12}

Fig. 4.22 Comparision of frequency against voltage based on linear and nonlinear analysis

93

It can be seen from Figure 4.22 that the frequency for both the cases is almost the same value till 75V. But for voltages above 75V, the frequency reduces drastically for the non linear method than that of the linear method. The pull-in voltage is 80.5V from the nonlinear analysis while it is 88V from the linear analysis based on [76]. Thus there is a reduction in the value of the pull-in voltage obtained by the method employed in this work compared to the linear method [76] as seen in Figure 4.22. This is physically meaningful because the electrostatic force increases rapidly when the gap between the electrodes becomes small in a highly nonlinear fashion. It can be inferred that the linear analysis does not hold good for larger deflection ranges since it is an approximate method compared to the non linear method employed in our case. Also, it might lead to the failure of the device if it is operated for larger deflection purposes as the device might be already pulled-in even though it is in a safe region of operation based on the linear method. Hence, the non linear method employed in this work is suggested for finding the accurate pull-in voltage and the operation range of the MEMS devices.

4.4 Summary

In this chapter, an introduction to the non-linear analysis is given and different methods used to analyse the nonlinearity of the pendulum has been explained. The phase portraits have been plotted for the pendulum at different initial conditions to understand the nonlinearity. Similarly, these phase portrait techniques were employed for the simple mass-spring model undergoing electrostatic actuation and the pull-in investigation has been done and the pull-in voltage value has been evaluated. A cantilever system

converted into a lumped mass-spring model has been taken, the pull-in investigation is done and the results are compared successfully with the published results. The significance of the energy value E_0 has been explained to understand the system behaviour. The dynamic analysis is done based on the time integration and the frequency plots have been sketched with a constant voltage and varying energy value E_0. Similar analysis is done for the MicraGeM cantilever and various plots similar to the previous case were plotted. In this case, the frequency plot for varying voltages and at different energy values E_0 is shown. Also, the comparision of the nonlinear method is done with a linear analysis method and the results have been discussed. Thus the nonlinear analysis of MEMS structures has been done successfully in this chapter.

Chapter 5

Dynamic Experimental Testing

5.1 Introduction

In the previous chapter, the nonlinear analysis of both the simple mass-spring model and the cantilever system converted into a mass-spring model has been described and their pull-in voltages and frequencies have been evaluated. In this chapter, experimental testing methods, the test set-up and the test results for a MEMS cantilever microfabricated through the MicraGeM process technology will be discussed. The main objective of testing devices is to validate the design and simulation process in the developmental phase. Theoretical methods alone cannot be relied upon for doing the performance analysis of the system since a number of constraints are involved in the analysis. The mathematical approach employed for analyzing the system is important since different methods can predict different behaviour of the system. Also, the size of the MEMS devices, microfabrication techniques and the tolerances that are provided will affect the real-time system behavior tremendously. Hence, experimental testing method for the dynamics of MEMS devices is necessary for developing reliable and marketable working systems. The main consideration is how to perform the measurements on the micro devices and represent its micromechanical elements. Different testing methods have been developed so far by various researchers to test these microdevices and have obtained their own results [77].

96

5.2 Different Testing Techniques

There are two main techniques [78, 79] that have been adopted so far for the testing of MEMS devices and they can be generalized as contact and non-contact testing methods. In case of finding the mechanical properties of the MEMS structures such as the Young's modulus and fracture strengths, different non-contact testing methods such as micro tension test [80], microbeam bend test [81], axisymmetric plate bend test [82], M-test [83] and dynamic tests [84] are carried out to test various clamped and free standing structures. By using contact methods, deflections of the MEMS devices are found out by means of using microprobe [85], a stylus [86] or a nano indenter [87]. Even though these contact techniques can give accurate results, the use of this technique might often result in the destruction of the devices. A non contact testing technique is adopted often since it is simple in terms of setting up the equipments and also, avoids causing any damage to the devices which is the case in contact methods. For example, interferometry principle is used in non contact testing methods which are based on the principle of measuring the deflections of micro beams by inferring the variations of optically induced fringe patterns [88] and hence there can be no possibility of the micro device to be in contact with any physical structure which might lead to its destruction. Although this method has various advantages, the main drawback of non contact optical method is the alignment of the light source, optical devices and the micro device. Also, the light scattered from the device and other equipments can also create a problem since the optical detector might detect light from various sources which will not yield correct results. After taking all the

positive and negative factors into consideration, a non contact optical testing method developed by Gino et. al [76] is adopted to test the micro cantilevers.

5.3 Test Set-up

Figure 5.1 shows the schematic representation of the dynamic testing set-up used for the measurement of the natural frequencies of the micro cantilevers which are excited by means of an electrical excitation. The experimental testing set up consists of a commercially available Bruel and Kjaer [89] Laser Doppler Velocimetry (LDV) with HeNe laser and a photodiode detector. LDV is the point measurement of the velocity by means of laser light and it is based on the principle of Doppler effect. The shift in the laser light frequency due to the change in the surface velocity of the micro device is called as the Doppler shift and the measurement of this shift leads to the measurement of the frequency of vibration of the device which is the principle of LDV. The micro cantilevers are actuated with both AC and DC voltages using a 5V power source and an AC/DC amplifier. The signal detection system consists of an oscilloscope for the time-domain reference and a spectrum analyzer for the frequency domain measurements. The entire test set-up is mounted on an optical table for the accurate measurement and for ease of operation since the table is a perfectly flat surface.

The nominal beam diameter at the output of the laser source is approximately 1mm. Since this value is too high to have the laser focused accurately on the micro cantilever device, a diverging-converging lens optical system is used to reduce the laser light spot

size according to the desired diameter. The adjustment between the two lenses towards

and away from the microdevice and also from the laser source is done by the fine-tuning

of the micro positioners. Also, a beam splitter is used between the two lenses to adjust the

intensity of reflected laser light falling back on the laser source. The complete optical

system comprising of the laser source, a divergent lens, a beam splitter and a convergent
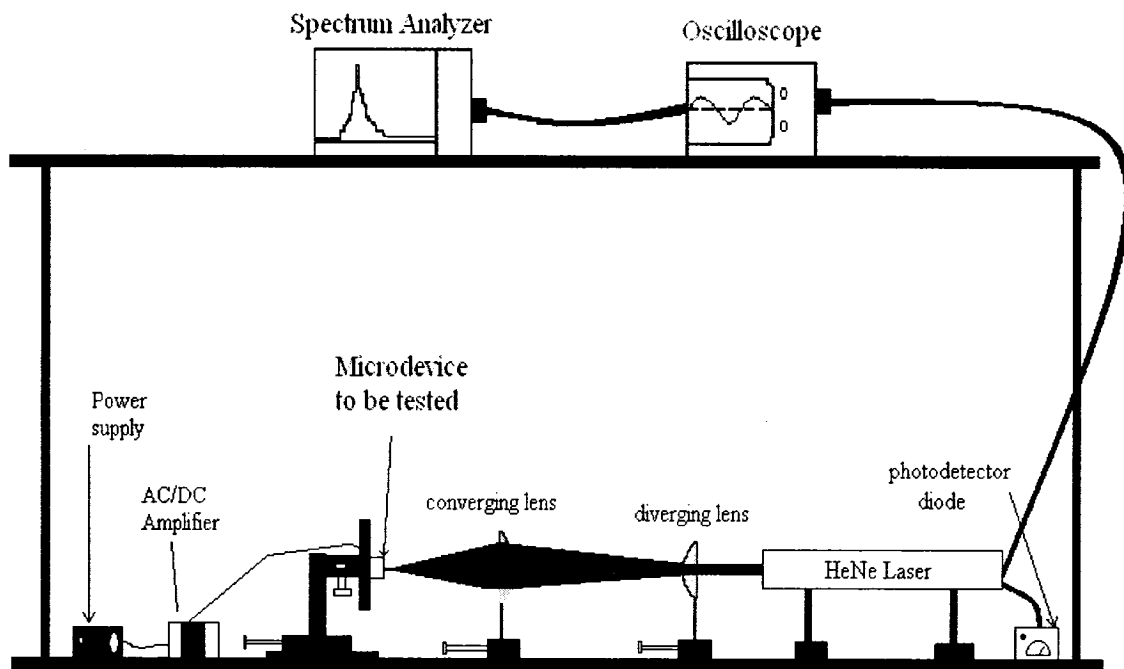
lens is shown below in Figure 5.1.

Fig. 5.1 Schematic representation of the experimental set-up

The excitation of the MEMS device can be done by both mechanical and electrical

sources. The mechanical excitation is done by means of mounting the device on a flat

acoustic speaker and based on adjusting the vibrations from the speaker, the intensity of

the device vibration can be varied. The other way of exciting the micro device is by

electrical excitation which is carried out by using an electrical power supply. This is the

99

type of excitation which is used to carry out our experiments as explained before. An AC/DC amplifier which is used to apply both AC and DC voltages to the micro device simultaneously is connected to the power supply. The micro device is mounted on a vertical clamping stand in such a way that the pins for the electrical connections of the packaged micro device chip comes on the back of the clamping stand for the ease of the connection purposes. A close-up view of the microchip clamped on the vertical stand with the help of an insulated tape is shown below in Figure 5.2.
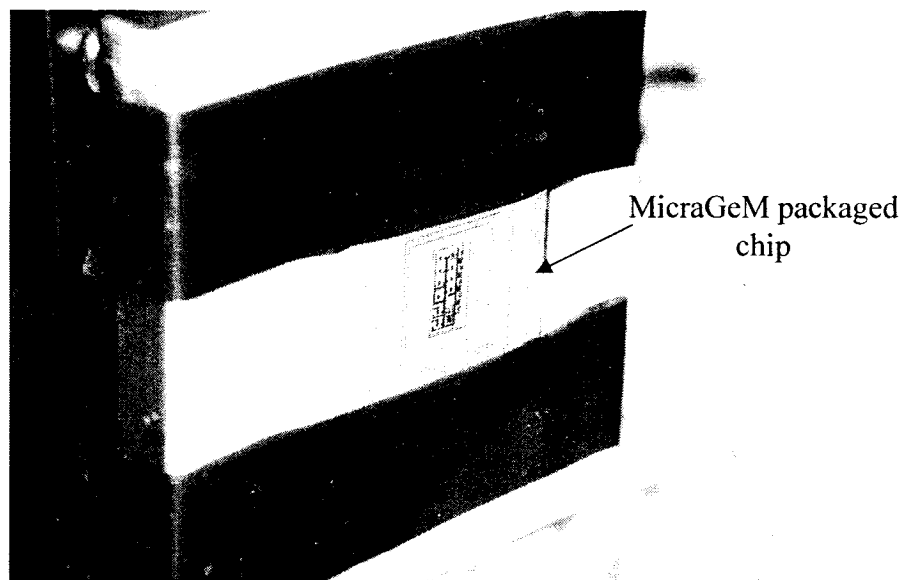
Fig. 5.2 A close-up view of the MicraGeM chip taken during the testing of the cantilevers

The laser light from the laser source is focused on the micro cantilever which is to be dynamically tested. The light is directed with the help of the convergent- divergent lens and the beam splitter for getting the required beam diameter focused on the device as shown in Figure 5.3. An optical microscope and a reflecting mirror set-up is employed to

have an enlarged view of the micro cantilever. This is done to have a clear view on the adjustment of the mirror set-up in the x, y and z-directions for the correct alignment of the laser light on the cantilever. Also, this microscopic image can be connected to a computer to view the direct image of the device movements in the monitor. The microscopic set-up with the MicraGeM chip is shown in Figure 5.4.
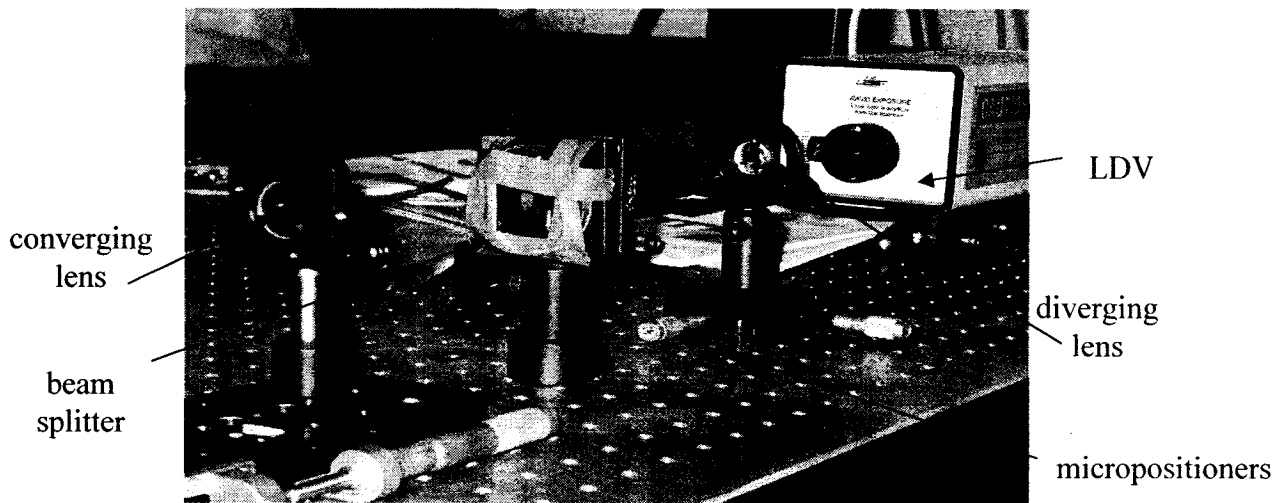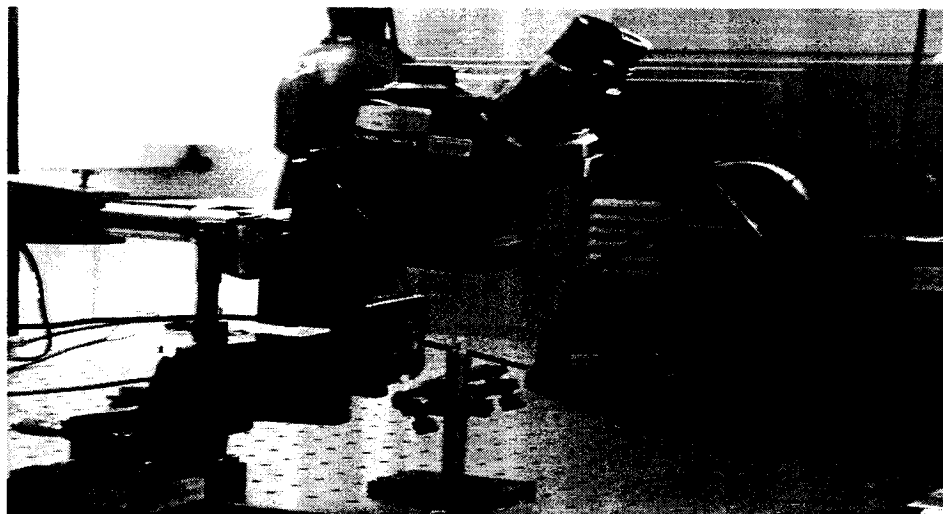

Fig. 5.3 The lens train consisting of convergent-divergent lenses and the beam splitter

Fig. 5.4 Microscopic set-up for an enlarged view of the micro cantilever

5.4 Testing Procedure and Test Results

The Figure 5.5 (a) gives the overview of the set-up that is used for the dynamic testing of the micro device. The pins of the micro cantilever are connected to the AC/DC amplifier which in turn is connected to the 5V power supply. When the required AC voltage is applied, the actuation of the cantilever occurs and hence the light reflected from the device suffers Doppler shift due to the surface velocity of the vibrating device. As explained before, the LDV measures this Doppler effect. The LDV is connected to the oscilloscope which in turn is connected to the spectral analyzer from which the amplitude and frequency responses of the vibration of the cantilever are obtained, respectively.

Consider Figure 5.5 (b) as the scheme for electrostatic testing. In this testing scheme, both AC and DC voltages are applied. The DC voltage provides the electrostatic bias while AC ($A_0\sin\omega t$) voltage excites the cantilever. The AC voltage with a peak-to-peak amplitude is applied on the system and hence the amplitude of vibration is dependent on the AC voltage. The DC voltage is a bias input that is given to the system and hence it leads to the bending of the cantilever beam. When both these voltages are applied as shown in the Figure 5.5 (b), the cantilever undergoes both the bending and the vibration at the same time. Thus the system is given a sweeping frequency over a range of 0-25kHz and the increase in the amplitude of vibration for frequencies close to its natural frequencies can be seen in the oscilloscope. Thus the peak in the frequency curve at their natural frequencies can be estimated using the spectral analyzer.
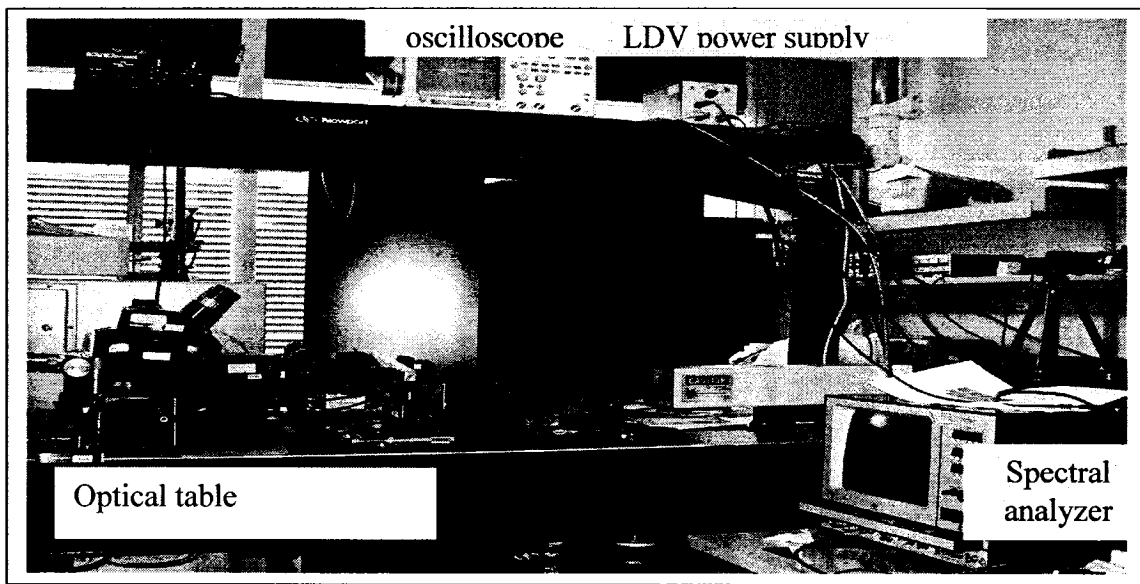
(a) Complete overview of the experimental setup
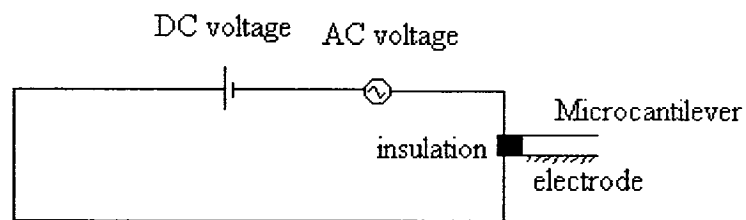
(b) Electrostatic testing scheme for the microcantilevers

Fig 5.5 Test setup and testing scheme

Then, the DC voltage is applied beginning from a zero value and slowly increased and when the voltages are close to the pull-in value obtained theoretically and no further increase in the voltage was applied. Also, when there is a huge reduction in the value of the frequency for a very small increase in the voltage, utmost care is taken in increasing the voltage further as the cantilever is close to the pull-in condition. The next step would be to increase the AC voltage and keep it at another higher fixed value and similar set of

103

values for increasing DC voltages are taken. Thus the frequency measurements are done for varying AC and DC voltages. Varying DC bias creates different nonlinear electrostatic condition, while varying AC amplitude represents the initial offset from the static equilibrium and thereby representing the value of E_0. Here, the different E_0 conditions were created by varying the amplitude of AC excitation signal while varying bias voltage of 'V' was created by changing the value of DC bias. By different combination of AC amplitude and DC value, one could create different nonlinear situation of electrostatically actuated structures.

The experiment is conducted on the MicraGeM cantilever whose dimensions were shown in Table 4.1. Other devices such as fixed-fixed beams are not tested since the theoretical prediction of their natural frequencies are found to be more than 25 kHz which is out of range of measurement using the current set-up. The values of AC voltages that are applied for the entire testing are 2,4,8,12,16 and 20V. For each set of readings, i.e. for each AC voltage, the DC voltage is varied from 0 to a value at which the frequency seems to reduce drastically compared to the previous value. Shown below in Figures 5.6 to 5.10 are the sample plots obtained from the spectral analyzer for particular values of AC and DC voltages. The frequency range which is swept is taken in the x-axis while the amplitude of vibration is taken in the y-axis. The peak values obtained are the natural frequencies of the cantilever beam at different voltage conditions.
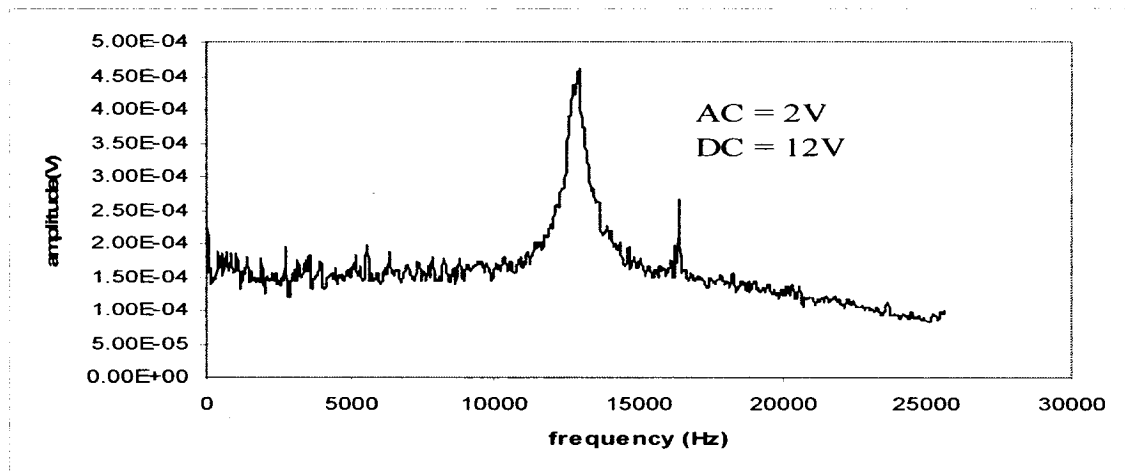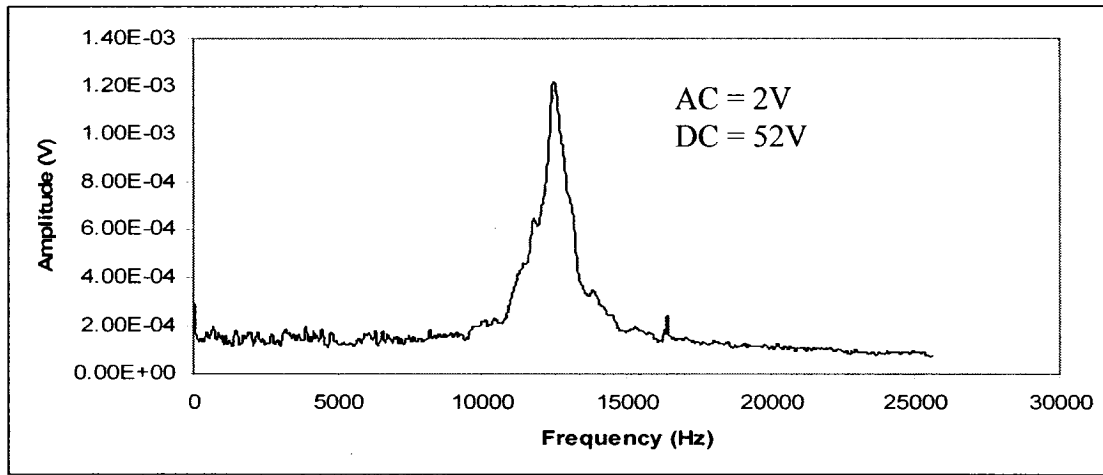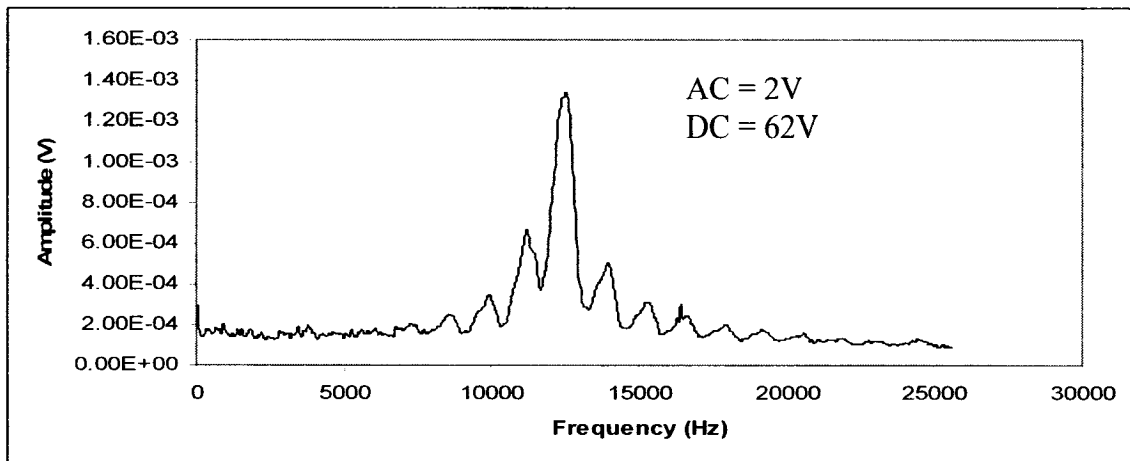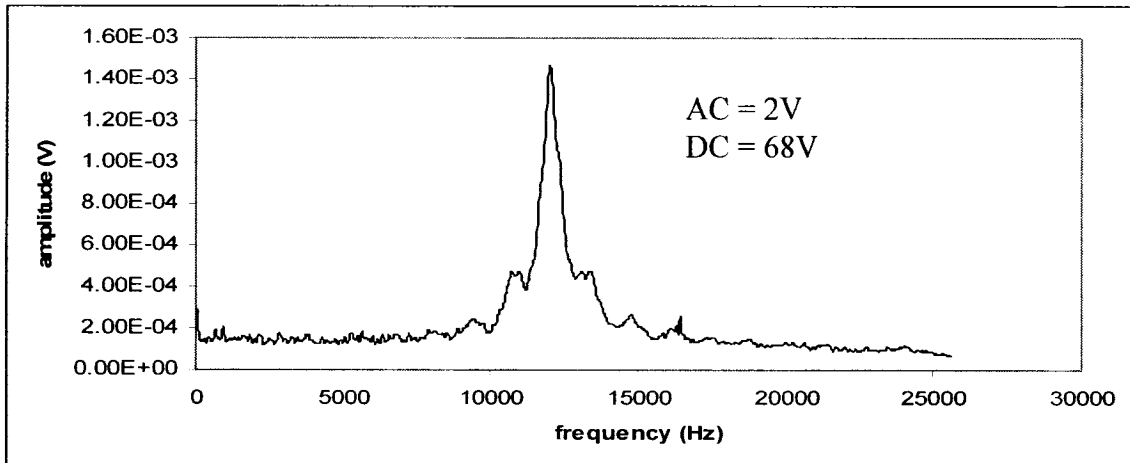
(a)
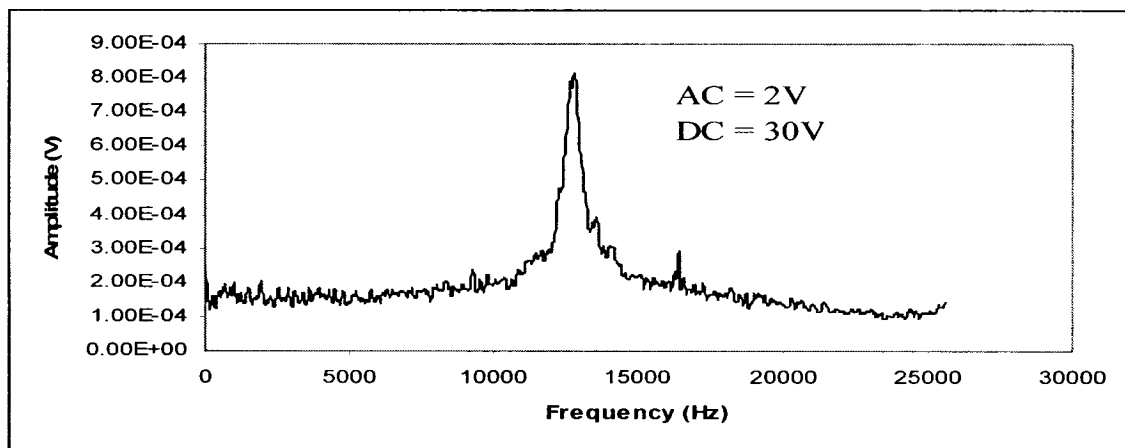
(b)
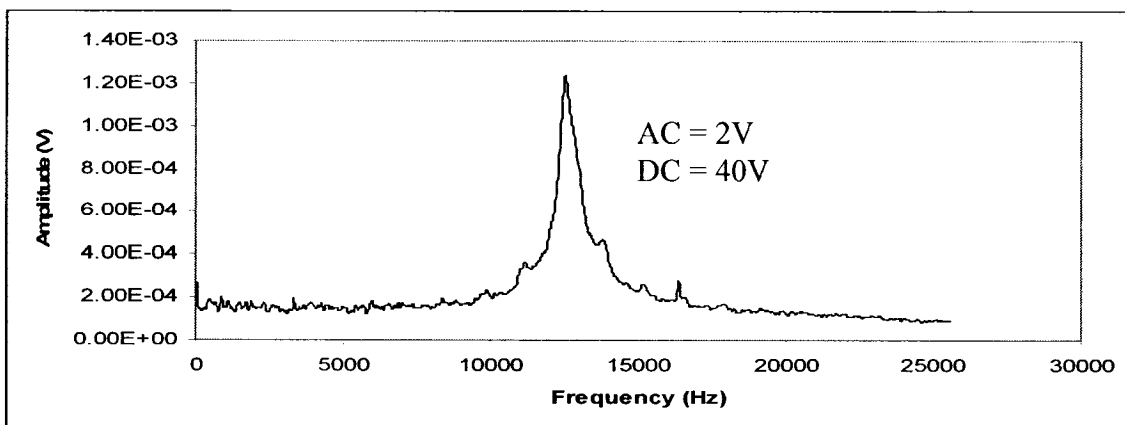
(c)

Fig. 5.6 Frequency response of the cantilever for constant AC = 2V and different DC voltages
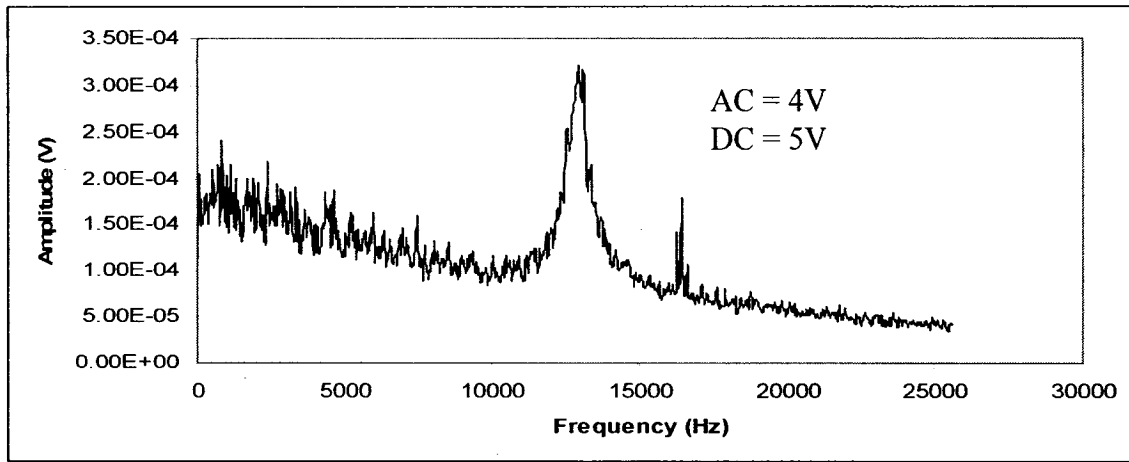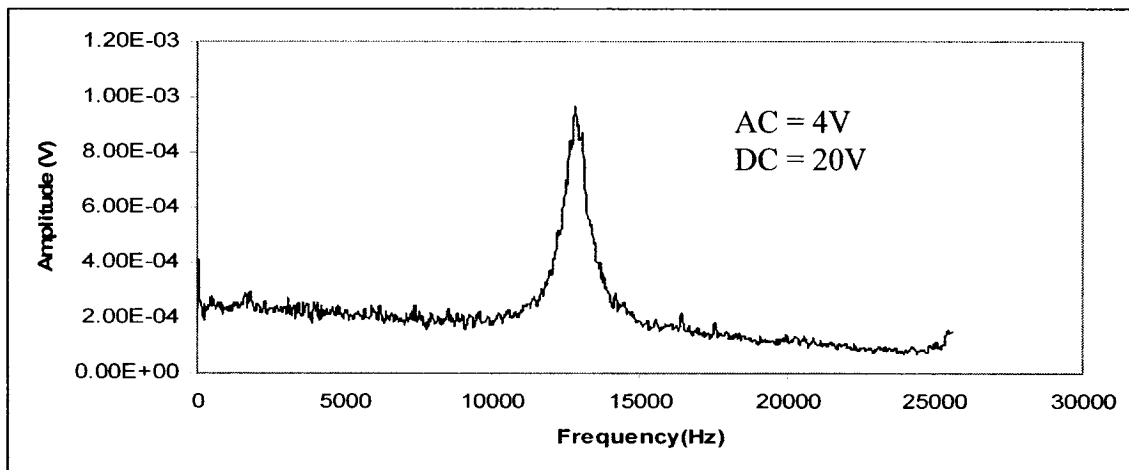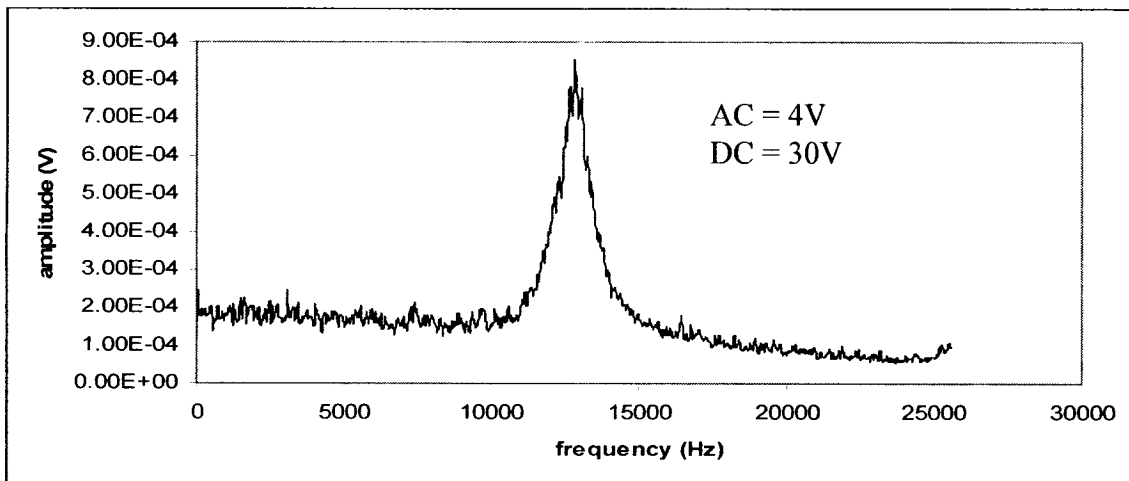
(d)

(e)

(f)

Fig. 5.6 Frequency response of the cantilever for constant AC = 2V and different DC
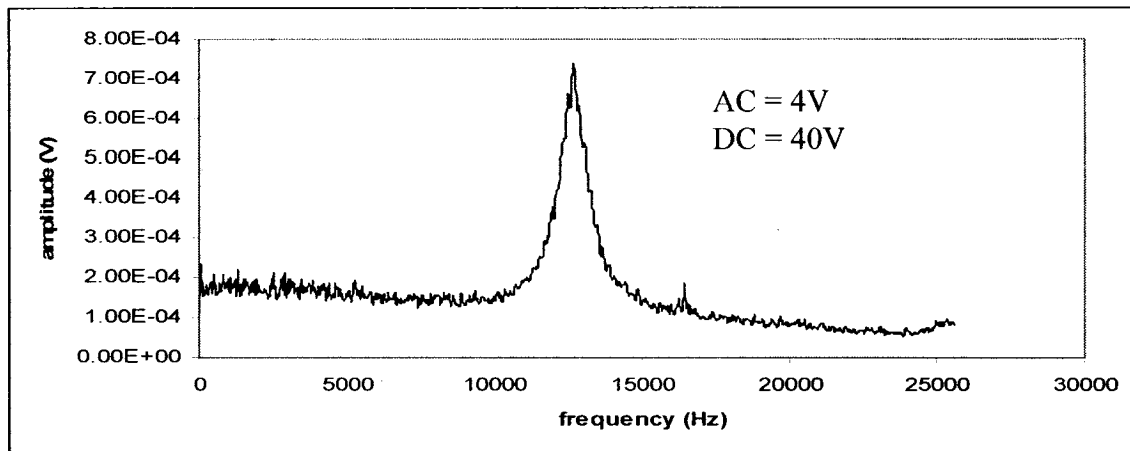
voltages

(a)

(b)
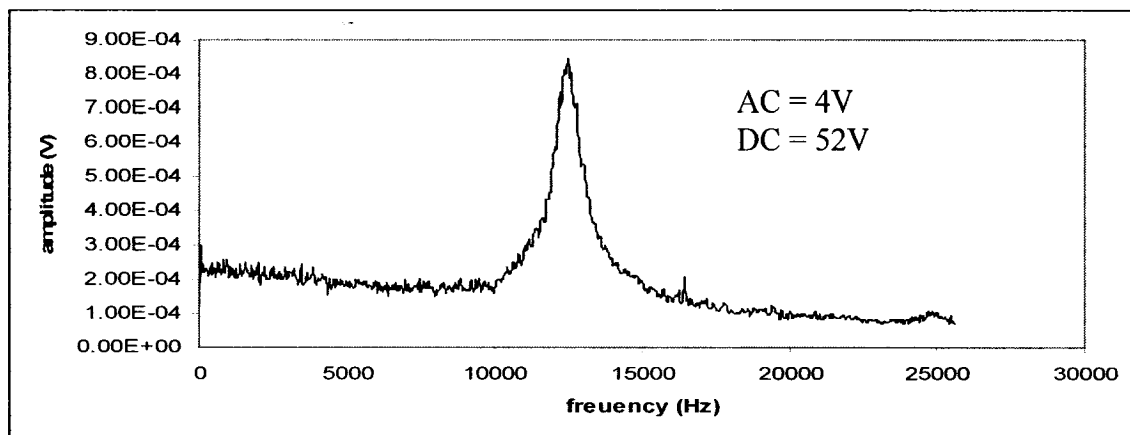

(c)

Fig. 5.7 Frequency response of the cantilever for constant AC = 4V and different DC

voltages

(d)

(e)

(f)

Fig. 5.7 Frequency response of the cantilever for constant AC = 4V and different DC
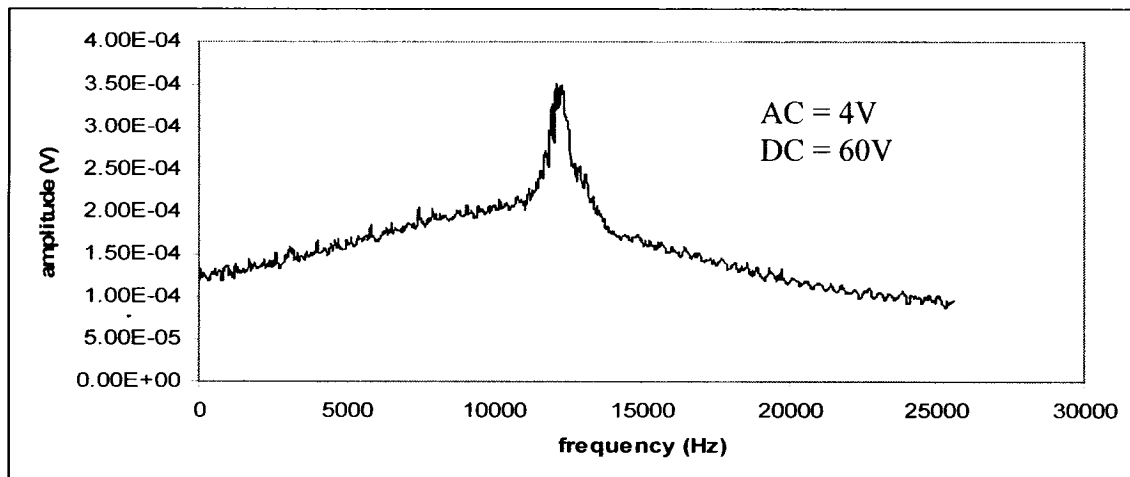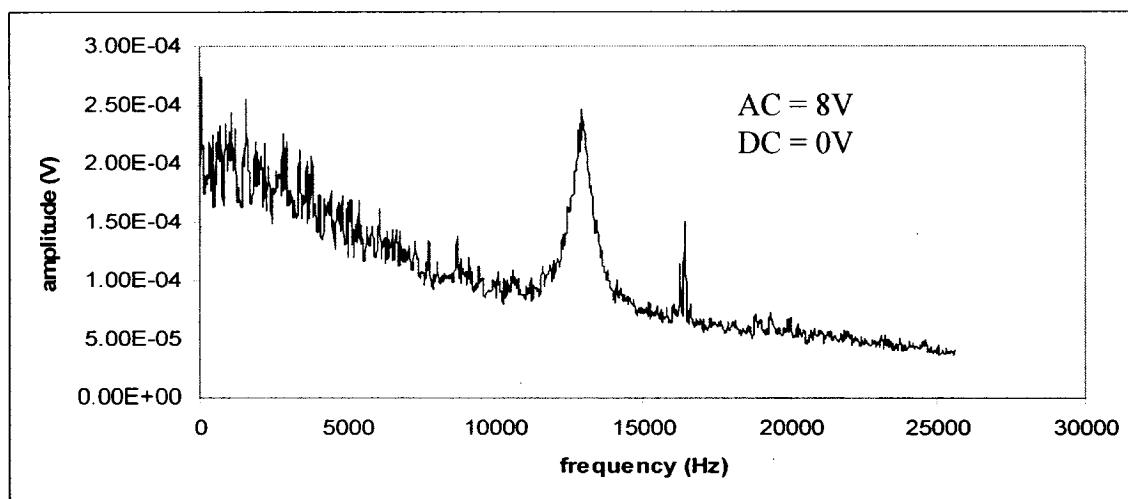
voltages

(a)

(b)

(c)

Fig. 5.8 Frequency response of the cantilever for constant AC = 8V and different DC
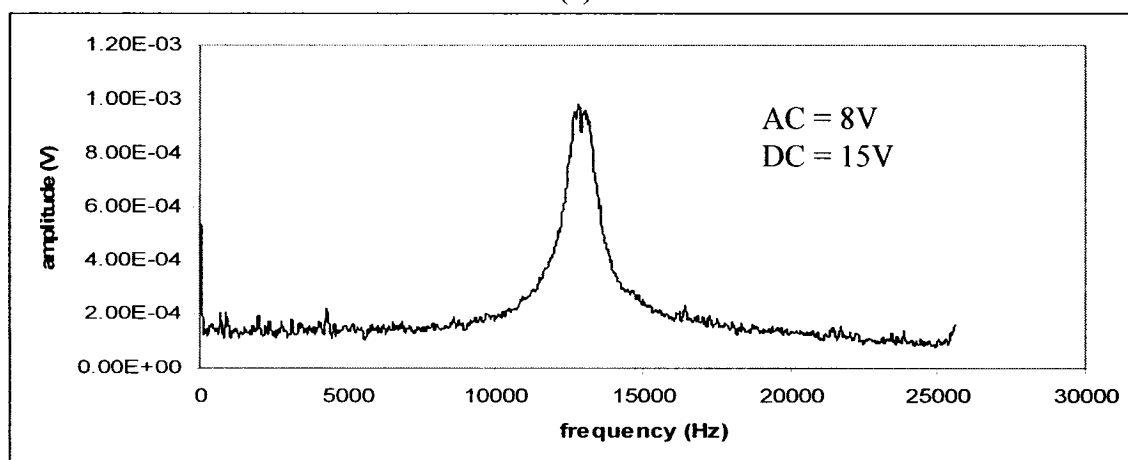
voltages

(d)

(e)

0

(f)

Fig. 5.8 Frequency response of the cantilever for constant AC = 8V and different DC
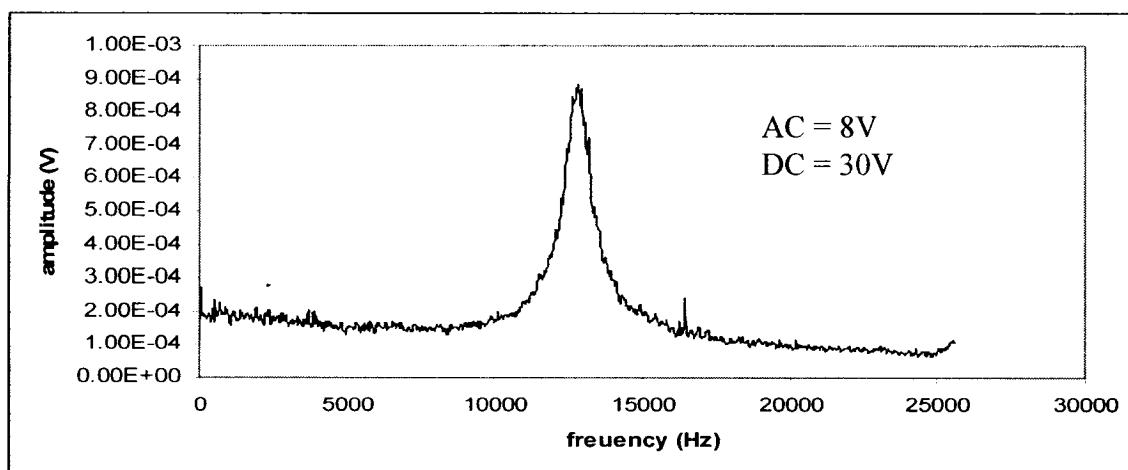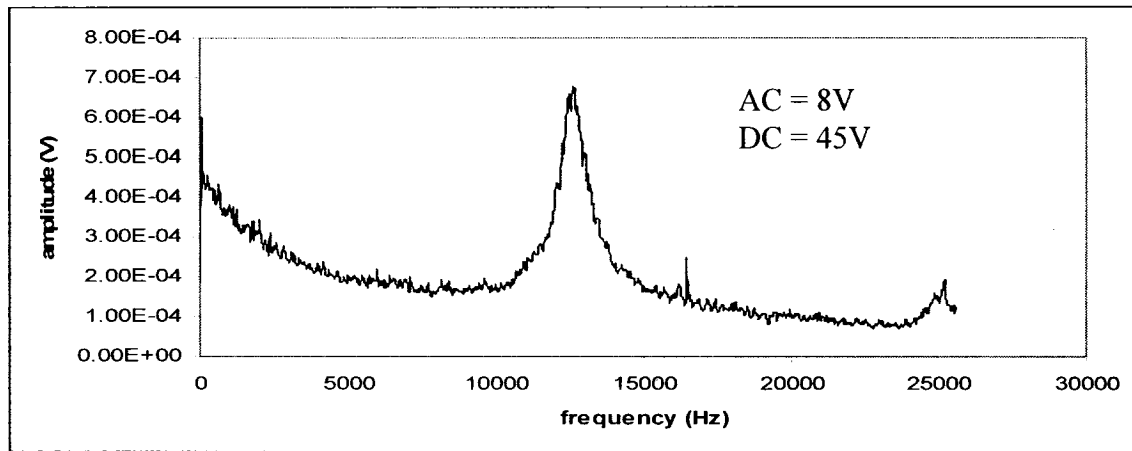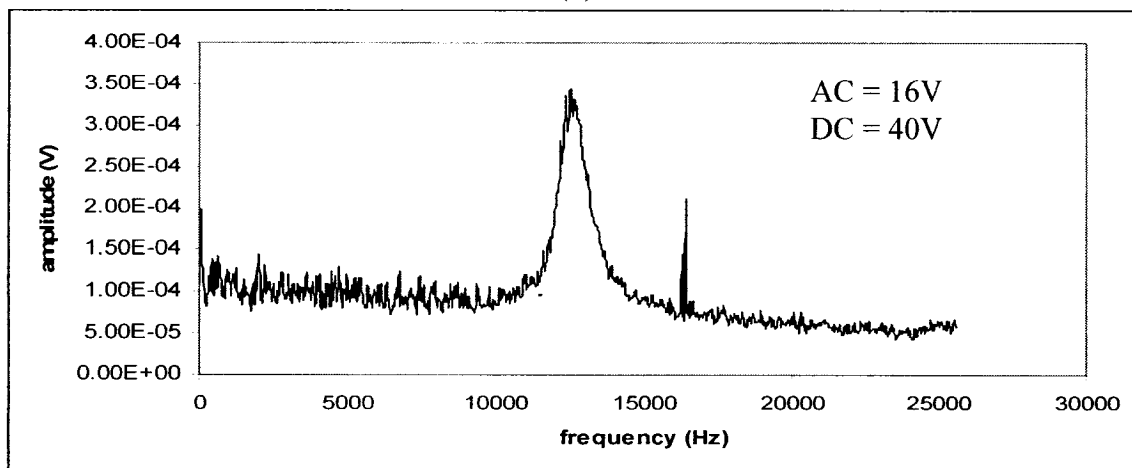
voltages

Fig. 5.9 Frequency response of the cantilever for constant AC = 16V and different DC
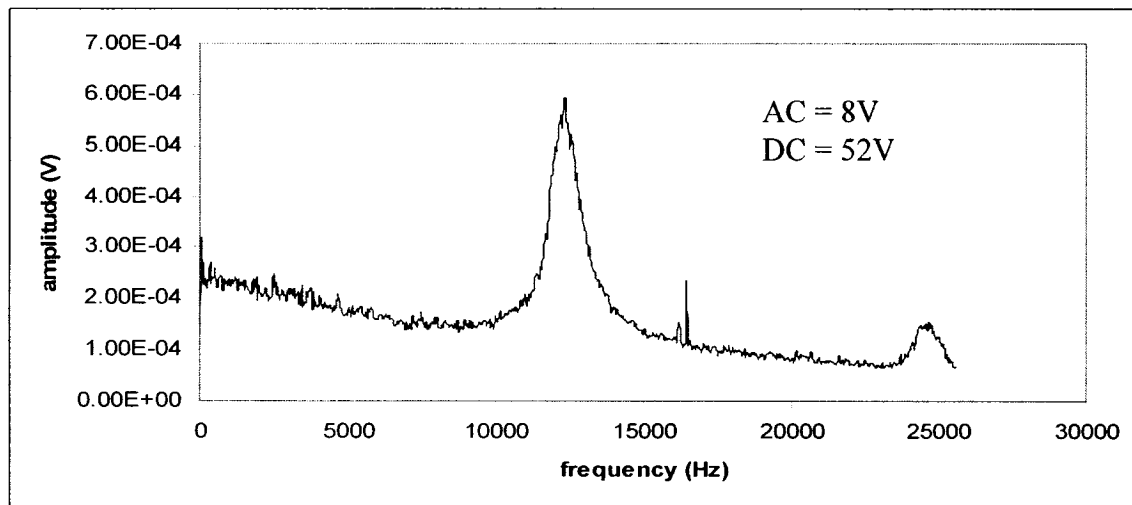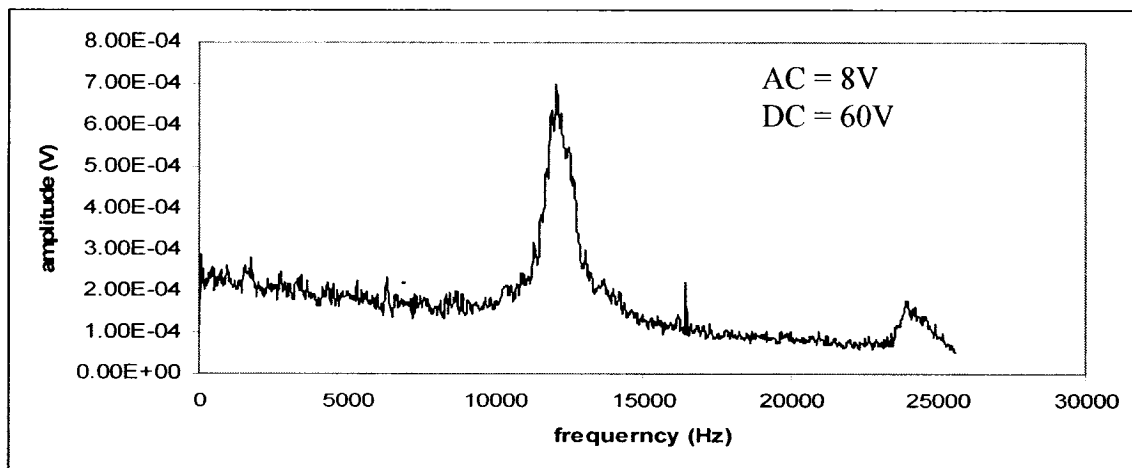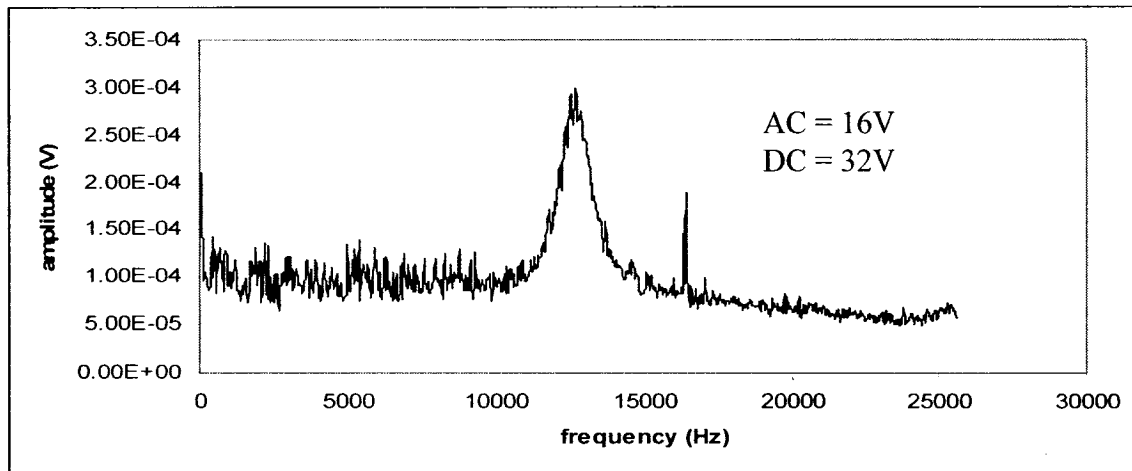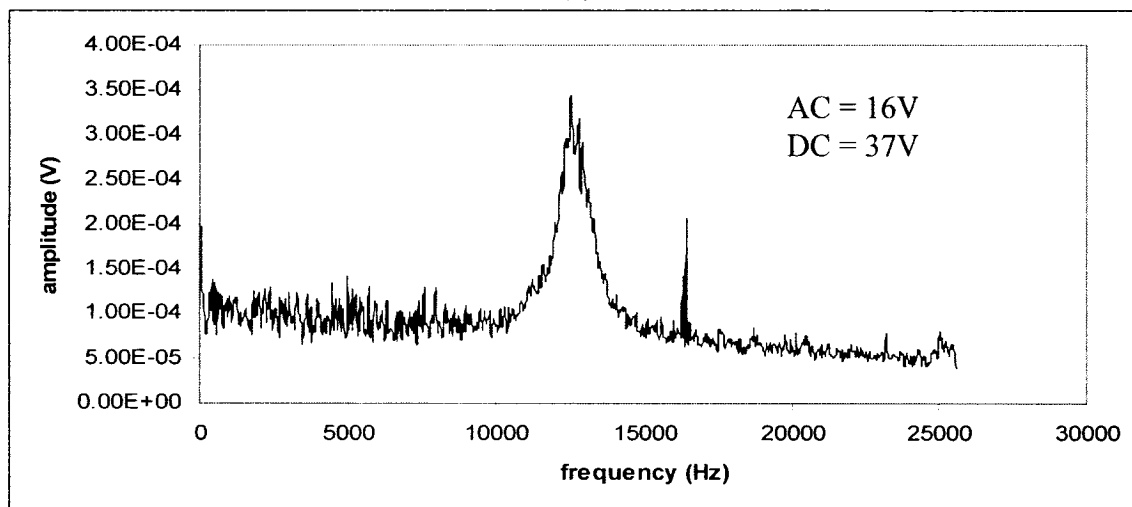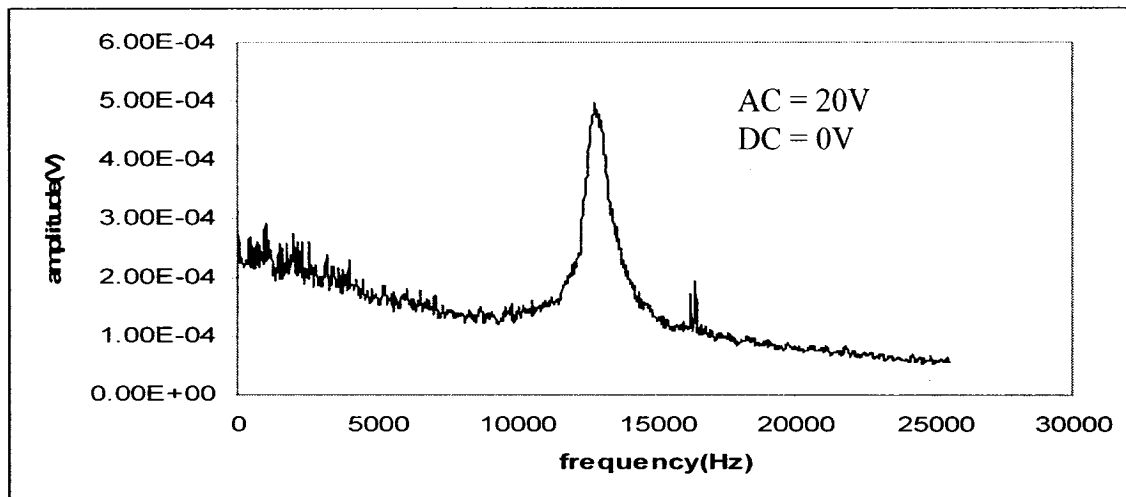
voltages

(a)
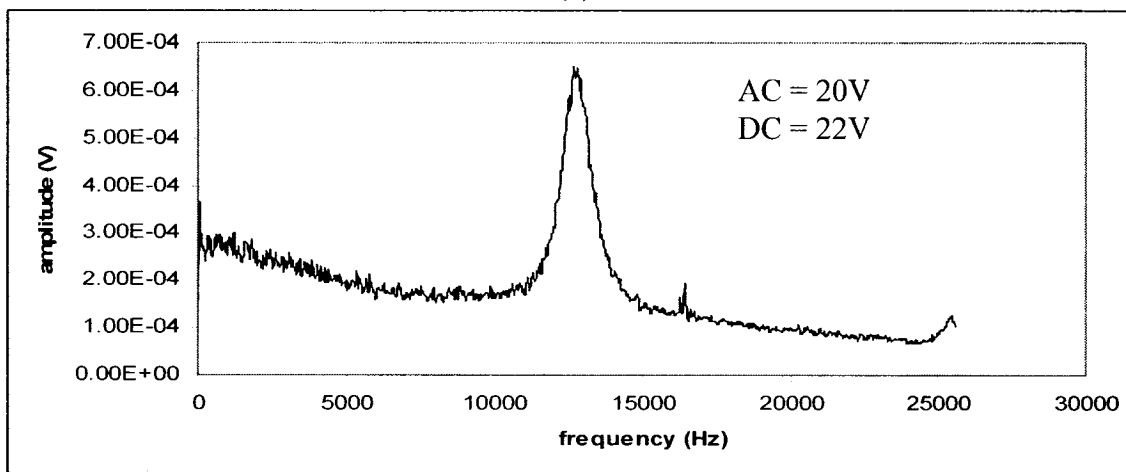
(b)
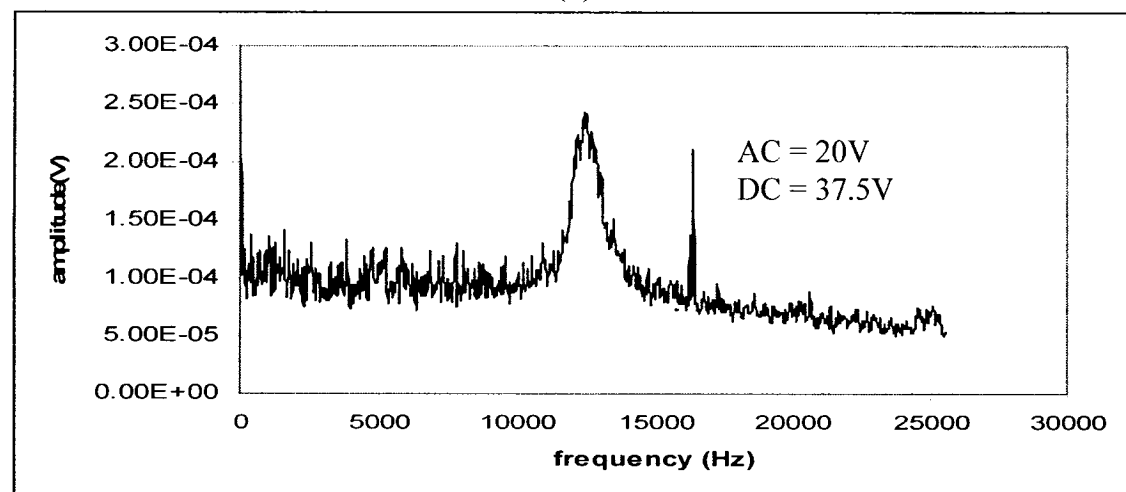
(c)

Fig. 5.10 Frequency response of the cantilever for AC = 20V and different DC

voltages

For a particular AC voltage, different natural frequencies (peak values) are obtained for different DC voltages close to the pull-in voltage values. Similarly, for various AC voltages, various sets of readings of the frequency values are taken. It is absolutely necessary to stop applying the voltage when the reduction in the frequency value is too large for a very small increase in the DC voltage. For example, in the case of 4V AC voltage, for initial smaller values of DC voltage, the frequency reduces by 10Hz for an increase of 10V DC approximately. But at 67.5 V DC, the frequency reduced by 100Hz for a further increase of 0.5V DC. Hence no further increase in the DC voltage is done since it might damage the cantilever due to the pull-in condition. Small value of AC amplitude is assumed to provide a condition of $E_0 \cong E_1^*$. The higher value of AC amplitude is expected to move closer to the condition $E_0 \cong E_2^*$. The Figures 5.11 to 5.16 show the plot of natural frequency against the DC voltage for different AC voltages.
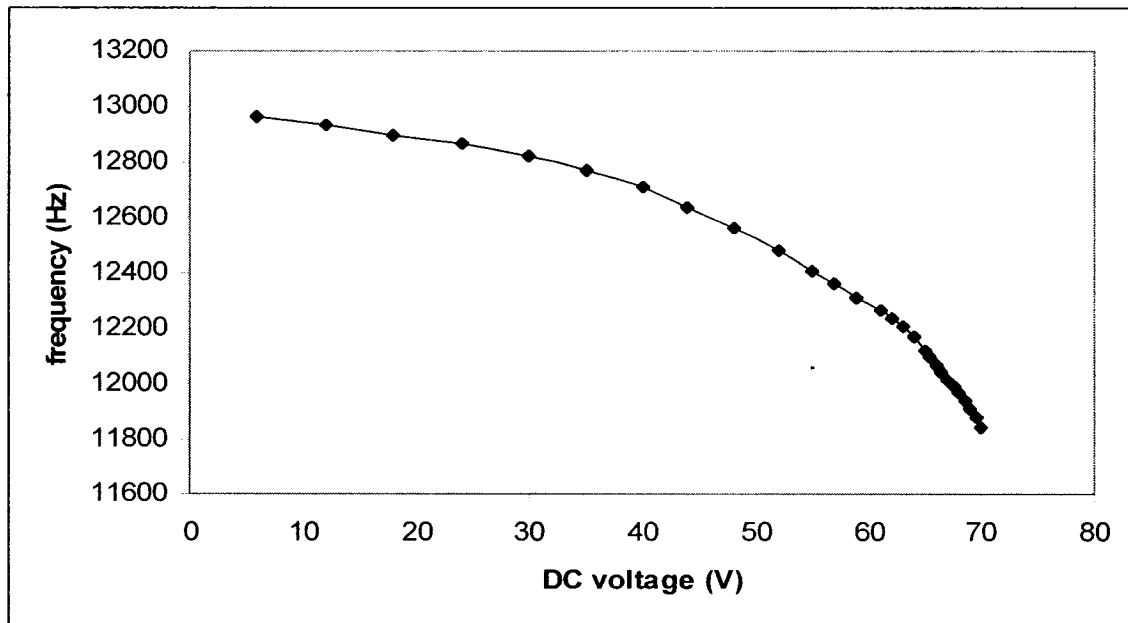
Fig. 5.11 Variation of experimental natural frequency against DC bias voltage at 2V AC
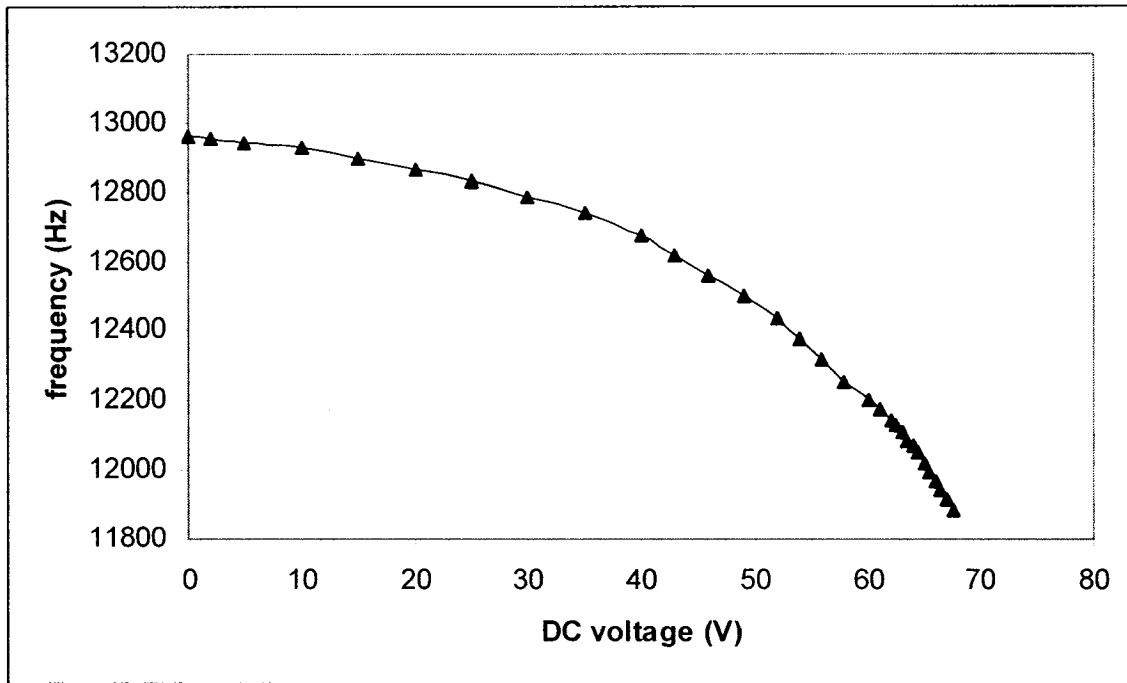
Fig. 5.12 Variation of experimental natural frequency against DC bias voltage at 4V AC
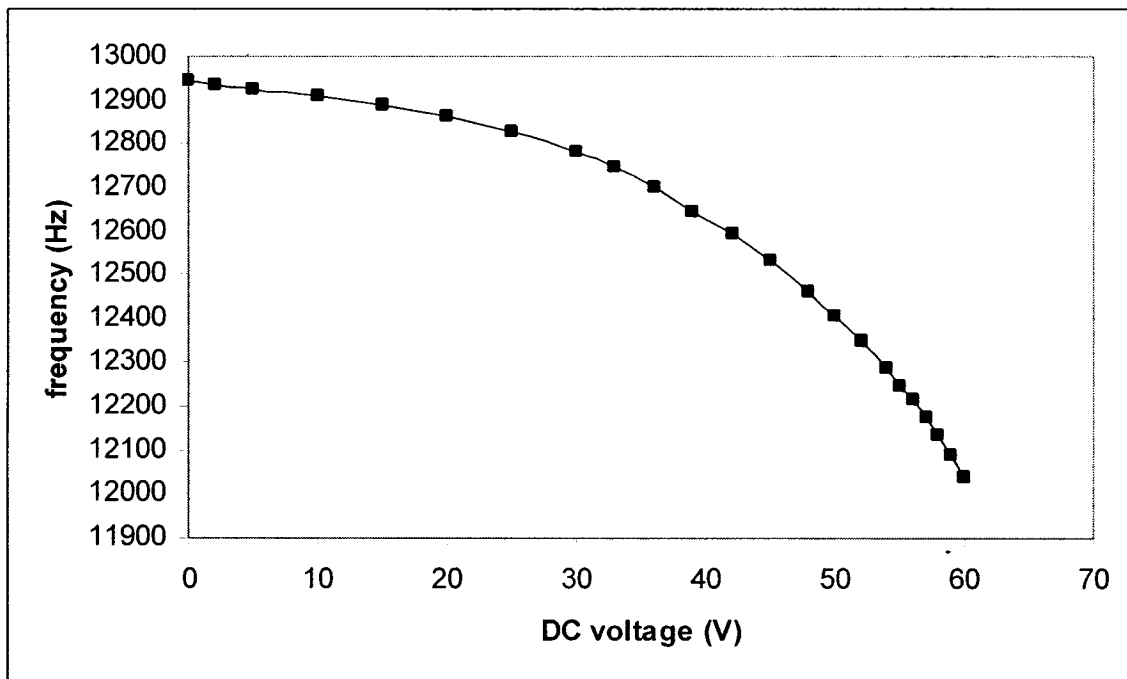
Fig. 5.13 Variation of experimental natural frequency against DC bias voltage at 8V AC

114
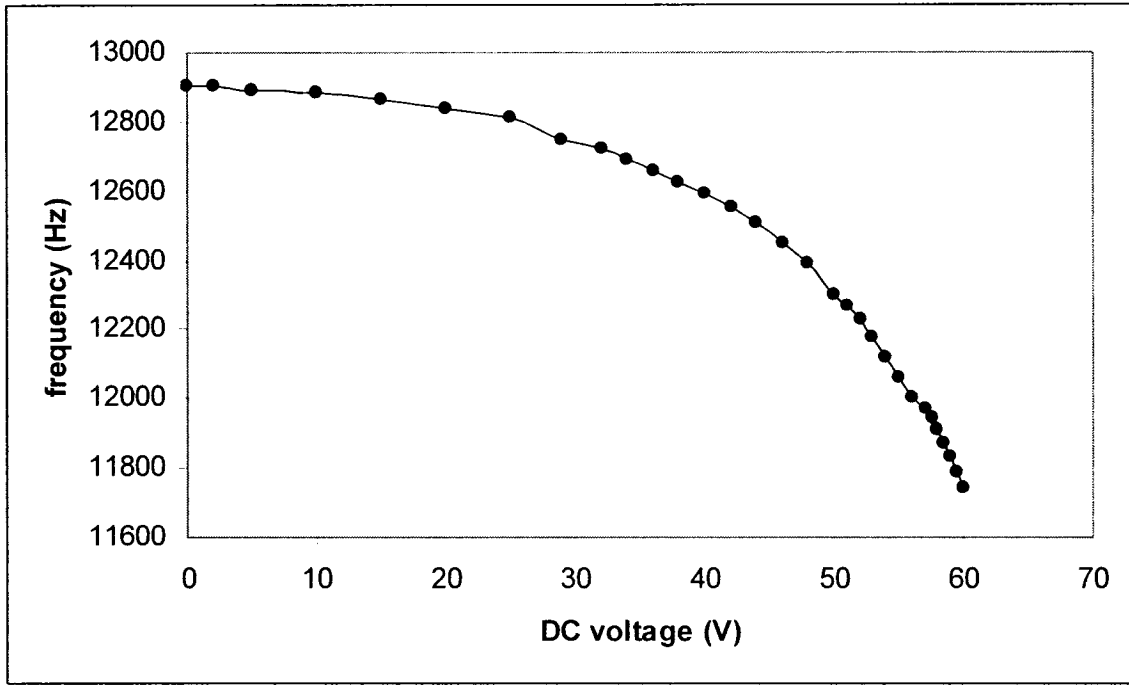
Fig. 5.14 Variation of experimental natural frequency against DC bias voltage at 12V AC
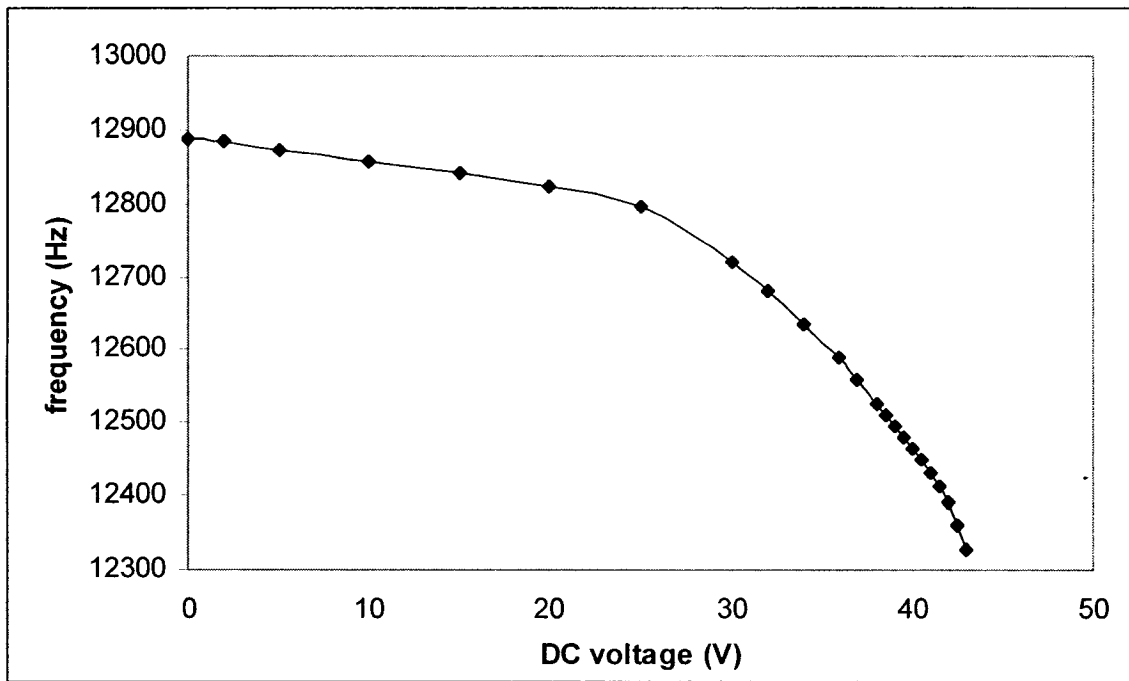
Fig. 5.15 Variation of experimental natural frequency against DC bias voltage at 16V AC
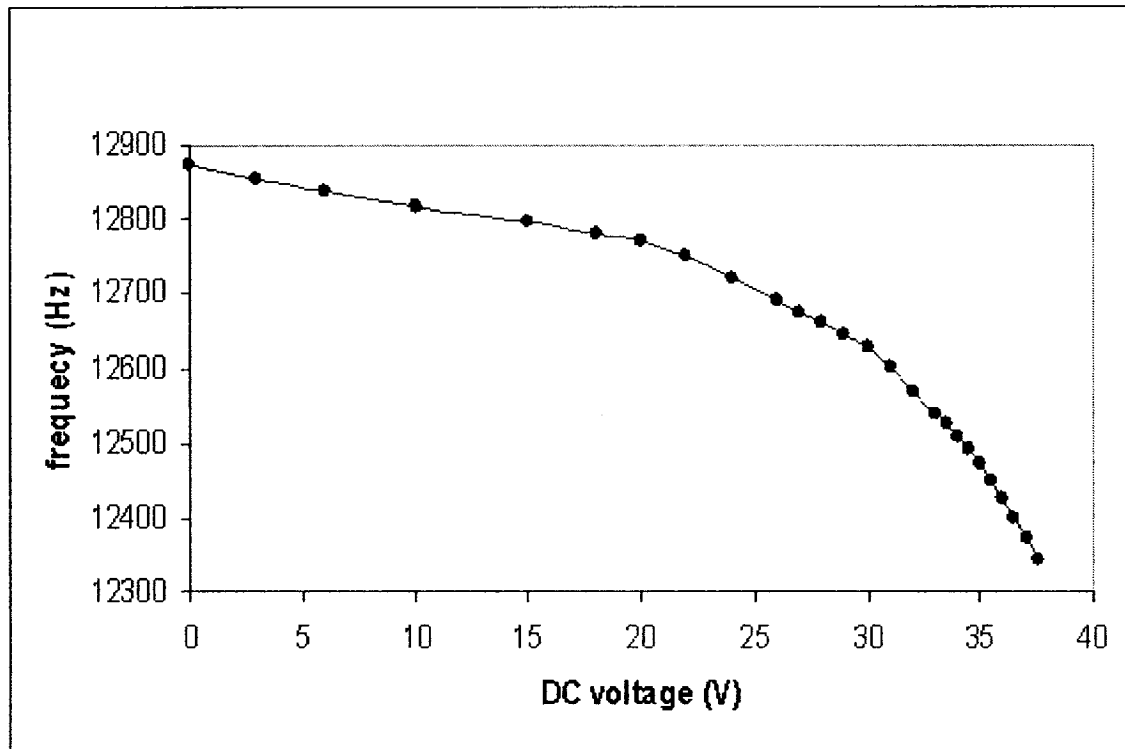
Fig. 5.16 Variation of experimental natural frequency against DC bias voltage at 20V AC

The obtained results are extrapolated till the frequency becomes zero since it is not achieved experimentally due to the pull-in constraint as explained before. This extrapolation is done using the fifth order polynomial and is shown below in Figure 5.17 which has all the curves from Figures 5.11 to 5.16. The fifth order polynomial is chosen for the extrapolation of experimental frequencies since the theoretical frequency prediction at very close to pull-in conditions were also extrapolated with the fifth order polynomial. It can be seen from Figure 5.17 that the frequency becomes zero at different DC voltages for different AC voltages.
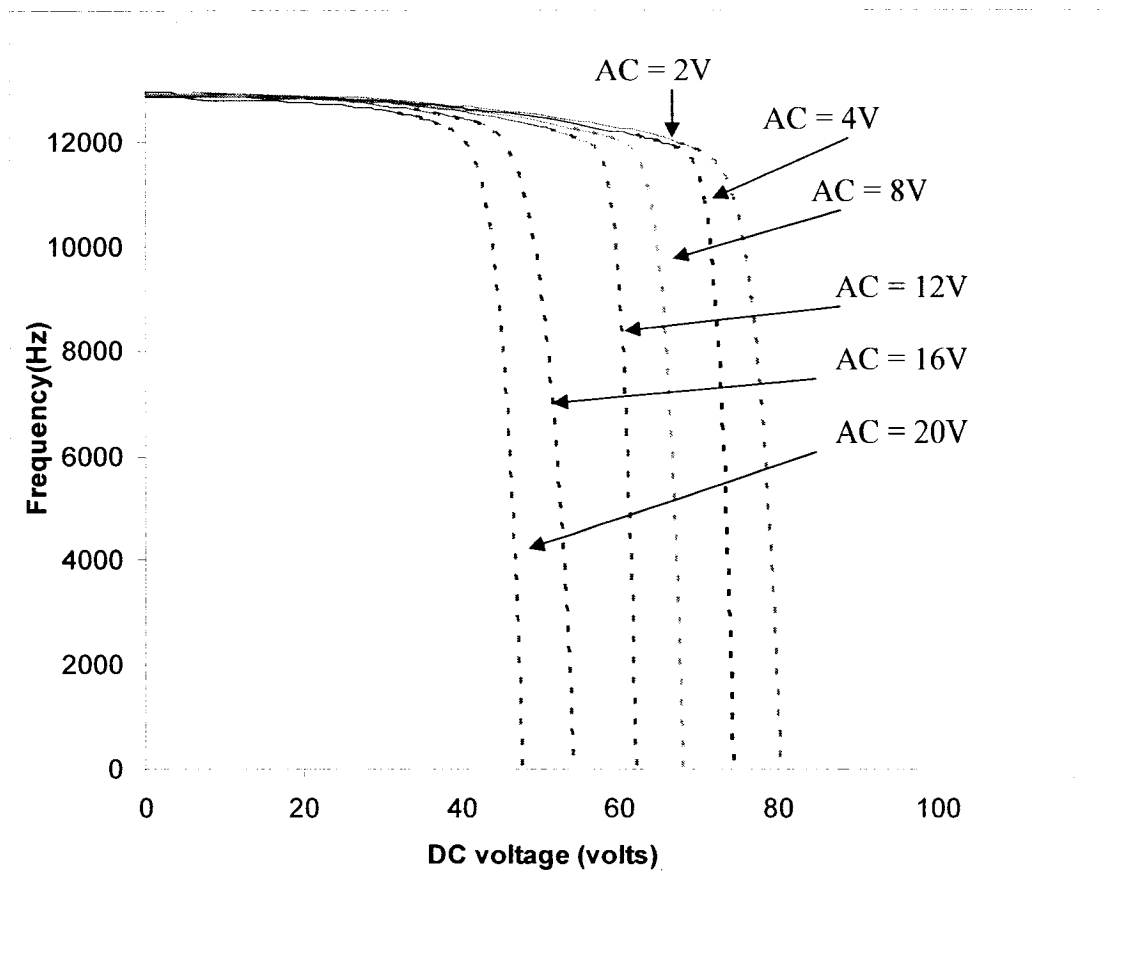
Fig. 5.17 Combined variation of tested natural frequency against DC bias voltage for

2,4,8,12,16 and 20V AC

5.5 Validation

5.5.1 MicraGeM cantilever

In this section, a comparision between the experimental frequency and the nonlinear predicted frequency is done for the MicraGeM cantilever whose dimensions are in Table 4.1. The frequency curve obtained against a varying DC voltage when a 2V AC voltage is

applied during the experimental testing is compared with the frequency curve obtained against a varying voltage with the energy value at E_1^* from the non linear analysis adopted in Chapter 4. The Figure 5.18 shows the comparison between the two curves.
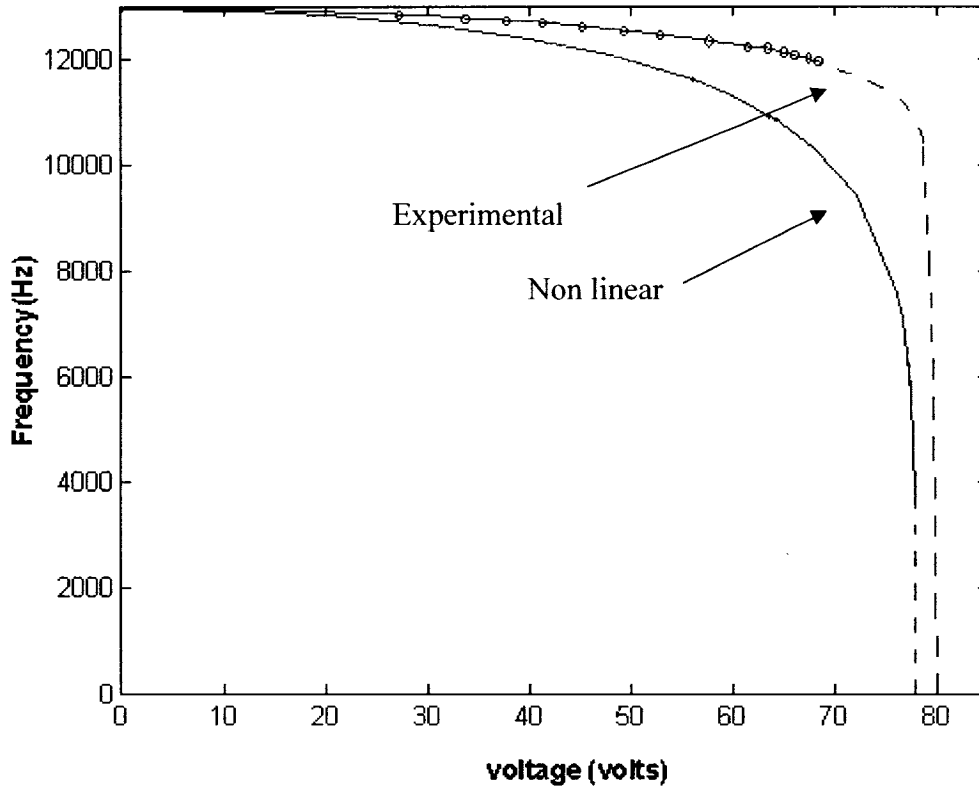
Fig. 5.18 Comparision between the experimental and nonlinear analysis frequency curves

From Figure 5.18, it is seen that the frequency values are almost the same for small value of voltages applied to the cantilever. After a voltage of around 50V, the gap between the frequency curves widens. Also, the voltage at which the frequency becomes zero from the non linear analysis is 77.8V while from the experimental testing, the zero frequency voltage value is extrapolated to be around 80V. Thus a difference of approximately 2.5%

in the accuracy of the pull-in voltage is found between the experimental results and theoretical prediction while doing the dynamic analysis.

5.5.2 AFM cantilever

In this section, the frequency validation of an Atomic Force Microscope (AFM) cantilever experimentally tested by Rinaldi et al. [76] is done. The frequency results obtained based on the nonlinear analysis is compared with both the theoretical (linear analysis) and experimental results of [76]. The dimensions of the cantilever taken by [76] are given below in Table 5.1. The gap between the top and bottom electrodes is 51.2μm.

Table 5.1 Design parameters taken for the comparison of frequency obtained from experimental [76], linear [76] and nonlinear analysis of an AFM cantilever

L (μm)	B (μm)	t (μm)	E (10^9N/m^2)	ρ (kg/m^3)
351	34.5	0.95	169.5	2330

The comparison of the frequency for different cases is done by plotting the natural frequency values against the voltage. It can be seen from Figure 5.19 that the frequency curve obtained from our nonlinear analysis is in very close agreement with the experimental [76] and theoretical [76] curves. The normalized plot of Figure 5.19 is shown below in Figure 5.20 and the close agreement of the values is clearly seen. The frequency values are normalized based on their maximum value as it can be inferred in Figure 5.20 that all the curves start at 1 in the y-axis. For very small voltages, the

nonlinear frequency values seem to be almost the same as that of the theoretical values [76] rather than the experimental [76] values as can be seen from Figure 5.19. For voltages close to the pull-in voltage, the nonlinear curve seems to be in close agreement
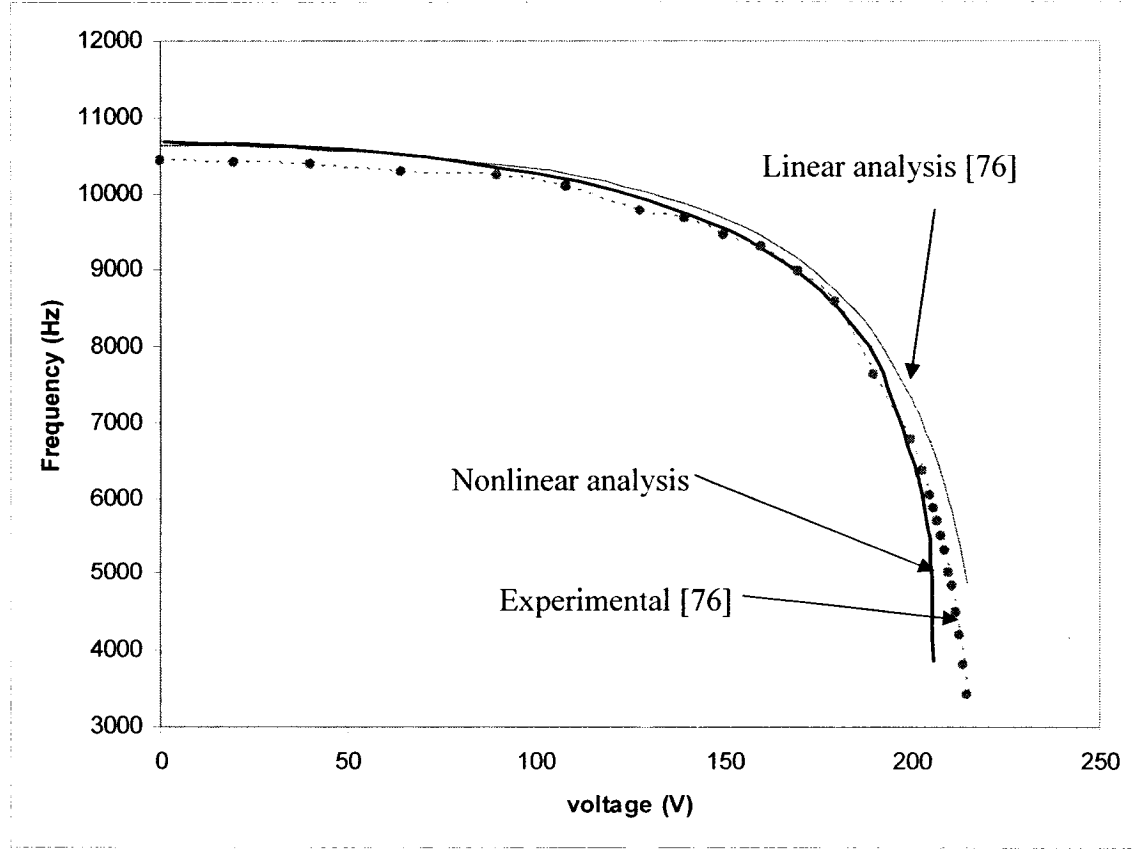
Fig. 5.19 Comparison of frequency obtained from experimental [76], linear [76] and nonlinear analysis of an AFM cantilever

with the experimental curve [76] rather than the theoretical curve [76]. The pull-in voltage value from our nonlinear analysis is less than that of experimental [76] whereas the theoretical [76] seems to be higher. Hence it can be inferred that it is always necessary to apply the nonlinear analysis for larger deflection ranges rather than the linear analysis to avoid pull-in and for the safe operation of the device. The difference

between the experimental and theoretical results can be attributed to the differences in dimensions, material properties and structural deviations between the design intent and that of the real device. In order to compare the variations clearly, the normalized frequencies are given in Figure 5.20 against the bias voltage. One could see a sudden decrease in frequency near pull-in condition with the nonlinear modeling.
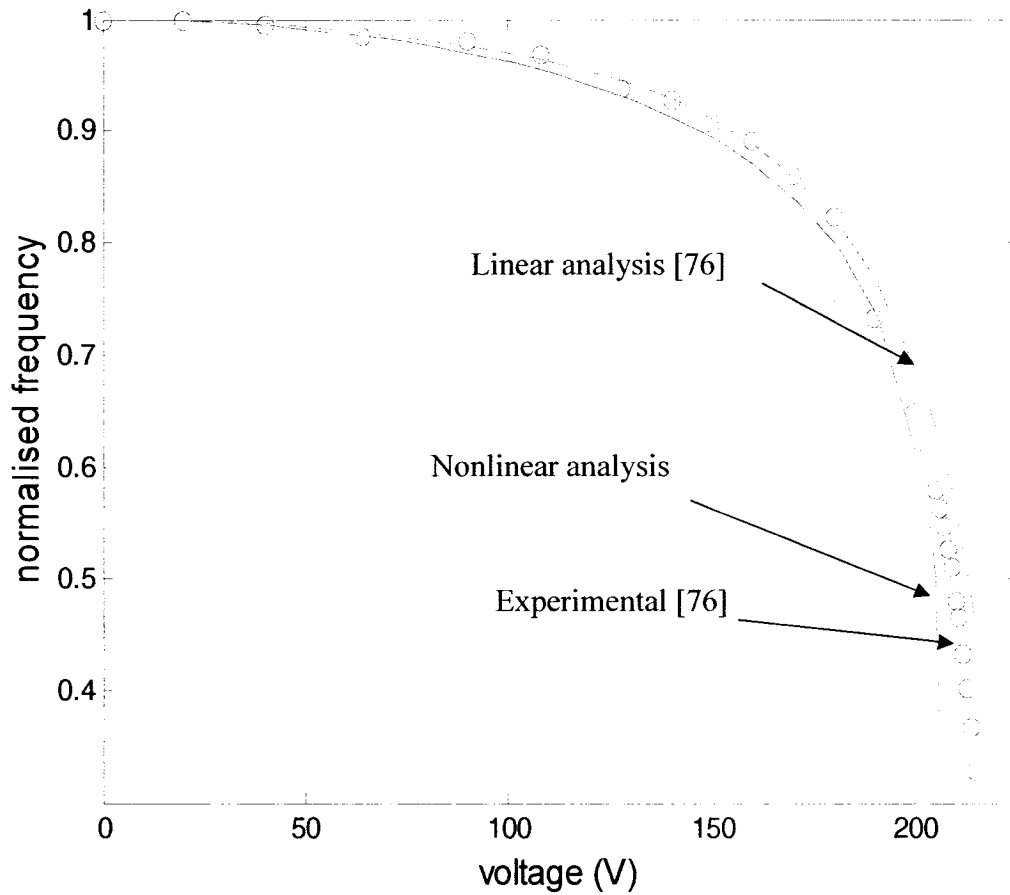
Fig. 5.20 Comparison of the normalized frequency curves

5.6 Summary

The experimental methods that have been adopted so far for MEMS structures have been discussed and a non-contact optical Laser Doppler Velocimetry (LDV) set-up that is used for the testing of micro cantilevers is explained. Then the testing procedure has been discussed and the safety measures taken to avoid the pull-in voltage have been given. The frequency plots have been drawn for different DC and AC voltages using the spectral analyzer frequency responses. The comparison of dynamic frequency plots against the voltage between the experimental test results and the nonlinear theoretical prediction was carried out and the percentage of accuracy of the prediction value has been found. Also, the comparison was carried out for the AFM cantilever [76] and the nonlinear frequency curve seems to be in very close agreement with both the experimental [76] and theoretical [76] curves.

Chapter 6

Conclusions and Future Work

6.1 Conclusions

An introduction to the electrostatic actuation and the pull-in instability in MEMS structures were given and the work done so far in employing both the linear and non linear methods for doing the static and dynamic analysis was discussed. Then the linear analysis of a simple mass-spring model of an electrostatically actuated MEMS structure was done and the significance of the pull-in instability was understood. Similarly, the linear analysis of 1-D aeroelastic wing structure was presented to understand the divergence and flutter instabilities. Thus a comparision between the electrostatic MEMS structures and the aeroelastic wing structures was performed to infer the analogy between the two fields. Also, the control methods employed so far in both the fields to overcome their instabilities were discussed.

The method of microfabricating the MEMS structures based on the MicraGeM technology was explained and the released microstructures such as microplates and micrcantilevers were presented. Then, the conversion of a cantilever system into an equivalent lumped mass-spring model was done and the final equations for calculating the equivalent mass, stiffness and electrostatic area were derived.

An introduction to the non linear analysis using the phase portraits was explained in the case of a simple pendulum. Similarly, a simple mass-spring model of an electrostatically actuated MEMS structure was taken and the non linear analysis based on the phase portraits were done to understand the nonlinearity of the system. Then a cantilever system converted into an equivalent mass-spring model was taken and the similar phase portrait analysis was done to investigate the pull-in instability. The significance of the conservative energy value on the system behaviour was presented and the pull-in voltage values were calculated. Then the dynamic analysis was done based on the time integration and the frequency variation against the conservative energy values was plotted. Similar results were discussed for a cantilever designed using the MicraGeM technology and the frequency curve against the varying voltage was plotted and compared with the result from the linear analysis.

A non-contact optical Laser Doppler Velocimetry (LDV) set-up that was used for the testing of micro cantilevers was explained. Then the testing procedure was discussed and the method of application of both the DC and AC voltages to find the frequency was given. Finally, the frequency plot was compared with the non linear theoretical prediction. The conclusions that can be inferred from the work done in this thesis are presented as follows:

1) A comparision of the electrostatic MEMS structures with the aeroelastic wing structures show that there is a considerable similarity between the instabilities and their control measures in these two domains. .

124

2) Non linear analysis of the electrostatic MEMS structures is done and the pull-in voltages are calculated based on the phase portraits. The results are compared with the published results and they are seen to be in close agreement.

3) From the previous works, it is only the voltage which has a considerable effect on the pull-in phenomenon. In the present work, it is seen that the conservative energy values also seem to influence the system behaviour considerably along with the voltage as different pull-in conditions are achieved based on different energy values.

4) The dynamic analysis is done based on the time integration technique. The frequency values obtained are compared with the linear analysis and it is proved that the linear analysis does not hold good for larger deflections as the pull-in voltages are higher than that of the values from the non linear methods. Hence a safe operation range of the micro devices is found based on the non linear method.

5) The dynamic testing of microcantilever is done successfully using the optical LDV set-up and the frequency values against the varying voltage seem to be in agreement with the non linear theoretical prediction. Thus for applications like optical mirrors, filters and detectors, the non linear method employed in this thesis work can be used for the prediction of the operation range of the MEMS devices.

6) Since various results seem to be in agreement with previously published continuous systems results, it is concluded that the equivalent lumped mass-spring model is adequate for the nonlinear analysis of any continuous systems.

6.2 Future Work

The field of MEMS is multidisciplinary in nature with various possibilities of miniaturization in different areas of engineering. The present work was done mainly for estimating the safe operation of the electrostatic MEMS structures and it was based on the non linear analysis. The following points are formulated that can be considered in the future for research and development purposes:

1) The analogy between electrostatic MEMS structures and the aeroelastic wing structures can be used to improve the static and dynamic performance of both these fields.

2) Non linear analysis based on the phase portraits and the time integration techniques can be done directly on the continuous systems such as cantilever beams instead of converting them into an equivalent mass-spring model.

3) A mathematical relation between the conservative energy value from the non linear analysis and the AC voltage applied from the experimental testing can be derived for the understanding of their similarities in affecting the system behaviour.

References

[1] R. Feynman, "There's Plenty of Room at the Bottom", Caltech's Engineering and Science magazine, 1960.

[2] N. Maluf, "An Introduction to Micro Electro Mechanical Systems engineering", Boston: Artech House, 1999.

[3] G. Kovacs, "Micromachined Transducers Sourcebook", McGraw-Hill, 1998.

[4] H. Fujita, "A Decade of MEMS and its Future", Proc. IEEE Tenth Annual International workshop on MEMS, 1997, pp.1-7.

[5] M. Madou, "Fundamentals of Microfabrication", CRC Press, 1997.

[6] J.W. Gardner, "Microsensors: Principles and Applications", Wiley, 1994.

[7] R.B. Apte, F.S.A. Sandejas, W.C. Banyai, D.M. Bloom, "Deformable Grating Light Valves for High Resolution Displays", Proc. IEEE Solid State Sensor and Actuator Workshop, 1994.

[8] N.P. Pham, K.T. Ng, M. Bartek, P.M. Sarro, B. Rejaei, J.N. Burghartz, "A Micromachining Post-process Module for RF Silicon RF Technology", IEDM Tech. Digest, 11–13, 2000, pp. 481–484.

[9] B. Bahreyni, C. Safai, "Investigation and Simulation of XeF_2 Isotropic Etching of Silicon", Journal of Vacuum Science Technology, Vol. 20, No. 6, 2002, pp. 1850-1854.

[10] K. Petersen, "Silicon as a Mechanical Material", Proc. IEEE, Vol. 70, No. 5, 1982, pp. 420-457.

[11] Y. Ding, Z. Liu, L. Liu, Z. Li, "A Surface Micromachining Process for Suspended RF-MEMS Applications using Porous Silicon", Microsystem Technologies, Vol. 9, No. 6-7, 2003, pp. 470-473.

[12] D.A Koester, R. Mahadevan, B. Hardy, K.W. Markus, "MUMPs Design Handbook", Revision 6.0, Cronos Integrated Microsystems, A JDS Uniphase Company, 2001.

[13] Micralyne Inc., Canadian Microelectronics Corporation, "MicraGeM: A Silicon-on-Insulator Based Micromachining Process", V3.0 (beta version), 2004.

[14] Micralyne Inc., Canadian Microelectronics Corporation," Protolyne™: A Micromachining Process for Microfluidic Applications", V1.0, 2004.

[15] K.A. Shaw, Z.L. Zhang, N.C. MacDonald, "SCREAM I: A Single Mask, Single-Crystal Silicon, Reactive Ion Etching Process for MicroElectroMechanical Structures," Sensors and Actuators A, Vol. 40, 1994, pp. 210-213.

[16] E. Jung, "Packaging Options for MEMS Devices", Materials Research Society Bulletin, Vol. 28, No. 1, 2003, pp. 51-54.

[17] Y.L. Low, R.E. Scotti, D.A. Ramsey, C.A. Bolle, "Packaging of Optical MEMS Devices", Proceedings of SPIE - The International Society for Optical Engineering, Vol. 4408, 2001, pp. 409-414.

[18] S.D. Senturia, "Microsystem Design", Kluwer Academic Publishers, 2001.

[19] C. Liu, Y.B. Cohen, "Scaling Laws of Microactuators and Potential Applications of Electroactive Polymers in MEMS", Proceedings of SPIE's 6th Annual International Symposium on Smart Structures and Materials, Vol. 33, No. 3669, 1999.

[20] U.F. González, W.A. Moussa, "Simulation of MEMS Piezoelectric Micropump for Biomedical Applications", University of Alberta with ALGOR Inc., 2002.

[21] J.Y. Park, Y.J. Yee, H.J. Nam, J.U. Bu, "Micromachined RF MEMS Tunable Capacitors using Piezoelectric Actuators", IEEE MTT-S International Microwave Symposium Digest, Vol. 1, 2001, pp. 2111-2114.

[22] H.Q. Li, D.C. Roberts, J.L. Steyn, K.T. Turner, O. Yaglioglu, N.W. Hagood, S.M. Spearing, M.A. Schmidt, "Fabrication of a Microvalve with Piezoelectric Actuation", Proceedings of the IEEE Micro Electro Mechanical Systems, 2003, pp. 92-95

[23] Y.W. Yong, C. Liu, "Magnetic Actuation of hinged Microstructures", Journal of Microelectromechanical Systems, Vol.8, No. 1, 1999, pp. 10-17.

[24] D. Yan, A. Khajepour, R. Mansour, "Design and Modeling of a MEMS Bidirectional Vertical Thermal Actuator", Journal of Micromechanics and Microengineering, Vol. 14, No. 7, 2004, pp. 841-850.

[25] S. Mutzenich, T. Vinay, G. Rosengarten, "Analysis of a Novel Micro-hydraulic Actuation for MEMS", Sensors and Actuators A, Vol.116, 2004, pp.525-529.

[26] B. Borovic, F.L. Lewis, M.M. Hossain, D. Agonafer, E.S. Kolafer, "Experimentally verified Procedure for Determining Dynamical Model of the ETM MEMS Structures", Proc. IEEE Inter Society Conference on Thermal Phenomena, 2004, pp.541-548.

[27] D.J. Bell, T.J. Lu, N.A. Fleck, S.M. Spearing, "MEMS Actuators and Sensors: Observations on their Performance and Selection for Purpose", Journal of Micromechanics and Microengineering, Vol. 15, 2005, pp. 153–164.

[28] V.T. Srikar, S.M. Spearing, "Material Selection for microfabricated Electrostatic Actuators", Sensors and actuators A, No.102, 2003, pp.279-285.

[29] P.M. Osterberg, S.D. Senturia, "M-TEST: A Test Chip for MEMS Material Property Measurement using Electrostatically actuated Test Structures", Journal of Microelectromechanical systems, Vol.6, No.2, 1997, pp.107-118.

[30] Y. Zhu, H.D. Espinosa, "Reliability of Capacitive RF MEMS Switches at High and Low Temperatures", International Journal of RF Microwave Computer Aided Engineering, No.14, 2003, pp.317–328

[31] H.C. Nathanson, W.E. Newell, R.A. Wickstrom, J.R. Davis, "The Resonant Gate Transistor", IEEE Transaction on Electron Devices, Vol. 14, 1967, pp. 117-133.

[32] P.D. Dobbelaere, K. Falta, L. Fan, S. Gloeckner, S. Patra, "Digital MEMS for Optical Switching", IEEE Communications Magazine, No.2, 2002 pp.88-95.

[33] J. Jin, T.C. Yih, T. Higuchi, J.U. Jeon, "Direct Electrostatic Levitation and Propulsion of Silicon Wafer", IEEE Transactions on Industry Applications, Vol.34, No.5, 1998, pp.975-984.

[34] J. Bay, O. Hansen, S. Bouwstra, "Micromachined Double Backplate Differential Capacitive Microphone", Journal of Micromechanics and Microengineering, No.9, 1999, pp.30–33.

[35] D. Bernstein, P. Guidotti, J.A. Pelesko, "Mathematical Analysis of an Electrostatically actuated MEMS Device", Proc. Modeling and Simulation of Microsystems, 2000, pp.489–492.

[36] J.A. Pelesko, "Multiple Solutions in Electrostatic MEMS", Proc. Modelling and simulation of Microsystems, 2001, pp.290-293.

[37] S. Pamidighantam, R. Puers, K. Baert, H.A.C. Tilmans, "Pull-in Voltage Analysis of Electrostatically actuated Beam Structures with Fixed–Fixed and Fixed–Free End

Conditions", Journal of Micromechanics and Microengineering, Vol.12, 2003, pp. 458–464.

[38] X. Zhao, A. Nayfeh, "A reduced Order Model for Electrically actuated Microplates", Structures, Structural Dynamics and Materials Conference, 2004, pp.19 – 22.

[39] G. Rinaldi, M. Packirisamy, I. Stiharu, "Boundary Characterization of Microstructures through Thermo-Mechanical Testing", Journal of Micromechanics and Microengineering, Vol.16, 2006, pp.549-556.

[40] J. Cheng, J. Zhe, X. Wu, "Analytical and Finite Element Model Pull-in Study of Rigid and Deformable Electrostatic Microactuators", Journal of Micromechanics and Microengineering, Vol.14, 2004, pp.56-68.

[41] S. Chowdhury, M. Ahmadi, W.C. Miller, "A Closed-form Model for the Pull-in Voltage of Electrostatically actuated Cantilever Beams", Journal of Micromechanics and Microengineering, Vol.15, 2005, pp.756-763.

[42] Coventor Inc., "Pull-in Voltage Analysis of Electrostatically actuated Beams verifying Accuracy of Coventor Behavioral Models", Available online at http://www.coventor.com/media/fem comparisons/pullin voltage.pdf

[43] J.H. Kuang, C.J. Chen, "Dynamic Characteristics of shaped Micro-actuators solved using the Differential Quadrature Method", Journal of Micromechanics and Microengineering, Vol.14, 2004, pp.647-654.

[44] A. Collenz, F.D. Bona, A. Gugliotta, A. Soma, "Large Deflections of Microbeams under Electrostatic Loads", Journal of Micromechanics and Microengineering, Vol.14, 2004, pp.365-373.

[45] W.C. Xie, H.P. Lee, S.P. Lim, "Nonlinear Dynamic Analysis of MEMS Switches by Nonlinear Modal Analysis", Nonlinear Dynamics, Vol.31, 2003, pp.243-256.

[46] W. Zhang, R. Baskaran., K.L.Turner, "Nonlinear Dynamics Analysis of a Parametrically Resonant MEMS Sensor", Proc. Society for Experimental Mechanics, MEMS Symposium, 2002.

[47] S. Liu, A. Davidson, Q. Lin, "Simulation Studies on Nonlinear Dynamics and Chaos in a MEMS Cantilever Control System", Journal of Micromechanics and Microengineering, Vol.14, 2004, pp.1064-1073.

[48] M. Serry, D. Walliser, G.J. Maclay, "The Anharmonic Casimir Oscillator (AC0)-The Casimir Effect in a Model Micro Electro Mechanical System", Journal of Microelectromechanical systems, Vol.4, No.4, 1995, pp.193-205.

[49] A. Fargas-Marques, A.M. Shkel, "On Electrostatic Actuation beyond Snapping Condition", IEEE Sensors, 2005, pp. 600-603

[50] F. Shi, P. Ramesh, S. Mukherjee, "Dynamic Analysis of Micro Electro Mechanical Systems", International Journal for Numerical methods in engineering, Vol.39, 1996, pp.4119-4139.

[51] A.H. Nayfeh, M.I. Younis, "Dynamics of MEMS Resonators under Superharmonic and Subharmonic Excitations", Journal of Micromechanics and Microengineering, Vol.15, 2005, pp.1840-1847.

[52] S. Krylov, R. Maimon, "Pull-in Dynamics of an Elastic Beam actuated by Continuously Distributed Electrostatic Force", Journal of Vibration and Acoustics, Vol.126, 2004, pp.332-342.

[53] A.C.J. Luo, F.Y. Wang, "Nonlinear Dynamics of a Micro Electro Mechanical System with Time-varying Capacitors", Journal of Vibration and Acoustics, Vol.126, 2004, pp.77-83.

[54] J.B. Arfken, "Mathematical Methods for Physicists". Academic Press, 1985, pp. 303-313.

[55] R.B. Bhat, "Principles of Aeroelasticity", Course notes for Principles of Aeroelasticity (Mech 6481), Concordia University, Montreal, Canada.

[56] E.G. Kenneth, "Active Control of Aircraft Wings with Divergence and Flutter Instabilities", Journal of aircraft, 1982.

[57] J. Heeg, "An Analytical and Experimental Investigation of Flutter Suppression via Piezoelectric Actuation", Proc. AIAA 33rd Dynamic Specialists Meeting, 1992.

[58] M.H. Shirk, T.J. Hertz, T.A. Weisshaar, "Aeroelastic Theory, Practices and Promises", Journal of Aircraft, Vol. 23, No.1, 1986, pp.6-18.

[59] T.A. Weisshaar, "Aeroelastic Tailoring of Forward Swept Composite Wings", Journal of Aircraft, Vol.18, No.8, 1981, pp-669-676.

[60] F.H. Gern, L. Librescu, "Aeroelastic Tailoring of Composite Wings Exhibiting Nonclassical Effects and Carrying External Stores", Journal of Aircraft, Vol.37, No.6, 2000, pp.1097-1104.

[61] J.I. Seeger, S.B. Crary, "Stabilization of Electrostatically Actuated MEMS Devices", International Conference on Solid-state Sensors and Actuators, 1997.

[62] P.B. Chu, S.J. Pister, "Analysis of Closed-loop Control of Parallel-Plate Electrostatic Microgrippers," IEEE Int. Conf Robotics and Automation, 1994, pp.820-825.

[63] S. Pamidighantam, R. Puers, K. Baert, H.A.C. Tilmans, "Pull-in Voltage Analysis of Electrostatically Actuated Beam Structures with Fixed–Fixed and Fixed–Free End Conditions", Journal of Micromechanics and Microengineering, Vol.12, 2003, pp. 458–464.

[64] M.A. Rosa, D.D. Bruyker, A.R. V"olkel, E. Peeters, J. Dunec, "A Novel External Electrode Configuration for the Electrostatic Actuation of MEMS Based Devices", Journal of Micromechanics and Microengineering, Vol. 14, 2004, pp. 446–451.

[65] O.B. Degani, Y. Nemirovsky, "On the Effect of Residual Charges on the Pull-In Parameters of the MEMS Actuators", Sensors and Actuators, 2002.

[66] Canadian Microelectronic Corporation, Micralyne Inc., "Introduction to MicraGeM: A Silicon-on-Insulator based Micromachining Process", V3.0 Beta Version, 2004.

[67] Canadian Microelectronic Corporation, Carruthers Hall, Kingston, Ontario, Canada, K7L 3N6.

[68] A.K. Bhaskar, "Synthesis of Electrostatically actuated Optical Micromirrors", M.A.Sc Thesis, Department of Mechanical and Industrial Engineering, Concordia University, Montreal, 2004.

[69] Micralyne Inc, 1911-94 Street, Edmonton, Alberta, Canada, T6N 1E6.

[70] Y.C. Hu, C.M. Chang, S.C. Huang, "Some Design Considerations on the Electrostatically actuated Microstructures", Sensors and Actuators A, No.112, 2003, pp. 155-161.

[71] A.H. Nayfeh , D.T. Mook, "Nonlinear Oscillations", John Wiley and Sons, 1979.

[72] L.P. Fulcher, B.F. Davis, "Theoretical and Experimental Study of the Motion of the Simple Pendulum", American Journal of Physics, Vol.44, No.1, 1976, pp.51-55.

[73] N. Kryloff, N. Bogoliuboff, "Introduction to Nonlinear Mechanics" Princeton University, Princeton, New Jersey, 1947.

[74] R. Simon, R.P. Reisz, "Large Amplitude Simple Pendulum", American Journal of Physics, Vol.47, No.10, 1979, pp.898-899.

[75] S.C. Shadden, "A Dynamical Systems Approach to Unsteady Systems", PhD Thesis, California Institute of Technology, California, 2006.

[76] G. Rinaldi, "Dynamic Analysis and Validation of Cantilever MEMS subjected to Electro-Thermo-Mechanical Influences", Ph.D. Dissertation, Department of Mechanical and Industrial Engineering, Concordia University, Montreal, QC, 2006.

[77] T. Yi, C.J. Kim, "Measurement of Mechanical Properties of MEMS Materials", Measurement Science and Technology, Vol. 10, 1999, pp. 706-716.

[78] V.T. Srikar, S.M. Spearing, "A Critical Review of Microscale Mechanical Testing Methods used in the Design of Microelectromechanical Systems", Experimental Mechanics, Vol.43, 2003, pp. 238-247.

[79] Srikar, Spearing, "Mechanical Test Methods for MEMS devices", Experimental Mechanics, Vol. 43, 2003, pp. 228-237.

[80] T. Tsuchiya, O. Tabata, J. Sakata, Y. Taga, "Specimen Size Effect on Tensile Strength of Surface-micromachined Polycrystalline Silicon Thin Films", Journal of Micromechanical Systems, Vol. 7, 1998, pp. 106-113.

[81] F. Ericson, J.A. Schweitz, "Micromechanical Fracture Strength of Silicon", Journal of Applied Physics, Vol. 68, 1990, pp. 5840-5844.

[82] S.M. Hu, "Critical Stress in Silicon Brittle Fracture, Effect of Ion Implantations and Other Surface Treatments", Journal of Applied Physics, Vol. 53, 1982, pp. 3576-3580.

[83] M. Finot, I.A. Blech, S. Suresh, H. Fujimoto, "Large Deformation and Geometric Instability of Substrates with Thin-Film Deposits", Journal of Applied Physics, Vol. 81, 1997, pp. 3457-3464.

[84] T. Ikehara, R.A.F. Zwijze, K. Ikeda, "New Method for an Accurate Determination of Residual Strain in Polycrystalline Silicon Films by Analysing Resonant Frequencies of Micromachined Beams", Journal of Micromechanics and Microengineering, Vol. 11, 2001, pp. 55-60.

[85] W.C. Oliver, G.M. Pharr, "An Improved Technique for Determining Hardness and Elastic Modulus using Load and Displacement Sensing Indentation Experiments", Journal of Materials Research, Vol. 7, 1992, pp. 1564-1583.

[86] J.A. Knapp, D.A. Follsdaedt, S.M. Myers, J.C. Barbour, T.A. Friedmann, "Finite Element Modelling of Nanoindentation", Journal of Aplied Physics, Vol. 85, 1999, pp. 1460-1474.

[87] R. Saha, W.D. Nix, "Effects of the Substrate on the Determination of Thin Film Mechanical Properties by Nanoindentation", Acta Materiala, Vol. 50, 2002, pp. 23-38.

[88] G.C. Brown, "Laser Interferometric Methodolgies for Characterizing Static and Dynamic Behavior of MEMS", Ph.D. Dissertation, Center for Holographic Studies and Laser Micro-Mechatronics, Mechanical Engineering Department, WPI, Worcester, MA,1999.

[89] Bruel & Kjaer, Naerum, Denmark, "The Industry's Broadest Range of Modal Analysis Equipment and Solutions", published magazine, No.1, 2002.